Highly Multiplexed Fluorescence Microscopy with Spectrally Tunable Semiconducting Polymer Dots

Ziyu Guo

A dissertation
submitted in partial fulfillment of the
requirements for the degree of

Doctor of Philosophy

University of Washington
2025

Reading Committee:
Joshua C. Vaughan
Daniel T. Chiu
Robert E. Synovec

Program Authorized to Offer Degree:

Chemistry

University of Washington

Abstract

Highly Multiplexed Fluorescence Microscopy
with Spectrally Tunable Semiconducting Polymer Dots

Ziyu Guo

Chair of the Supervisory Committee:
Joshua C. Vaughan
Departments of Chemistry and Physiology & Biophysics

The need for advanced imaging tools has grown rapidly with the increasing complexity of biological questions. To understand how cells behave and interact in near physiological conditions, in either thin tissue slices or across whole tissues, researchers must be able to map a wide range of molecular targets across space and scale. Traditional fluorescence imaging is limited to around five targets for a single sample. Commonly used probes often suffer from spectral overlap, narrow Stokes shifts, and susceptibility to photobleaching. This bottleneck restricts multiplexing and narrows the biological insight that can be gained from a single experiment. Beyond that, deep tissue imaging poses additional challenges. Light scattering and absorption, especially in thick or uncleared samples, can significantly degrade resolution and signal quality. Together, these limitations reduce both the depth and dimensionality of the information that can be extracted from complex specimens. As a result, questions involving spatial organization, tissue-scale signaling, or multicellular interactions often remain only partially answered. In this dissertation, I explore new strategies to push the boundaries of multiplexed fluorescence imaging, both in thin sections and in intact, cleared tissues. Chapter 1 introduces the core principles of fluorescence microscopy and highlights the constraints posed by conventional labeling tools in high-plex settings. Chapter 2 presents a new

approach based on spectrally tunable semiconducting polymer dots (Pdots), which achieve large Stokes shifts and high brightness, enabling simultaneous detection of over 20 targets without specialized hardware or iterative cycles. Building on this foundation, Chapter 3 extends this capability into three dimensions through the integration of polymer-dot labeling with light sheet fluorescence microscopy and tissue clearing techniques. With further optimization on this system, I aim to build a fast, highly-multiplexed and scalable volumetric imaging platform, suitable for generating rich molecular and structural maps of biological systems of thick or whole organs.

Table of Contents

List of Figures and Tables

Acknowledgments

Thanks to all the mice — I hope they're having fun in heaven.

I'm deeply grateful to my boss, Professor Joshua Vaughan, for all his guidance and encouragement throughout my PhD. He's kind, patient, and always full of good humor, which made this long journey much more enjoyable. He took us boating and even taught us how to read the navigation charts onboard. One of the most unforgettable moments from these five years was in 2024, when Josh hosted a party at his house. That night, he played the guitar and sang a song that he had written and composed himself, and the lyrics were about each one of us in the lab. All in all, he's just an incredibly cool boss. Many thanks to Dr. Chetan Poudel, our amazing (and only!) postdoc, for the great time we had working together on the Pdot project. I learned so much from him, and I feel lucky to have him as my co-first author on our Science Advances paper. Maddie and Adil — who joined the group with me the same year during the pandemic — have been there since the beginning. Most of our early memories are from Zoom meetings instead of in-person chats, but those tough times brought us closer (I'll treasure all those pixelated, funny Zoom screenshots). They've supported me in both research and personal life, and I'm thankful for the laughs and encouragement they brought along the way. Thanks to Chris, "the second PI in the lab." I really enjoyed working with him on the KECK project and learned a lot from his perspective. Thank you, Hannah, for always being open to chatting and for helping me perfect my slides with your keen eye for detail. Thanks to Yuka, Wenhui, Pedro, Erica, and Trevor for always keeping our lab full of laughter and making it a fun workplace. Special thanks to Professor Daniel Chiu and his team for generously providing us with those amazing Pdots — they were absolutely essential to the success of my experiments. Another special thank you to my undergrads, Yvonne and Siying, for their hard work and dedication to my project. I truly appreciate their effort and wish them all the best in reaching their goals for graduate school. Last, thanks to my best emotional support kitties, Xiaoli (Kris) and Boluo. Miaomiaomiao miaomiao miaomiao, miaomiao miao miaomiaomiaomiao.

Thank you all for being part of this journey and for making my time in graduate school memorable and fulfilling.

Chapter 1

Introduction

1.1. Fluorescence Microscopy

1.1.1. Overview of Microscopy and Its Importance to Biology and Medicine

Microscopy has improved our understanding of biology by allowing us to directly observe microscopic structures that are otherwise invisible to the naked eye. Optical microscopy, in particular, is essential for studying complex biological processes in live cells, tissues, and organisms[1,2]. The capability to study biological specimens non-destructively under their near-physiological conditions allows researchers to gain an exceptional understanding of dynamic cellular processes and disease pathogenesis, as well as structure-function relationships. From fundamental cellular biology to clinical diagnostics, optical microscopy is a cornerstone of life sciences and medicine. This technology improved our understanding of disease processes and facilitated the discovery of potential therapeutic targets.

Various microscopy modalities, such as brightfield[3], phase contrast[4], and confocal microscopy[5–7], each serve important roles in a wide range of applications. Brightfield microscopy, which uses transmitted white light to visualize specimens, is one of the simplest and most widely applied techniques. Phase contrast microscopy enhances contrast through phase shift differences in light to reveal internal structures of transparent samples like live cells without staining. Confocal microscopy offers higher resolution and optical sectioning capabilities by using point illumination and pinhole apertures to block out-of-focus light from above and below the focal plane, making it suitable for imaging thick specimens and obtaining three-dimensional structural information. Among the newer advancements, light sheet fluorescence microscopy[8–12] (LSFM) (see **Chapter 1.3.1**) has brought a breakthrough in imaging technology as it only illuminates the focal plane with a thin sheet of light, which minimizes out-of-focus excitation and photodamage. This optical sectioning approach enables rapid imaging of large specimens, such as whole organs or embryos, with improved signal-to-background contrast compared to widefield or spinning disk microscopy[7], while also supporting high-speed volumetric acquisition. These diverse modalities collectively provide unparalleled insights into biological systems, which contribute significantly to both basic research and medical advancements.

1.1.2. Overview of Fluorescence Microscopy

Expanding on the previously discussed microscopy modalities, fluorescence microscopy[13–15] enables the visualization of multiple structures at the cellular and molecular levels with high sensitivity and high selectivity if coupled with immunostaining (see **Chapter 1.1.3**). This imaging technique leverages the unique properties of fluorescent molecules[16], which absorb light at specific wavelengths and emit light at longer wavelengths. By utilizing specialized optical components to selectively excite these fluorophores and detect their emitted fluorescence, researchers can achieve highly specific and sensitive imaging. The resulting high contrast against a dark background is particularly advantageous for studying intricate biological samples. The ability to simultaneously study numerous desired molecules or structures within the same sample allows for the detailed analysis of cellular processes and their spatial interactions in complex biological systems[15,17]. This versatility has established fluorescence microscopy as an essential tool for unraveling the complexities of cellular organization and even understanding structures and functions at the organ level.

Advanced modalities, such as confocal microscopy[5–7], two-photon excitation microscopy[18,19], and the recently developed light-sheet microscopy[8–12], have significantly enhanced the capabilities of fluorescence imaging. These technologies enable deeper penetration of light in thick tissue samples, and the ability to monitor dynamic processes in live cells and tissues with exceptional precision. Importantly, these advancements have extended the application of fluorescence microscopy beyond cellular studies to organ-level research, allowing detailed visualization of complex structures and functional processes within intact tissues and organs.

As a result, fluorescence microscopy has become an indispensable tool in biological and medical research. From investigating cellular signaling pathways and tissue architecture to unraveling disease mechanisms at both the cellular and organ scales, it continues to drive groundbreaking discoveries at the forefront of science.

1.1.3. Overview of Fluorescent Probes

Fluorescent probes are essential components in fluorescence microscopy, offering specificity and sensitivity for visualizing and tracking molecules, cells, organ structures, and biological processes[20–22]. These probes can target various biomolecules, including nucleic acids, proteins, and lipids, through conjugation with antibodies, ligands, or oligonucleotides. Their applications span cell and molecular imaging, flow cytometry, super-resolution microscopy, and even diagnostic and therapeutic fields. The design of fluorescent probes is critical, with factors such as stability, brightness, and photostability, which

will determine the success of an experimental analysis and the quality of the resulting data. An effective probe must include (1) a targeting moiety to bind the molecule of interest specifically and (2) a fluorophore to provide high-contrast visualization[15]. A variety of fluorescent probes have been developed to study live and fixed specimens, such as Fluorophore-antibody conjugates, small-molecule probes, and fluorescent proteins, which are discussed in the following subsections.

1.1.3.1. Fluorophore-antibody Conjugates

One widely used category of fluorescent probes is fluorophore-antibody conjugates and its labeling technique is called immunofluorescence (IF). The technique uses highly specific antibodies to visualize and quantify proteins within cells or tissues.

Antibodies, classified into several major classes (e.g., IgG, IgE, IgD, IgA, and IgM for humans, though these can vary across species), bind specifically to antigenic epitopes through their paratope on the variable regions. They can be monoclonal, offering high specificity to a single epitope, or polyclonal, recognizing multiple epitopes but with higher variability (**Table 1.1**). They can also be genetically engineered, such as recombinant antibodies produced in vitro, that are highly reproducible with low lot-to-lot variability[23].

Table 1.1. Comparison of monoclonal and polyclonal antibodies.

	Monoclonal Antibodies (mAbs)	**Polyclonal Antibodies (pAbs)**
Production Method	Produced via hybridoma technology (B cell fused with myeloma cell)	Produced by immunizing animals (e.g., rabbit, goat) and collecting serum
Epitope Recognition	Recognizes a single, specific epitope on the antigen	Recognizes multiple epitopes on the same antigen
Specificity	Very high specificity; minimal cross-reactivity	Broader reactivity; more likely to bind similar antigens
Sensitivity	May have lower signal (single epitope)	Often higher signal due to multiple binding events
Reproducibility	High batch-to-batch consistency	Lower consistency between batches or animals
Tolerant to Epitope Change	Less tolerant to protein denaturation or fixation	More tolerant to changes; better for fixed or denatured samples
Cross-Reactivity	Low, ideal for clean backgrounds in imaging	Higher, may result in non-specific binding
Cost	More expensive due to production complexity	Less expensive

Fluorophore-antibody conjugates are typically formed via covalent coupling or bioconjugation, such as reactions between primary amines on antibodies and n-hydroxysuccinimide (NHS) ester-functionalized

fluorophores, resulting in stable bonds under mild conditions[24]. Recent advances in antibody engineering and modifications, like recombinant antibodies, have further improved the performance of these conjugates, enhancing their utility in microscopy applications.

There are two major methods for labeling specimens in immunofluorescence: direct and indirect approaches (**Figure 1.1** and **Table 1.2**). In direct immunofluorescence, fluorophores are conjugated directly to primary antibodies. This provides a straightforward labeling process that avoids issues such as species cross-reactivity when targeting multiple antigens in a single round. However, this method has a higher potential to alter the primary antibody structure, which will decrease the specificity or, in the worst case, lose the binding function to epitopes[25]. Also, direct immunofluorescence is often more costly than the indirect approach because primary antibodies are more expensive than secondary antibodies and also have dimmer signals from lower fluorophore per antigen, as shown in **Figure 1.1**. Indirect immunofluorescence involves using an unconjugated primary antibody to bind the target antigen, followed by a fluorophore-conjugated secondary antibody, which allows for greater flexibility in fluorophore selection and which also achieves signal amplification. To achieve the same signal-to-noise ratio, a higher amount of primary antibody is generally used in direct immunofluorescence. Despite its versatility, immunofluorescence has inherent challenges. Labeling thick specimens can be time-consuming due to the large size of antibodies and their slow diffusion in tissue, and the effectiveness of labeling often depends on how easily the target antigens can be reached within the dense tissue environment[26]. Additionally, variability in antibody performance can affect reproducibility, presenting further obstacles in complex applications[27].

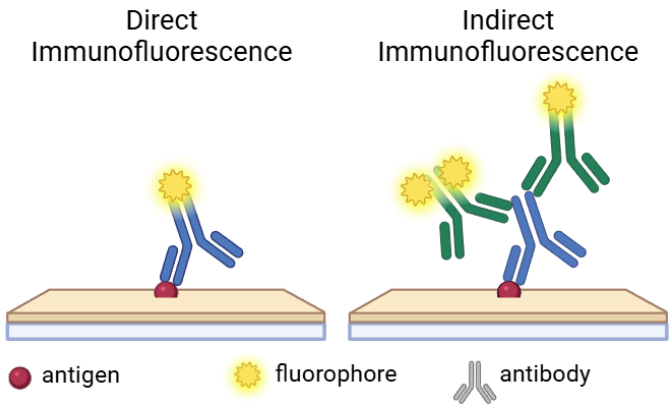

Figure 1.1. *Direct and indirect immunofluorescence.*

Table 1.2. Comparison of Direct and Indirect Immunostaining

	Direct Immunostaining	Indirect Immunostaining
Antibody conjugation	Primary antibody is directly conjugated to a fluorophore or label	Unlabeled primary antibody is detected by a labeled secondary antibody
Steps	Single staining step	Two-step process: primary antibody followed by labeled secondary antibody
Signal Amplification	Limited (few fluorophores per antibody)	Higher (multiple secondary antibodies can bind each primary antibody)
Sensitivity	Lower sensitivity	Higher sensitivity
Specificity	High specificity but limited amplification	Specificity depends on primary-secondary antibody interaction
Experiment time	Faster (one incubation)	Slower (requires multiple incubations)
Flexibility	Less flexible—requires new conjugates for each primary antibody	More flexible—same secondary can be used with many primaries
Multiplexing Potential	Limited—requires spectrally distinct primary conjugates	Higher—flexibility in using different secondary antibodies
Cross-Reactivity	Lower (fewer antibodies involved)	Higher (non-specific binding by secondary antibodies possible)
Cost	More expensive per conjugated antibody	More cost-effective over multiple experiments
Best For	Quick, simple detection of abundant targets	Enhanced detection, multiplexed assays, low-abundance targets

1.1.3.2. Small-molecule Probes and Fluorescent Proteins

In addition to antibody conjugates, small-molecule fluorescent probes and fluorescent proteins are the other two widely used fluorescent probes in biological research. Small-molecule proteins that naturally have specificity to certain abundant targets (e.g., lipids, DNA, or proteins) are innately fluorescent or designed with binding moieties conjugated to fluorophores. Their small size offers unique advantages compared to larger antibody conjugates and exhibits fast, consistent binding across specimens. Examples include fluorescent phalloidin for actin[28], MitoTracker® dyes for mitochondria, and DNA-binding dyes like the Hoechst family[15]. These probes provide high specificity and sensitivity but may face challenges such as water solubility issues for lipophilic dyes or reduced signal-to-noise ratios for nucleic acid probes that bind both DNA and RNA. Despite these limitations, small-molecule probes remain a versatile and reliable choice for rapid labeling of various abundant biological components.

Fluorescent proteins, derived from green fluorescent protein (GFP) that was discovered from the *Aequorea Victoria* jellyfish in the 1960s [29] with engineered variants developed starting in the 1990s[30,31], revolutionized

biological imaging by enabling genetic tagging of target proteins in living systems. This approach eliminates the need for exogenous probes, allowing researchers to visualize protein distribution, track dynamic processes, and monitor interactions in live cells. Over the years, advancements in protein engineering have expanded the spectral range and applications of fluorescent proteins, making them widely adopted in research. However, their limitations include reduced brightness and photostability compared to organic dyes, poor performance in far-red and near-infrared regions, and challenges in non-model organisms or clinical specimens due to the need for genetic manipulation. Additionally, fluorescent proteins also face challenges on low expression efficiency and slow maturation period[32]. Despite these challenges, they remain a cornerstone of modern imaging techniques for studying complex biological systems.

1.1.3.3 Fluorophore and Fluorescence

Fluorescence is a physical property of molecules and atoms that absorb light at a specific wavelength and then emit that light at a longer wavelength. Fluorescence involves three primary stages: excitation, vibrational relaxation, and fluorescence emission[15].

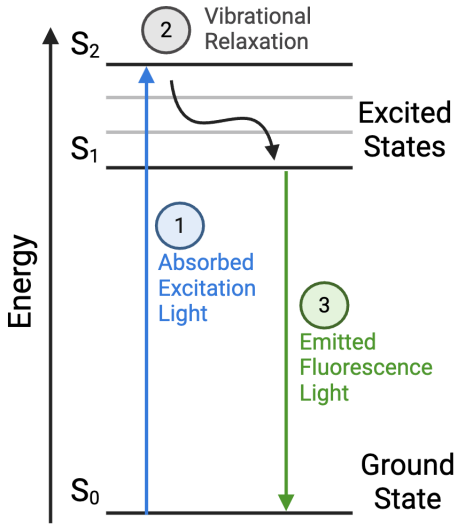

Figure 1.2. Jablonski diagram of fluorescence. *S_0, S_1, and S_2 represent the electronic states of a molecule. The molecule gets excited by light, reaches an excited state, and then releases the unstable energy through fluorescence.*

In the first stage, a fluorophore absorbs energy of a photon from an external light source, such as a laser or LED light, transitioning to an excited electronic singlet state. This process distinguishes fluorescence from

chemiluminescence, where chemical reactions create the excited state. In the second stage, the excited lifetime can last 1–10 nanoseconds, and the fluorophore undergoes conformational changes, interacts with its molecular environment, and produces a relaxed singlet excited state where fluorescence emission originates. However, not all molecules return to the ground state via fluorescence; instead, some fluorophores go through processes such as collisional quenching, fluorescence resonance energy transfer (FRET), and intersystem crossing to release the energy. The fluorescence quantum yield quantifies the balance of these competing processes by calculating the ratio of emitted fluorescence photons to absorbed photons. In the third stage, the fluorophore releases a lower-energy photon as it returns to the ground state. Energy dissipation during the excited-state lifetime results in this emitted photon having a longer wavelength than the excitation photon, a phenomenon known as the Stokes shift. The unique property of the Stokes shift allows for the enhancement of fluorescence detection sensitivity by separating the shorter excitation wavelength from the longer emission wavelength.

Fluorescence is a cyclical process unless the fluorophore is irreversibly damaged in the excited state, which is called photobleaching. A single fluorophore can emit thousands of photons, underpinning the high sensitivity of fluorescence techniques. A fluorophore's excitation spectrum typically mirrors its absorption spectrum, while the emission spectrum remains independent of the excitation wavelength due to energy dissipation during the excited-state lifetime. Emission intensity positively correlates with the excitation spectrum's amplitude at the excitation wavelength, enabling detailed fluorescence analysis.

1.1.4. Traditional Multiplexed Imaging

Traditional multiplexed imaging enables the detection of multiple targets simultaneously using different fluorescent markers, but it is limited by spectral overlap. The broad emission spectra and narrow Stokes shifts of typical fluorophores restrict the number of well-separated channels to ~5 within the visible and near-infrared (400–750 nm), complicating signal interpretation and reducing signal specificity. Careful selection and understanding of fluorophore excitation and emission spectra are essential for optimizing imaging protocols and minimizing these limitations. Moreover, the use of appropriate excitation filters, dichroic mirrors, and emission filters is crucial for accurately isolating the desired spectral band for each fluorophore. Applying sequential excitation and detection for each fluorophore instead of simultaneous excitation with multiple light sources is also necessary to minimize fluorescence crosstalk and background signals.

1.1.4.1. Spectral Overlap in Multiplexed Imaging

Spectral overlap occurs when multiple probes are used to simultaneously monitor different biomolecules on one specimen. The absorbance and emission spectra of multiple fluorophores overlap, which complicates the distinction between their signals and limits the number of fluorophores usable in a single experiment. This raises challenges for the clarity and accuracy of multiplexed imaging. Understanding each fluorophore's absorption and emission spectra is essential for effective experimental design. Below is an example of choosing the wrong fluorophore combination, which results in high cross-talk images.

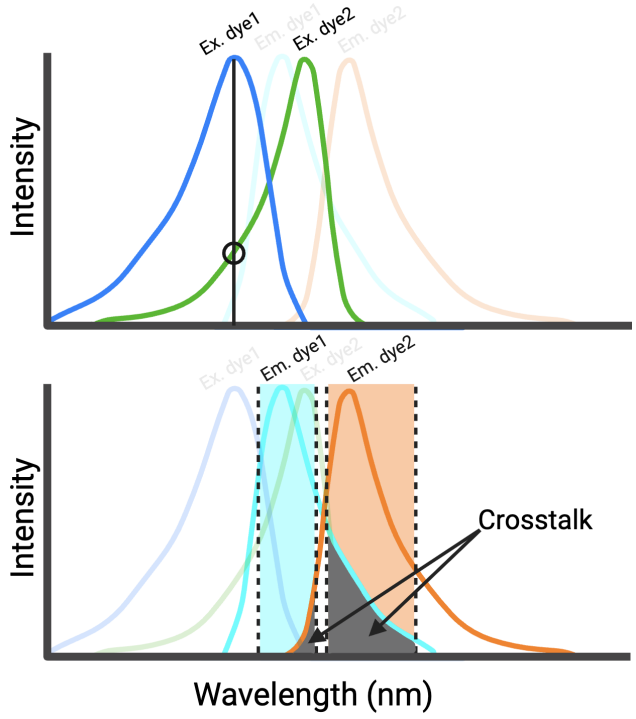

Figure 1.3. Co-excitation and cross-talk between two conventional fluorophores. *The top panel is the excitation spectra of two Dyes (Dye 1: blue, Dye 2: green). While the wavelength is optimal for exciting Dye 1 (black vertical line), it also partially excites Dye 2 (green curve), leading to co-excitation. Emission spectra for both dyes are faintly shown in the background to indicate their relative positions. The corresponding emission spectra (Dye 1: cyan, Dye 2: orange) are displayed, along with the defined detection channels (shaded boxes). Due to overlapping emission profiles, both dyes contribute fluorescence signals within each detection channel. The crosstalk (gray shaded region) arises when emission from Dye 1 is detected in the Dye 2 channel, and vice versa, complicating signal interpretation and reducing specificity.*

To get clean, well-separated single target images, using appropriate hardware setup and fluorophore combinations is sufficient for dealing with a sample that is stained with two to four fluorescent probes, but is insufficient for more than six fluorescent probes in use. Several spectral unmixing methodologies have been developed to address the challenges of spectral overlap based on the distinct emission spectra of each fluorophore. Unmixing becomes increasingly challenging as more fluorophores are added due to the increased complexity of the overlap. Recent computational advancements[33–38] have significantly enhanced these unmixing processes, leading to more accurate interpretations of collected data in complex biological samples (see **Chapter 1.2**).

1.1.4.2. Why Conventional Fluorophores Are Not Good for Large Stokes Shift.

Despite their wide use in fluorescence imaging, conventional small-molecule fluorophores have significant limitations in highly multiplexed imaging applications, particularly when large or variable Stokes shifts are required. These fluorophores generally have limited Stokes shifts, 10-50 nm[39], making them not optimal for imaging setups that require large shifts to reduce background signals and minimize channel cross-talk. The limited Stokes shifts arise from their rigid π-conjugated molecular structure that constrains the energy gap between electronic states and limits the vibrational relaxation before fluorescence emission[15]. Moreover, the fixed chemical structures of small-molecule dyes provide little flexibility for tuning excitation and emission spectra, which restricts adaptability to highly multiplexed systems[39].

1.2. Highly Multiplexed Fluorescence Microscopy Techniques

There is a growing need to measure multiple molecular targets simultaneously in complex biological systems in fields such as neuroscience, immunology, and oncology. Highly multiplexed imaging enables the simultaneous visualization of tens to a hundred biomarkers or molecular interactions in a single specimen, providing richer datasets and more comprehensive insights. This is particularly valuable in applications like tissue mapping or cancer diagnostics, where understanding the spatial distribution and interaction of tens of targets is crucial.

The following sections review the state-of-the-art technologies in the field that revolutionized the ability to visualize and quantify multiple targets in a single sample.

1.2.1. Existing Highly Multiplexed Imaging Approaches

1.2.1.1. Sequential Labeling and Imaging

A growingly popular family of approaches to highly multiplexed fluorescence microscopy uses sequential or iterative staining and multiplexed imaging, such as multiplexed immunofluorescence (MxIF)[17] and

tissue-based cyclic immunofluorescence (t-CyCIF)[40]. These methods avoid spectral overlap by chemically inactivating fluorescent dyes or removing antibodies to eliminate signals after each staining and imaging cycle, where a sample is stained and imaged multiple times with different fluorophores or antibodies. It is possible to observe up to 60 targets in a single tissue slide by using tens of rounds of cycled indirect immunofluorescence imaged over a period of 6-8 hours per cycle per day[40]. Despite the high number of targets, this cyclic approach has multiple challenges and limitations, including possible unsuccessful probe inactivation, extended incubation time and steps, restriction to imaging of thin tissues, and potential for tissue distortion between rounds.

A second group of sequential multiplexing techniques uses DNA-barcoded antibodies, such as co-detection by indexing (CODEX)[41] and immunostaining with signal amplification by exchange reaction (Immuno-SABER)[42]. These approaches use one-step immunostaining, followed by sequential barcode readout through annealing and stripping of complementary fluorescent oligonucleotides to DNA barcodes on tissue-bound antibodies. CODEX can detect up to ~100 targets in a single tissue section, but often depends on commercially prepared antibody panels, which may limit customization for specific experimental needs. Unlike traditional indirect immunofluorescence that uses secondary antibodies, no concerns related to species-to-species cross-linkages are involved, and it is able to detect multiple targets in a wide range of tissues, but this method is constrained by sample choices due to its limited signal-to-noise ratio throughputs. Tissues with a harsh fixation or with high autofluorescence are not preferred, and further amplification steps are needed.

Similarly, multiplexed transcriptomics methods exist to study the spatial distribution of mRNA at the single-cell level, such as multiplexed error-robust fluorescence in situ hybridization (MERFISH)[43] and sequential fluorescence in situ hybridization (seqFISH+)[44]. They also use a single round of probe staining but with pre-encoded barcodes of custom gene panels and followed by sequential rounds of imaging to read out the binary barcode and hence spatially localize transcripts and map gene expression across whole tissue. However, cyclic DNA readout requires complex computational probe design, customized automated hardware with fluidics, and computationally intensive analysis.

Table 1.3. Comparison of Sequential/Iterative Multiplexed Imaging Techniques

Category	Technique	How It Works	Pros	Cons
Cyclic Immunofluorescence	MxIF, t-CyCIF	Iterative staining and dye inactivation or antibody stripping	High multiplexing (up to ~60 targets), no spectral overlap	Long imaging cycles, possible tissue distortion, limited to thin tissue
DNA-Barcoded Antibodies	CODEX, Immuno-SABER	One-time antibody staining + cyclic DNA probe hybridization	Single-step staining, no species cross-reactivity, flexible imaging, high multiplexing (up to ~100 targets)	Sensitive to autofluorescence, lower SNR, more suited to soft tissues
Spatial Transcriptomics	MERFISH, seqFISH+	Pre-barcoded probes and sequential hybridization readout	High gene throughput (1000+), single-molecule resolution	Complex probe design, hardware demands, heavy computational analysis

1.2.1.2 Advanced computational spectral unmixing

Instead of a multi-round of staining or imaging, a single round of higher-plexed imaging is achievable with spectral unmixing that focuses on mathematical calculation and computational analysis to separate overlapped signals of each spectrum back into their corresponding channels[33]. An example of congested overlapping emission spectra of ten commonly used fluorophores is shown in **Figure 1.4**. Linear unmixing is one of the leading techniques in this field, which uses raw and mixed images to generate a reference matrix which helps in unmixing the original mixed images[33,34]. Compared to linear unmixing, Hyper-Spectral Phasors (HySP) and Blind source separation methods unmix signals without tedious pre-measurement of reference spectra. HySP applies Fourier transform on the emission spectra of each pixel to get a 2D phasor plot[35]. It enables rapid unmixing of 7 channels to obtain in vivo time-lapse images with a high signal-to-noise ratio and low autofluorescence background[36]. Blind source separation uses non-negative matrix factorization to determine matrix and unmixing images from raw data[37]. PICASSO is an advanced blind source separation method and it is able to unmix up to 15-channel multiplexed imaging of a mouse brain[38]. Although unmixing is typically constrained to ~6-8 channels, it still faces challenges caused by conventional fluorophores.

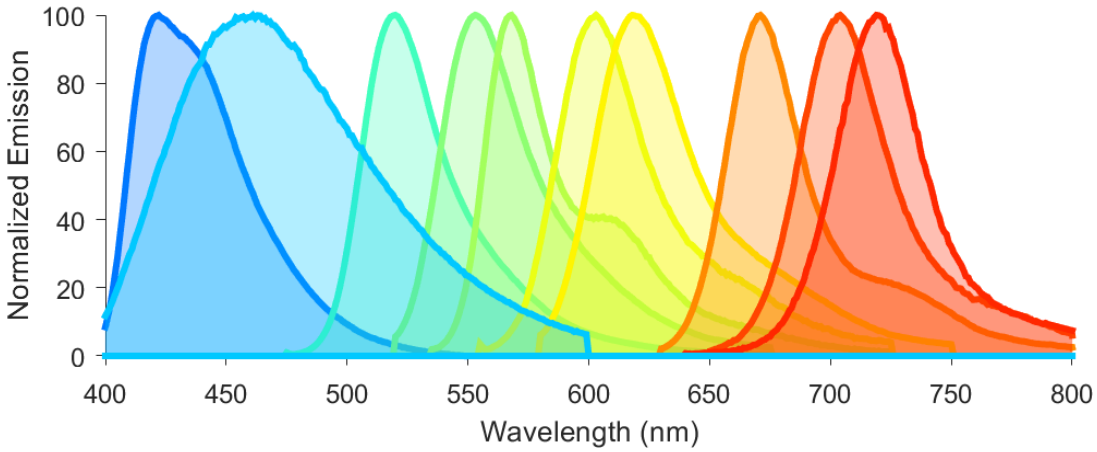

Figure 1.4. Congested overlapping spectra of ten conventional fluorophores. *Emission spectra for Alexa Fluor 405, DAPI, Alexa Fluor 488, Alexa Fluor 532, Alexa Fluor 555, Alexa Fluor 568, Alexa Fluor 594, Alexa Fluor 647, Alexa Fluor 680, and Alexa Fluor 700 respectively.*

1.2.1.3. Advanced fluorescent probes for highly multiplexed imaging

Besides the staining/imaging techniques and computational unmixing approaches, a high degree of multiplexed imaging can, in principle, also be achieved using advanced fluorescent probes with distinguishable excitation and emission properties. These fluorescent probes should include the following properties: a variable range of Stokes shifts, high photoluminescence quantum yield, ability to modify surface functional groups, enhanced photostability, and narrow excitation and emission spectral bands.

Conventional small-molecule dyes usually have a small Stokes shift around 20-30 nm and a ~40-50 nm FWHM spectral width, which limits the number of spectrally well-separated fluorophores across the visible region (400-750 nm) to about five. In recent studies, quantum dots (QDs) have gained attention as powerful probes for multiplexed bioimaging owing to their unique size-tunable emission properties[45]. However, achieving desirable fluorescent probe properties, such as improved quantum efficiency, high photostability, and long fluorescence lifetime, requires stringent control over synthesis parameters.

Another advanced fluorescent probe that has become an outstanding choice in recent years is spectrally tunable semiconducting nanoparticles called polymer dots (Pdots). These dots have a small particle size, with diameters as small as 5 nm to 30 nm, excellent fluorescence brightness, and variable Stokes shifts of 20 nm to 400 nm between excitation and emission peak wavelengths[46,47]. The high tunability of Pdot Stokes shifts offers wider spectral real estate for multiplexing that is challenging in traditional fluorescent dyes (see **Chapter 2**).

1.3. Thick tissue labeling and volumetric imaging techniques

Labeling thick tissue samples or even whole organ samples and imaging volumetrically are essential for preserving 3D spatial context of intact biological structures, which is critical for studying convoluted systems like neural networks, vasculature, or tumor microenvironments. However, achieving uniform antibody or probe penetration throughout thick or whole-organ samples remains a major challenge due to physical diffusion barriers, dense extracellular matrices, and limited molecular mobility. These constraints often result in uneven staining, long incubation times, and signal attenuation. To overcome these limitations, improvements in both imaging hardwares and tissue preparation procedures have been developed.

1.3.1. Tissue optical clearing methods

High-resolution imaging of intact biological tissues is often limited by absorption, light scattering, and tissue autofluorescence, which obscure structures deep within a sample (**Figure 1.5**). There are several factors that decrease clarity and depth. One significant issue is that fluorescence from out-of-focus regions creates high background noise and low image contrast. Another hindered issue is that biological tissues appear opaque because they are optically heterogeneous with varying refractive indices that scatter light, and contain pigments that absorb excitation light which further limits imaging depth. To address these challenges, LSFM is used to optically select and capture in-focus signals to improve image clarity, and tissue clearing methods have revolutionized deep imaging by rendering biological specimens more transparent, allowing light to penetrate more effectively[52–56]. The following sections will explore the three major types of tissue-clearing techniques, organic-based, water-based, and hydrogel-based methods (**Figure 1.6**).

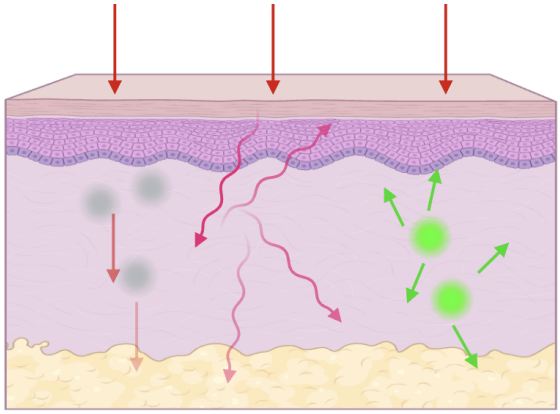

Figure 1.5. Illustration of different interactions between excitation light and biological tissues. *Absorption, scattering and autofluorescence are shown respectively.*

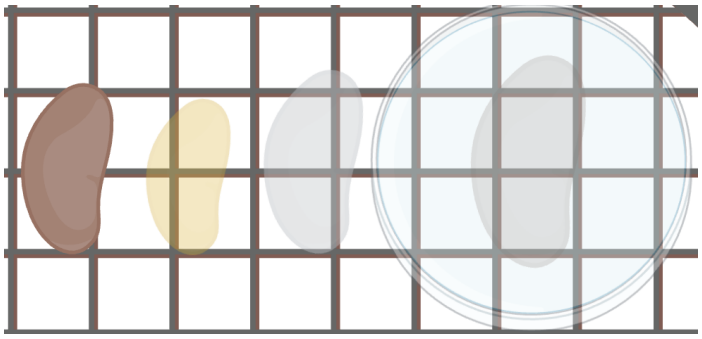

Figure 1.6. Cartoon illustration of kidney after different clearing methods. *From left to right are untreated kidney, kidney after organic-based clearing, water-based clearing, and hydrogel-based clearing methods respectively.*

1.3.1.1. Hydrophobic organic solvent-based methods

The organic solvent-based tissue-clearing approach follows two main steps: dehydration and delipidation, followed by refractive index (RI) matching. Water-miscible organic solvents like methanol or tetrahydrofuran (THF) are commonly used to remove water and lipids[57], the most abundant components in tissues, in order to improve optical homogeneity. This process leaves behind structures with a higher refractive index as proteins (RI = 1.55-1.56)[57,58], therefore necessitating the use of organic solvents with similarly high refractive indices for the final clearing step. Selecting proper solvents that also aid in lipid removal can further enhance transparency. Commonly used solvents include benzyl alcohol and benzyl ether. Several well-established protocols have been developed based on this method, such as BABB[59] and DISCO variants[54,58,60–62] (3DISCO, iDISCO, FDISCO, uDISCO), each offering specific advantages. 3DISCO[54] utilizes THF for efficient dehydration and delipidation, reducing background noise while improving fluorescence signals, achieving rapid and effective clearing of the mouse brain and spinal cord. iDISCO[60] incorporates a pre-treatment step with DMSO and Triton X-100 to enhance antibody penetration and immunolabeling. FDISCO[61] optimizes pH and temperature conditions to better preserve endogenous fluorescence over time. Meanwhile, uDISCO[62] facilitates significant tissue shrinkage, enabling whole-organ imaging within the working distance of a microscope, making it particularly useful for mapping neuronal and vascular networks in intact specimens. Despite their effectiveness, these approaches have limitations, like causing tissue shrinkage, and the reliance on toxic organic solvents, which poses safety and handling concerns.

1.3.1.2. Hydrophilic aqueous solvent-based methods

Hydrophilic, or aqueous-based, tissue clearing methods utilize water-soluble reagents to achieve delipidation, hyperhydration, and RI (refractive index) matching while preserving structural and fluorescent integrity[57]. These approaches are well-suited for use with fluorescent proteins and tend to cause less tissue shrinkage than hydrophobic organic solvent-based methods. Both hydrophilic and hydrophobic techniques begin with delipidation, but aqueous methods use mild detergents like Triton X-100 instead of harsh water-miscible solvents. A key advantage of hydrophilic clearing lies in the hyperhydration step, where substances like urea hydrate hydrophobic protein regions, lowering the tissue's RI to approximate that of water (~1.33)[58]. This RI matching allows for compatibility with water-immersion objective lenses. One of the prominent hydrophilic methods, CUBIC[52,63,64] (Clear, Unobstructed Brain/Body Imaging Cocktails and Computational Analysis), uses two chemical cocktails—one for delipidation and decolorization, and another for RI matching and structural preservation. CUBIC uses of amino alcohols, such as Quadrol (N,N,N',N'-tetrakis(2-hydroxypropyl) ethylenediamine) and TEA (triethanolamine), helps decolorize heme-containing tissues, enhancing optical clarity. Additionally, sucrose is included to counteract sample swelling from urea. While highly effective, aqueous-based clearing often requires extended processing times and is most commonly applied to lipid-rich organs and whole organisms.

1.3.1.3. Hydrogel embedding-based methods

Hydrogel-based tissue clearing methods, first proposed by Chung et al. in 2013 with the introduction of CLARITY[55,65], represent a distinct approach that preserves tissue structure while enabling high-resolution imaging and molecular labeling. These techniques embed biological samples in a polyacrylamide-based hydrogel, which forms covalent bonds with proteins, nucleic acids, and other biomolecules, thus maintaining their spatial organization during lipid removal. The process typically involves three steps: hydrogel embedding, lipid extraction using ionic detergents like sodium dodecyl sulfate (SDS), and RI matching to achieve transparency. Because the hydrogel stabilizes the tissue matrix, endogenous fluorescence is well preserved, and samples can undergo multiple rounds of staining and imaging. Lipid removal can be accelerated using electrophoresis, though this "active CLARITY" approach[65] may compromise protein integrity. To address this, improved passive methods like PACT[66] have been developed, optimizing hydrogel composition for better permeability and more efficient passive lipid removal while also offering adjustable RI matching solutions tailored to different sample types. Notably, Expansion Microscopy (ExM)[67] , introduced by the Boyden lab in 2015, also used hydrogel-embedding principle. In addition to enabling nanoscale resolution through physical expansion of the tissue, ExM inherently improves optical clarity by diluting dense tissue components during expansion, reducing light

scattering and tissue autofluorescence[68]. Despite its advantages of superior molecular preservation and the ability to perform repeated labeling, hydrogel-based clearing is technically complex and time-consuming compared to hydrophilic and hydrophobic methods.

1.3.2. Light sheet microscopy

Traditional fluorescence microscopy techniques, such as widefield and confocal microscopy, as mentioned in the previous sections, have been widely employed for imaging thin biological specimens. While these methods provide high x-y spatial resolution, they suffer limitations such as out-of-focus light contamination in widefield microscopy and photobleaching due to point-scanning in confocal microscopy[5–7]. These limitations make it challenging to efficiently image thick or optically dense specimens in three dimensions.

To overcome these challenges, light sheet fluorescence microscopy (LSFM) has emerged as a powerful alternative[8]. One of the LSFM variations is the open-top light sheet microscope (OTLS)[48], which enables efficient optical sectioning, reduced phototoxicity, improved imaging depth, and high throughput. Unlike most other LSFM designs that require specimen embedding within a chamber[49], OTLS employs an inverted geometry that allows samples to be placed on a glass platform. The setup is similar to a flat-bed document scanner by placing all optical components below the sample holder, which simplifies sample mounting procedures and enables seamless integration with tissue-clearing techniques[50]. By illuminating the sample with a thin sheet of light that excites fluorescence selectively within the focal plane, OTLS achieves excellent optical sectioning, minimizing out-of-focus blur and photodamage while maximizing signal-to-noise ratio[10,51]. These advantages make OTLS particularly useful for applications such as whole-organ imaging, pathology, and neuroscience, where detailed three-dimensional visualization of tissue architecture is essential.

1.3.3. Thick tissue immunostaining

The combination of light-sheet microscopy and advanced tissue-clearing techniques enables deep, high-resolution imaging of intact samples. The next critical step is thick tissue immunostaining, which enables 3D labeling of specific molecules and structures within optically transparent tissues. Immunostaining thick tissues presents challenges due to limited antibody penetration. Passive staining relies on the diffusion of antibodies into the tissue, which can be time-consuming, from weeks to months, and may result in uneven labeling which leads to increased noise and artifacts and decreased overall quality of the imaging analysis. Various active staining methods have been developed to overcome these problems to achieve efficient and uniform immunolabeling in thick, optically cleared tissues.

Each advanced passive or active labeling method used distinct strategies to address the inherent limitations of antibody diffusion, tissue permeability, and uneven staining. For passive labeling methods, antibody penetration relies on diffusion, which often requires extended incubation times, especially for thick samples, since diffusion time scales with the square of the distance to be traveled. Although slower, these methods are generally less likely to damage tissue structure. Several notable strategies have been developed to enhance penetration efficiency. SWITCH[69] controls antibody-antigen binding affinity by alternating ON/OFF states using SDS detergent and different temperatures. SHANEL[70] uses a combination of Quadrol and CHAPS that forms smaller micelles to facilitate permeabilization of dense adult human tissues, enabling whole-organ immunolabeling. CUBIC-HistoVIsion[26] incorporates proprietary penetration enhancers, HV-additives, to facilitate deeper and more uniform antibody distribution in whole organ scale. SPEARs[71] introduces antibody stabilization under elevated temperatures (~37–55 °C), which accelerates staining while maintaining antibody functionality for efficient deep penetration. ELAST[72] offers new means of accelerating antibody delivery through reversibly stretching tissue to a thin sheet to physically decrease the tissue thickness.

In contrast, active labeling methods use external forces to drive antibody penetration more rapidly and uniformly. CLARITY[65,73] applies electrophoresis and SDS in a polyacrylamide matrix to actively extract lipids and accelerate antibody diffusion that might cause heating, tissue distortion, or risk of protein loss. Whereas eFLASH[74] further improves this by applying optimized, enhanced electric fields for faster and more uniform antibody penetration with less tissue damage. EERS[75] uses a low-intensity electric field to enhance diffusion gently without tissue damage or structural integrity. Similarly, CuRVE[76] maintains a dynamic equilibrium between antibody diffusion and binding reactions to uniformly distribute antibodies throughout the tissue by incorporating stochastic electrotransport to further facilitate antibody movement.

Together with tissue-clearing techniques, these advanced immunolabeling methods significantly expand the boundaries of deep-tissue immunolabeling for comprehensive volumetric imaging at the whole organ or even whole-body scales.

1.4. Summary

The merging of fluorescent probes, advanced labeling strategies, innovative microscopy designs, and various tissue-clearing methods has revolutionized the field of multiplexed and volumetric imaging. These advancements have enabled researchers to visualize complex biological structures in a higher dimension, facilitating deeper insights into tissue architecture and function. In Chapter 2, a novel fluorescent semiconducting polymer dots for highly multiplexed imaging and its application on fluorescence

microscopy on thin mouse tissues will be discussed. In Chapter 3, this multiplexing method is extended into three-dimensional space by integrating polymer dot labeling with light sheet fluorescence microscopy and tissue clearing techniques, enabling rapid and highly multiplexed imaging of thick tissues and whole organs. Together, these efforts provide a versatile imaging platform for mapping molecular landscapes across spatial scales.

1.5. Reference

(1) Shotton, D. M. Confocal Scanning Optical Microscopy and Its Applications for Biological Specimens. *J. Cell Sci.* **1989**, *94* (2), 175–206. https://doi.org/10.1242/jcs.94.2.175.
(2) Masters, B. R. History of the Optical Microscope in Cell Biology and Medicine. In *Encyclopedia of Life Sciences*; Wiley, 2008. https://doi.org/10.1002/9780470015902.a0003082.
(3) Thorn, K. A Quick Guide to Light Microscopy in Cell Biology. *Mol. Biol. Cell* **2016**, *27* (2), 219–222. https://doi.org/10.1091/mbc.e15-02-0088.
(4) Palima, D.; Glückstad, J. Generalised Phase Contrast: Microscopy, Manipulation and More. *Contemp. Phys.* **2010**, *51* (3), 249–265. https://doi.org/10.1080/00107510903462257.
(5) Jonkman, J.; Brown, C. M.; Wright, G. D.; Anderson, K. I.; North, A. J. Tutorial: Guidance for Quantitative Confocal Microscopy. *Nat. Protoc.* **2020**, *15* (5), 1585–1611. https://doi.org/10.1038/s41596-020-0313-9.
(6) St. Croix, C. M.; Shand, S. H.; Watkins, S. C. Confocal Microscopy: Comparisons, Applications, and Problems. *BioTechniques* **2005**, *39* (sup6), 1. https://doi.org/10.2144/000112089.
(7) Halpern, A. R.; Halpern, A. R.; Lee, M. Y.; Howard, M. D.; Woodworth, M. A.; Nicovich, P. R.; Vaughan, J. C. Versatile, Do-It-Yourself, Low-Cost Spinning Disk Confocal Microscope. *Biomed. Opt. Express* **2022**, *13* (2), 1102–1120. https://doi.org/10.1364/BOE.442087.
(8) Santi, P. A. Light Sheet Fluorescence Microscopy: A Review. *J. Histochem. Cytochem.* **2011**, *59* (2), 129–138. https://doi.org/10.1369/0022155410394857.
(9) Power, R. M.; Huisken, J. A Guide to Light-Sheet Fluorescence Microscopy for Multiscale Imaging. *Nat. Methods* **2017**, *14* (4), 360–373. https://doi.org/10.1038/nmeth.4224.
(10) Liu, J. T. C.; Glaser, A. K.; Poudel, C.; Vaughan, J. C. Nondestructive 3D Pathology with Light-Sheet Fluorescence Microscopy for Translational Research and Clinical Assays. *Annu. Rev. Anal. Chem.* **2023**, *16* (1), 231–252. https://doi.org/10.1146/annurev-anchem-091222-092734.
(11) Hobson, C. M.; Guo, M.; Vishwasrao, H. D.; Wu, Y.; Shroff, H.; Chew, T.-L. Practical Considerations for Quantitative Light Sheet Fluorescence Microscopy. *Nat. Methods* **2022**, *19* (12), 1538–1549. https://doi.org/10.1038/s41592-022-01632-x.
(12) Liu, J. T. C.; Glaser, A. K.; Bera, K.; True, L. D.; Reder, N. P.; Eliceiri, K. W.; Madabhushi, A. Harnessing Non-Destructive 3D Pathology. *Nat. Biomed. Eng.* **2021**. https://doi.org/10.1038/s41551-020-00681-x.
(13) Lichtman, J. W.; Conchello, J.-A. Fluorescence Microscopy. *Nat. Methods* **2005**, *2* (12), 910–919. https://doi.org/10.1038/nmeth817.
(14) Renz, M. Fluorescence Microscopy-A Historical and Technical Perspective: Fluorescence Microscopy. *Cytometry A* **2013**, *83* (9), 767–779. https://doi.org/10.1002/cyto.a.22295.
(15) *The Molecular Probes Handbook: A Guide to Fluorescent Probes and Labeling Technologies*, 11. ed.; Johnson, I., Ed.; Life Technologies: Carlsbad, Calif., 2010.
(16) Terai, T.; Nagano, T. Small-Molecule Fluorophores and Fluorescent Probes for Bioimaging. *Pflüg. Arch. - Eur. J. Physiol.* **2013**, *465* (3), 347–359. https://doi.org/10.1007/s00424-013-1234-z.
(17) Gerdes, M. J.; Sevinsky, C. J.; Sood, A.; Adak, S.; Bello, M. O.; Bordwell, A.; Can, A.; Corwin, A.; Dinn, S.; Filkins, R. J.; others. Highly Multiplexed Single-Cell Analysis of Formalin-Fixed, Paraffin-Embedded Cancer Tissue. *Proc. Natl. Acad. Sci.* **2013**, *110* (29), 11982–11987.

(18) Piston, D. Imaging Living Cells and Tissues by Two-Photon Excitation Microscopy. *Trends Cell Biol.* **1999**, *9* (2), 66–69. https://doi.org/10.1016/S0962-8924(98)01432-9.
(19) Luu, P.; Fraser, S. E.; Schneider, F. More than Double the Fun with Two-Photon Excitation Microscopy. *Commun. Biol.* **2024**, *7* (1), 364. https://doi.org/10.1038/s42003-024-06057-0.
(20) Zhu, H.; Fan, J.; Du, J.; Peng, X. Fluorescent Probes for Sensing and Imaging within Specific Cellular Organelles. *Acc. Chem. Res.* **2016**, *49* (10), 2115–2126. https://doi.org/10.1021/acs.accounts.6b00292.
(21) Kolanowski, J. L.; Liu, F.; New, E. J. Fluorescent Probes for the Simultaneous Detection of Multiple Analytes in Biology. *Chem. Soc. Rev.* **2018**, *47* (1), 195–208. https://doi.org/10.1039/C7CS00528H.
(22) Rust, M. J.; Bates, M.; Zhuang, X. Sub-Diffraction-Limit Imaging by Stochastic Optical Reconstruction Microscopy (STORM). *Nat. Methods* **2006**, *3* (10), 793–796.
(23) Basu, K.; Green, E. M.; Cheng, Y.; Craik, C. S. Why Recombinant Antibodies — Benefits and Applications. *Curr. Opin. Biotechnol.* **2019**, *60*, 153–158. https://doi.org/10.1016/j.copbio.2019.01.012.
(24) Hermanson, G. Bioconjugate Techniques, 3rd Edition. In *Bioconjugate Techniques*; Elsevier, 2013; pp 1017–1094. https://doi.org/10.1016/B978-0-12-382239-0.00036-4.
(25) *Biobanking: Methods and Protocols*; Yong, W. H., Ed.; Methods in Molecular Biology; Springer New York: New York, NY, 2019; Vol. 1897. https://doi.org/10.1007/978-1-4939-8935-5.
(26) Susaki, E. A.; Shimizu, C.; Kuno, A.; Tainaka, K.; Li, X.; Nishi, K.; Morishima, K.; Ono, H.; Ode, K. L.; Saeki, Y.; Miyamichi, K.; Isa, K.; Yokoyama, C.; Kitaura, H.; Ikemura, M.; Ushiku, T.; Shimizu, Y.; Saito, T.; Saido, T. C.; Fukayama, M.; Onoe, H.; Touhara, K.; Isa, T.; Kakita, A.; Shibayama, M.; Ueda, H. R. Versatile Whole-Organ/Body Staining and Imaging Based on Electrolyte-Gel Properties of Biological Tissues. *Nat. Commun.* **2020**, *11* (1), 1982. https://doi.org/10.1038/s41467-020-15906-5.
(27) Bradbury, A.; Plückthun, A. Reproducibility: Standardize Antibodies Used in Research. *Nature* **2015**, *518* (7537), 27–29. https://doi.org/10.1038/518027a.
(28) Wulf, E.; Deboben, A.; Bautz, F. A.; Faulstich, H.; Wieland, T. Fluorescent Phallotoxin, a Tool for the Visualization of Cellular Actin. *Proc. Natl. Acad. Sci.* **1979**, *76* (9), 4498–4502.
(29) Zimmer, M. GFP: From Jellyfish to the Nobel Prize and Beyond. *Chem. Soc. Rev.* **2009**, *38* (10), 2823. https://doi.org/10.1039/b904023d.
(30) Chalfie, M.; Tu, Y.; Euskirchen, G.; Ward, W. W.; Prasher, D. C. Green Fluorescent Protein as a Marker for Gene Expression. *Science* **1994**, *263*, 802–805.
(31) Tsien, R. Y. The Green Fluorescent Protein. *Annu. Rev. Biochem.* **1998**, *67* (1), 509–544.
(32) Balleza, E.; Kim, J. M.; Cluzel, P. Systematic Characterization of Maturation Time of Fluorescent Proteins in Living Cells. *Nat. Methods* **2018**, *15* (1), 47–51. https://doi.org/10.1038/nmeth.4509.
(33) Zimmermann, T.; Marrison, J.; Hogg, K.; O'Toole, P. Clearing Up the Signal: Spectral Imaging and Linear Unmixing in Fluorescence Microscopy. In *Confocal Microscopy*; Paddock, S. W., Ed.; Methods in Molecular Biology; Springer New York: New York, NY, 2014; Vol. 1075, pp 129–148. https://doi.org/10.1007/978-1-60761-847-8_5.
(34) Alterman, M.; Schechner, Y. Y.; Weiss, A. Multiplexed Fluorescence Unmixing. In *2010 IEEE International Conference on Computational Photography (ICCP)*; IEEE: Cambridge, MA, USA, 2010; pp 1–8. https://doi.org/10.1109/ICCPHOT.2010.5585093.
(35) Fereidouni, F.; Bader, A. N.; Gerritsen, H. C. Spectral Phasor Analysis Allows Rapid and Reliable Unmixing of Fluorescence Microscopy Spectral Images. *Opt. Express* **2012**, *20* (12), 12729. https://doi.org/10.1364/OE.20.012729.
(36) Cutrale, F.; Trivedi, V.; Trinh, L. A.; Chiu, C.-L.; Choi, J. M.; Artiga, M. S.; Fraser, S. E. Hyperspectral Phasor Analysis Enables Multiplexed 5D in Vivo Imaging. *Nat. Methods* **2017**, *14* (2), 149–152. https://doi.org/10.1038/nmeth.4134.
(37) Neher, R. A.; Mitkovski, M.; Kirchhoff, F.; Neher, E.; Theis, F. J.; Zeug, A. Blind Source Separation Techniques for the Decomposition of Multiply Labeled Fluorescence Images. *Biophys. J.* **2009**, *96* (9), 3791–3800. https://doi.org/10.1016/j.bpj.2008.10.068.

(38) Seo, J.; Sim, Y.; Kim, J.; Kim, H.; Cho, I.; Nam, H.; Yoon, Y.-G.; Chang, J.-B. PICASSO Allows Ultra-Multiplexed Fluorescence Imaging of Spatially Overlapping Proteins without Reference Spectra Measurements. *Nat. Commun.* **2022**, *13* (1), 2475. https://doi.org/10.1038/s41467-022-30168-z.
(39) Lavis, L. D.; Raines, R. T. Bright Ideas for Chemical Biology. *ACS Chem. Biol.* **2008**, *3* (3), 142–155. https://doi.org/10.1021/cb700248m.
(40) Lin, J.-R.; Izar, B.; Wang, S.; Yapp, C.; Mei, S.; Shah, P. M.; Santagata, S.; Sorger, P. K. Highly Multiplexed Immunofluorescence Imaging of Human Tissues and Tumors Using T-CyCIF and Conventional Optical Microscopes. *eLife* **2018**, *7*, e31657. https://doi.org/10.7554/eLife.31657.
(41) Goltsev, Y.; Samusik, N.; Kennedy-Darling, J.; Bhate, S.; Hale, M.; Vazquez, G.; Black, S.; Nolan, G. P. Deep Profiling of Mouse Splenic Architecture with CODEX Multiplexed Imaging. *Cell* **2018**, *174* (4), 968-981.e15. https://doi.org/10.1016/j.cell.2018.07.010.
(42) Saka, S. K.; Wang, Y.; Kishi, J. Y.; Zhu, A.; Zeng, Y.; Xie, W.; Kirli, K.; Yapp, C.; Cicconet, M.; Beliveau, B. J.; Lapan, S. W.; Yin, S.; Lin, M.; Boyden, E. S.; Kaeser, P. S.; Pihan, G.; Church, G. M.; Yin, P. Immuno-SABER Enables Highly Multiplexed and Amplified Protein Imaging in Tissues. *Nat. Biotechnol.* **2019**, 1–11. https://doi.org/10.1038/s41587-019-0207-y.
(43) Xia, C.; Babcock, H. P.; Moffitt, J. R.; Zhuang, X. Multiplexed Detection of RNA Using MERFISH and Branched DNA Amplification. *Sci. Rep.* **2019**, *9* (1), 7721. https://doi.org/10.1038/s41598-019-43943-8.
(44) Eng, C.-H. L.; Lawson, M.; Zhu, Q.; Dries, R.; Koulena, N.; Takei, Y.; Yun, J.; Cronin, C.; Karp, C.; Yuan, G.-C.; Cai, L. Transcriptome-Scale Super-Resolved Imaging in Tissues by RNA seqFISH+. *Nature* **2019**, *568* (7751), 235–239. https://doi.org/10.1038/s41586-019-1049-y.
(45) Zhou, J.; Yang, Y.; Zhang, C. Toward Biocompatible Semiconductor Quantum Dots: From Biosynthesis and Bioconjugation to Biomedical Application. *Chem. Rev.* **2015**, *115* (21), 11669–11717. https://doi.org/10.1021/acs.chemrev.5b00049.
(46) Wu, C.; Chiu, D. T. Highly Fluorescent Semiconducting Polymer Dots for Biology and Medicine. *Angew. Chem. Int. Ed.* **2013**, *52* (11), 3086–3109. https://doi.org/10.1002/anie.201205133.
(47) Guo, Z.; Poudel, C.; Sarfatis, M. C.; Yu, J.; Wong, M.; Chiu, D. T.; Vaughan, J. C. Highly Multiplexed Fluorescence Microscopy with Spectrally Tunable Semiconducting Polymer Dots. *ScienceAdvances* **2024**.
(48) Glaser, A. K.; Bishop, K. W.; Barner, L. A.; Susaki, E. A.; Kubota, S. I.; Gao, G.; Serafin, R. B.; Balaram, P.; Turschak, E.; Nicovich, P. R.; Lai, H.; Lucas, L. A. G.; Yi, Y.; Nichols, E. K.; Huang, H.; Reder, N. P.; Wilson, J. J.; Sivakumar, R.; Shamskhou, E.; Stoltzfus, C. R.; Wei, X.; Hempton, A. K.; Pende, M.; Murawala, P.; Dodt, H.-U.; Imaizumi, T.; Shendure, J.; Beliveau, B. J.; Gerner, M. Y.; Xin, L.; Zhao, H.; True, L. D.; Reid, R. C.; Chandrashekar, J.; Ueda, H. R.; Svoboda, K.; Liu, J. T. C. A Hybrid Open-Top Light-Sheet Microscope for Versatile Multi-Scale Imaging of Cleared Tissues. *Nat. Methods* **2022**, *19* (5), 613–619. https://doi.org/10.1038/s41592-022-01468-5.
(49) Albert-Smet, I.; Marcos-Vidal, A.; Vaquero, J. J.; Desco, M.; Muñoz-Barrutia, A.; Ripoll, J. Applications of Light-Sheet Microscopy in Microdevices. *Front. Neuroanat.* **2019**, *13*, 1. https://doi.org/10.3389/fnana.2019.00001.
(50) Glaser, A. K.; Reder, N. P.; Chen, Y.; Yin, C.; Wei, L.; Kang, S.; Barner, L. A.; Xie, W.; McCarty, E. F.; Mao, C.; Halpern, A. R.; Stoltzfus, C. R.; Daniels, J. S.; Gerner, M. Y.; Nicovich, P. R.; Vaughan, J. C.; True, L. D.; Liu, J. T. C. Multi-Immersion Open-Top Light-Sheet Microscope for High-Throughput Imaging of Cleared Tissues. *Nat. Commun.* **2019**, *10* (1), 2781. https://doi.org/10.1038/s41467-019-10534-0.
(51) Park, S.; Na, M.; Chang, S.; Kim, K. H. High-Resolution Open-Top Axially Swept Light Sheet Microscopy. *BMC Biol.* **2023**, *21* (1), 248. https://doi.org/10.1186/s12915-023-01747-3.
(52) Susaki, E. A.; Tainaka, K.; Perrin, D.; Kishino, F.; Tawara, T.; Watanabe, T. M.; Yokoyama, C.; Onoe, H.; Eguchi, M.; Yamaguchi, S.; Abe, T.; Kiyonari, H.; Shimizu, Y.; Miyawaki, A.; Yokota, H.; Ueda, H. R. Whole-Brain Imaging with Single-Cell Resolution Using Chemical Cocktails and Computational Analysis. *Cell* **2014**, *157* (3), 726–739. https://doi.org/10.1016/j.cell.2014.03.042.
(53) Tainaka, K.; Kuno, A.; Kubota, S. I.; Murakami, T.; Ueda, H. R. Chemical Principles in Tissue

Clearing and Staining Protocols for Whole-Body Cell Profiling. *Annu. Rev. Cell Dev. Biol.* **2016**, *32* (1), 713–741. https://doi.org/10.1146/annurev-cellbio-111315-125001.
(54) Ertürk, A.; Becker, K.; Jährling, N.; Mauch, C. P.; Hojer, C. D.; Egen, J. G.; Hellal, F.; Bradke, F.; Sheng, M.; Dodt, H.-U. Three-Dimensional Imaging of Solvent-Cleared Organs Using 3DISCO. *Nat. Protoc.* **2012**, *7* (11), 1983–1995. https://doi.org/10.1038/nprot.2012.119.
(55) Chung, K.; Wallace, J.; Kim, S.-Y.; Kalyanasundaram, S.; Andalman, A. S.; Davidson, T. J.; Mirzabekov, J. J.; Zalocusky, K. A.; Mattis, J.; Denisin, A. K.; Pak, S.; Bernstein, H.; Ramakrishnan, C.; Grosenick, L.; Gradinaru, V.; Deisseroth, K. Structural and Molecular Interrogation of Intact Biological Systems. *Nature* **2013**, *497* (7449), 332–337. https://doi.org/10.1038/nature12107.
(56) Tainaka, K.; Murakami, T. C.; Susaki, E. A.; Shimizu, C.; Saito, R.; Takahashi, K.; Hayashi-Takagi, A.; Sekiya, H.; Arima, Y.; Nojima, S.; Ikemura, M.; Ushiku, T.; Shimizu, Y.; Murakami, M.; Tanaka, K. F.; Iino, M.; Kasai, H.; Sasaoka, T.; Kobayashi, K.; Miyazono, K.; Morii, E.; Isa, T.; Fukayama, M.; Kakita, A.; Ueda, H. R. Chemical Landscape for Tissue Clearing Based on Hydrophilic Reagents. *Cell Rep.* **2018**, *24* (8), 2196-2210.e9. https://doi.org/10.1016/j.celrep.2018.07.056.
(57) Richardson, D. S.; Lichtman, J. W. Clarifying Tissue Clearing. *Cell* **2015**, *162* (2), 246–257. https://doi.org/10.1016/j.cell.2015.06.067.
(58) Molbay, M.; Kolabas, Z. I.; Todorov, M. I.; Ohn, T.; Ertürk, A. A Guidebook for DISCO Tissue Clearing. *Mol. Syst. Biol.* **2021**, *17* (3). https://doi.org/10.15252/msb.20209807.
(59) Dodt, H.-U.; Leischner, U.; Schierloh, A.; Jährling, N.; Mauch, C. P.; Deininger, K.; Deussing, J. M.; Eder, M.; Zieglgänsberger, W.; Becker, K. Ultramicroscopy: Three-Dimensional Visualization of Neuronal Networks in the Whole Mouse Brain. *Nat. Methods* **2007**, *4* (4), 331–336. https://doi.org/10.1038/nmeth1036.
(60) Renier, N.; Wu, Z.; Simon, D. J.; Yang, J.; Ariel, P.; Tessier-Lavigne, M. iDISCO: A Simple, Rapid Method to Immunolabel Large Tissue Samples for Volume Imaging. *Cell* **2014**, *159* (4), 896–910. https://doi.org/10.1016/j.cell.2014.10.010.
(61) Qi, Y.; Yu, T.; Xu, J.; Wan, P.; Ma, Y.; Zhu, J.; Li, Y.; Gong, H.; Luo, Q.; Zhu, D. FDISCO: Advanced Solvent-Based Clearing Method for Imaging Whole Organs. *Sci. Adv.* **2019**, *5* (1), eaau8355. https://doi.org/10.1126/sciadv.aau8355.
(62) Pan, C.; Cai, R.; Quacquarelli, F. P.; Ghasemigharagoz, A.; Lourbopoulos, A.; Matryba, P.; Plesnila, N.; Dichgans, M.; Hellal, F.; Ertürk, A. Shrinkage-Mediated Imaging of Entire Organs and Organisms Using uDISCO. *Nat. Methods* **2016**, *13* (10), 859–867. https://doi.org/10.1038/nmeth.3964.
(63) Hasegawa, S.; Susaki, E. A.; Tanaka, T.; Komaba, H.; Wada, T.; Fukagawa, M.; Ueda, H. R.; Nangaku, M. Comprehensive Three-Dimensional Analysis (CUBIC-Kidney) Visualizes Abnormal Renal Sympathetic Nerves after Ischemia/Reperfusion Injury. *Kidney Int.* **2019**, *96* (1), 129–138. https://doi.org/10.1016/j.kint.2019.02.011.
(64) Nojima, S.; Susaki, E. A.; Yoshida, K.; Takemoto, H.; Tsujimura, N.; Iijima, S.; Takachi, K.; Nakahara, Y.; Tahara, S.; Ohshima, K.; Kurashige, M.; Hori, Y.; Wada, N.; Ikeda, J.; Kumanogoh, A.; Morii, E.; Ueda, H. R. CUBIC Pathology: Three-Dimensional Imaging for Pathological Diagnosis. *Sci. Rep.* **2017**, *7* (1). https://doi.org/10.1038/s41598-017-09117-0.
(65) Tomer, R.; Ye, L.; Hsueh, B.; Deisseroth, K. Advanced CLARITY for Rapid and High-Resolution Imaging of Intact Tissues. *Nat. Protoc.* **2014**, *9* (7), 1682–1697. https://doi.org/10.1038/nprot.2014.123.
(66) Jin, B.-H.; Woo, J.; Lee, M.; Ku, S.; Moon, H. S.; Ryu, S. J.; Hyun, Y.-M.; Park, J.-Y.; Kuh, S. U.; Cho, Y. E. Optimization of the Optical Transparency of Bones by PACT-Based Passive Tissue Clearing. *Exp. Mol. Med.* **2023**, *55* (10), 2190–2204. https://doi.org/10.1038/s12276-023-01089-8.
(67) Chen, F.; Tillberg, P. W.; Boyden, E. S. Expansion Microscopy. *Science* **2015**, *347* (6221), 543–548. https://doi.org/10.1126/science.1260088.
(68) Chozinski, T. J.; Halpern, A. R.; Okawa, H.; Kim, H.-J.; Tremel, G. J.; Wong, R. O. L.; Vaughan, J. C. Expansion Microscopy with Conventional Antibodies and Fluorescent Proteins. *Nat. Methods* **2016**, *13* (6), 485–488. https://doi.org/10.1038/nmeth.3833.
(69) Murray, E.; Cho, J. H.; Goodwin, D.; Ku, T.; Swaney, J.; Kim, S.-Y.; Choi, H.; Park, Y.-G.; Park,

J.-Y.; Hubbert, A.; McCue, M.; Vassallo, S.; Bakh, N.; Frosch, M. P.; Wedeen, V. J.; Seung, H. S.; Chung, K. Simple, Scalable Proteomic Imaging for High-Dimensional Profiling of Intact Systems. *Cell* **2015**, *163* (6), 1500–1514. https://doi.org/10.1016/j.cell.2015.11.025.
(70) Mai, H.; Rong, Z.; Zhao, S.; Cai, R.; Steinke, H.; Bechmann, I.; Ertürk, A. Scalable Tissue Labeling and Clearing of Intact Human Organs. *Nat. Protoc.* **2022**, *17* (10), 2188–2215. https://doi.org/10.1038/s41596-022-00712-8.
(71) Lai, H. M.; Tang, Y.; Lau, Z. Y. H.; Campbell, R. A. A.; Yau, J. C. N.; Chan, C. C. Y.; Chan, D. C. W.; Wong, T. Y.; Wong, H. K. T.; Yan, L. Y. C.; Wu, W. K. K.; Wong, S. H.; Kwok, K.-W.; Wing, Y.-K.; Lam, H. H. N.; Ng, H.-K.; Mrsic-Flogel, T. D.; Mok, V. C. T.; Chan, J. Y. K.; Ko, H. Antibody Stabilization for Thermally Accelerated Deep Immunostaining. *Nat. Methods* **2022**, *19* (9), 1137–1146. https://doi.org/10.1038/s41592-022-01569-1.
(72) Ku, T.; Guan, W.; Evans, N. B.; Sohn, C. H.; Albanese, A.; Kim, J.-G.; Frosch, M. P.; Chung, K. Elasticizing Tissues for Reversible Shape Transformation and Accelerated Molecular Labeling. *Nat. Methods* **2020**, *17* (6), 609–613. https://doi.org/10.1038/s41592-020-0823-y.
(73) Chung, K.; Deisseroth, K. CLARITY for Mapping the Nervous System. *Nat. Methods* **2013**, *10* (6), 508–513. https://doi.org/10.1038/nmeth.2481.
(74) Yun, D. H.; Park, Y.-G.; Cho, J. H.; Kamentsky, L.; Evans, N. B.; Albanese, A.; Xie, K.; Swaney, J.; Sohn, C. H.; Tian, Y.; Zhang, Q.; Drummond, G.; Guan, W.; DiNapoli, N.; Choi, H.; Jung, H.-Y.; Ruelas, L.; Feng, G.; Chung, K. Ultrafast Immunostaining of Organ-Scale Tissues for Scalable Proteomic Phenotyping. *bioRxiv pre-print* **2019**.
(75) Zhang, N.; Li, X.; Czajkowsky, D. M.; Zhang, H.; Alam, M. S.; Shao, Z. Efficient and Fast Immuno-Labeling of Clarified Tissues Using Low-Field Enhanced Diffusion. *IEEE Trans. Biomed. Eng.* **2021**, *68* (11), 3301–3307. https://doi.org/10.1109/TBME.2021.3070146.
(76) Yun, D. H.; Park, Y.-G.; Cho, J. H.; Kamentsky, L.; Evans, N. B.; DiNapoli, N.; Xie, K.; Choi, S. W.; Albanese, A.; Tian, Y.; Sohn, C. H.; Zhang, Q.; Kim, M. E.; Swaney, J.; Guan, W.; Park, J.; Drummond, G.; Choi, H.; Ruelas, L.; Feng, G.; Chung, K. Uniform Volumetric Single-Cell Processing for Organ-Scale Molecular Phenotyping. *Nat. Biotechnol.* **2025**, 1–12. https://doi.org/10.1038/s41587-024-02533-4.

Chapter 2

Highly Multiplexed Fluorescence Microscopy with Semiconducting Polymer Dots

The following material in this chapter is reproduced with permission from:

Ziyu Guo,† Chetan Poudel,† Margaret C. Sarfatis, Jingbo Yu, Madeline Wong, Daniel T. Chiu, Joshua C. Vaughan; "Highly Multiplexed Fluorescence Microscopy with Semiconducting Polymer Dots", Science Advances, Vol. 10, no. 50, 2024.

† indicates equal contributions.

All material in this chapter has been reformatted to conform to the style of this thesis.

2.1. Abstract

Current studies of biological tissues require visualizing diverse cell types and molecular interactions, creating a growing need for versatile techniques to simultaneously probe numerous targets. Traditional multiplexed imaging is limited to around five targets at once. Emerging methods utilizing sequential rounds of staining, imaging, and signal removal can probe tens of targets but require specialized hardware, time-consuming workflows, and face some challenges with sample distortion and artifacts. Here we present a method for highly-multiplexed fluorescence microscopy using semiconducting polymer dots (Pdots) in a single round of staining and imaging. Pdots are small, bright, and photostable fluorescent probes with a wide range of tunable Stokes shifts (20–450 nm). Multiple series of Pdots with varying excitation wavelengths allow for fast (<1 minute) and single-round imaging of up to 21 targets in the brain and kidney. This method is based on a simple immunofluorescence workflow, efficient use of spectral space, standard hardware, and straightforward analysis, making it widely applicable for bioimaging laboratories.

2.2. Introduction

Biological tissues are complex networks of cells that are arranged within intricate extracellular environments and that adapt during development, aging, and disease. Fluorescence microscopy is heavily used for the study of these complex specimens and particularly benefits from the high molecular specificity of immunofluorescence and related staining methods due to their powerful ability to quantify the

distributions of multiple molecules of interest within the specimen. Commonly used fluorophores in microscopy have absorption and emission spectral bandwidths of 30–60 nm and a Stokes shift of 20–30 nm between the absorption and emission maxima. Because each fluorophore occupies a combined ~70nm of spectral bandwidth, the number of fluorophores concurrently visualized across the visible and near-infrared (400–750 nm) is commonly limited to ~5.

Prior work has sought to increase fluorescence multiplexing capabilities using various immunolabeling strategies and detection techniques[1]. One family of techniques uses sequential cycles of staining and imaging and avoids spectral overlap by chemically inactivating or removing fluorescent dyes after each cycle (e.g., MxIF[2], t-CyCIF[3], IBEX[4], and SWITCH[5]). A second family of sequential multiplexing techniques uses a single step to immunostain tissues with DNA-barcoded antibodies, followed by a sequential readout of barcodes using complementary fluorescent oligonucleotides (e.g., CODEX[6] and Immuno-SABER[7]). Multiplexed transcriptomics methods are a third family of techniques that map mRNA distributions across cells and tissues (e.g., MERFISH[8] and seqFISH[9]). These methods also use a single round of staining with barcoded probes for gene panels, followed by sequential rounds of reagent delivery and imaging to read out the barcodes and spatially localize the transcripts. Despite the large number of targets that can be probed, all of these sequential approaches encounter major limitations: extended times for probe delivery and incubation (usually 20–120 minutes or longer per cycle and on order of a day or more per experiment) that restrict the application to imaging of thin tissues; the potential for tissue distortion between rounds and for unsuccessful inactivation of probes; complex and computationally intensive probe design and analysis; and the requirement for specialized and automated fluidic handling equipment and dedicated imaging instruments.

Instead of multiple rounds of staining and imaging, a single round of highly multiplexed imaging would be desirable in many circumstances. Laser or ion beam ablation followed by mass spectroscopy can achieve higher plex imaging in a single round[10,11], but this approach involves a tedious workflow with low throughput (e.g., pump-down of the sample chamber), is destructive, and requires expensive instrumentation. A fluorescence-based technique would alleviate some of these requirements, in principle. However, commonly used microscopy fluorophores have a small Stokes shift of 20–30 nm that, together with the 30–60 nm excitation and emission bandwidths, limits the number of fluorophores that may be used. In contrast, recently developed spectrally tunable semiconducting polymer dots (Pdots)[12–23] exhibit a variable Stokes shift of 20–450 nm which can be tuned by varying the composition of the emitting Pdots[17,18,20,21]. This tunability of Stokes shift in Pdots provides much more spectral real estate for multiplexing than is possible using conventional fluorescent dyes. The related field of flow cytometry has led the way in pushing the limits of fluorescence multiplexing. However, many of the long Stokes-shift

fluorophores that made high multiplex flow cytometry possible, such as phycoerythrin (PE) tandem dyes and the BD Brilliant series of polymer dyes, can be prone to photobleaching and are thus unsuitable for imaging. In contrast, Pdots are photostable and can have similar or better photostability as water-soluble Qdots (quantum dots)[12–14,20]. (A comparison of the photostability of Pdots and BD Brilliant dyes is shown in Supplementary Figure 2.1.) Pdots are also brighter than small-molecule organic dyes or water-soluble Qdots due to their larger absorption cross-section[14,16,17,23].

Here we demonstrate highly multiplexed imaging of up to 21 targets in a single round of immunostaining and imaging by using only three series of Pdots (a Pdot series is defined by its excitation peak, such as a 355 nm excitable series of Pdots comprising over 10 Pdots - each with a distinct emission peak from below 400 nm to over 800 nm). With computational processing using linear unmixing[24] after a single round of image acquisition, overlapping spectral signals of multiple Pdots can be unmixed and reassigned to their corresponding channels to provide reliable signal separation and distinct multi-target imaging. We demonstrate the versatility of our technique by using both direct and indirect immunolabeling of tissues (mouse kidney and brain), and by making both separate and concurrent use of excitation- and emission-multiplexed imaging.

2.3. Results

2.3.1. Semiconducting Pdots with Spectrally Tunable Properties

Pdots are semiconducting nanoparticles prepared by collapsing hydrophobic semiconducting polymers into a compact "dot", the size of which can be tuned from ~5 nm to over ~20 nm[12,13,15,18,19]. The brightness of Pdots is generally very high, owing to their large absorption cross-section. In fact, by incorporating a Qdot into a Pdot, the brightness of the Qdot can be increased by up to an order of magnitude in comparison with a water-soluble Qdot alone[16]. The photophysical property of Pdots that is of particular relevance to the current study is amplified energy transfer, which enables the Stokes shift to be tuned from ~20 nm to over 400 nm[20,21]. This characteristic, together with narrow emission bands, allows for the design and creation of a large color panel (e.g., 10) for a single wavelength excitation. Unlike Qdots, the absorption peak of Pdots can also be tuned to enable excitation multiplexing. Combining excitation and emission multiplexing enables the creation of a very large color panel that numbers in the many tens. These favorable properties of Pdots have now facilitated highly multiplexed flow-cytometry analysis of single cells, and Pdots are commercially available as the StarBright series from Bio-Rad, with over 30 colors launched thus far. Unlike many of the tandem dyes used traditionally in flow cytometry, most Pdots possess good photostability and may enable highly multiplexed fluorescence imaging. Additionally, Pdots can be designed with further improved photostability or used under conditions that improve their photostability[22].

For multiplexed imaging in this study, we used three series of spectrally distinguishable Pdots with absorption maxima near 355 nm, 405 nm, or 488 nm for optimal excitation with commonly available laser lines. For each series, we used 6–8 Pdots with a range of emissions covering the visible and near-infrared spectrum, from below 400 to over 800 nm. The excitation and emission spectra of this palette of 22 Pdots are shown in **Figure 2.1**.

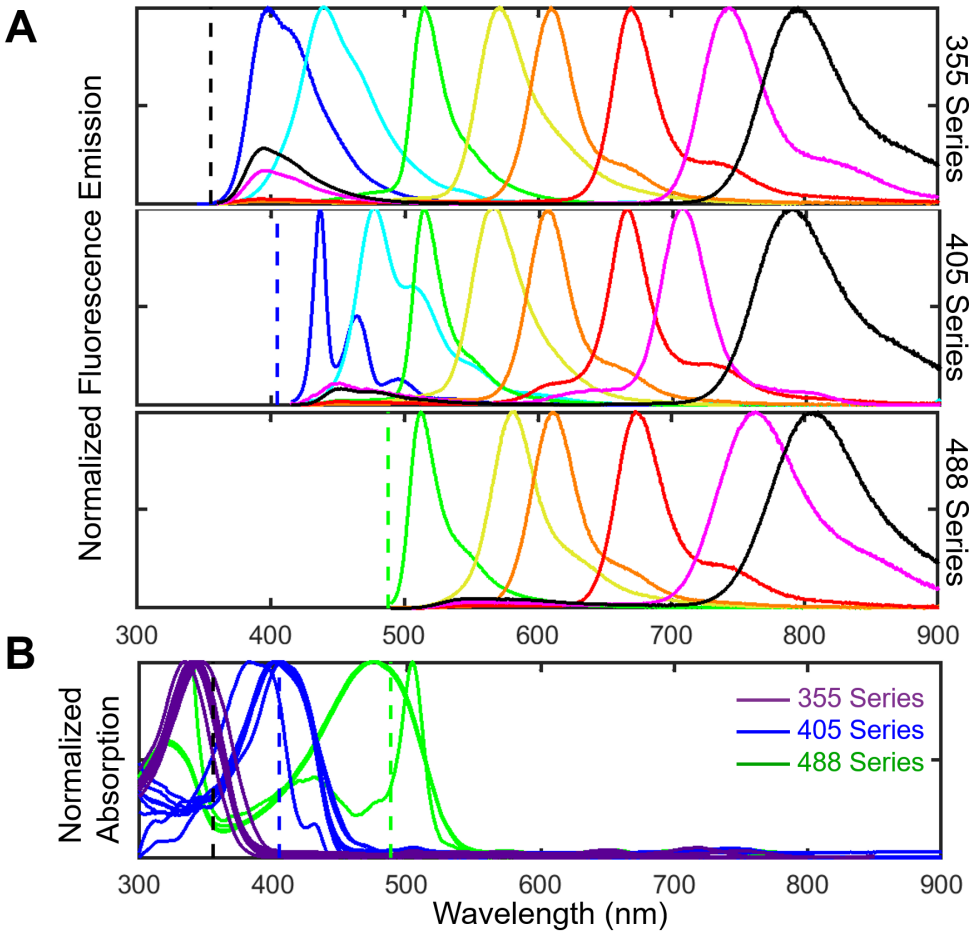

Figure 2.1. Emission (A) and excitation (B) spectra of three series of Pdots. *Each series contains 6–8 Pdots with emission wavelengths that span the visible and near-infrared spectrum from below 400 to over 800 nm. Dashed lines indicate the excitation wavelengths used (365, 405, and 488 nm).*

In order to measure fluorescence from about 400 to 800 nm for our panels of Pdots, we sequentially recorded images using a set of bandpass emission filters (**Supplementary Figure 2.7.2**) for a given excitation wavelength, then repeated the process for up to three excitation wavelengths. While the emission filters were selected to match each Pdot, some emission bleedthrough was present due to spectral overlap of the Pdots within each Pdot series (**Figure 2.1A**). This emission bleedthrough is most notable for Pdots in adjacent spectral bands and for Pdots with a principal emission peak of 700–800 nm that exhibit a minor

emission peak with a small Stokes shift of 50–100 nm. In addition, the excitation spectra of the three Pdot series partly overlap at the excitation wavelengths, leading to some cross-excitation (**Figure 2.1B**). For instance, at 365 nm excitation, 355ex-Pdots (the 355 nm excitation series of Pdots) are excited at ~80% of their excitation maximum while the 405ex-Pdots and 488ex-Pdots are also cross-excited at ~20–30% of their excitation maximum. To address emission-bleedthrough and cross-excitation, we employed a linear unmixing algorithm in MATLAB (source code publicly available: see Data and materials availability) to reassign signals to their corresponding channels based on calibration data measured for individual Pdots. This procedure allowed us to generate unmixed images that correct for crosstalk.

2.3.2. Emission multiplexing: Visualizing eight targets using a single excitation wavelength in a single round

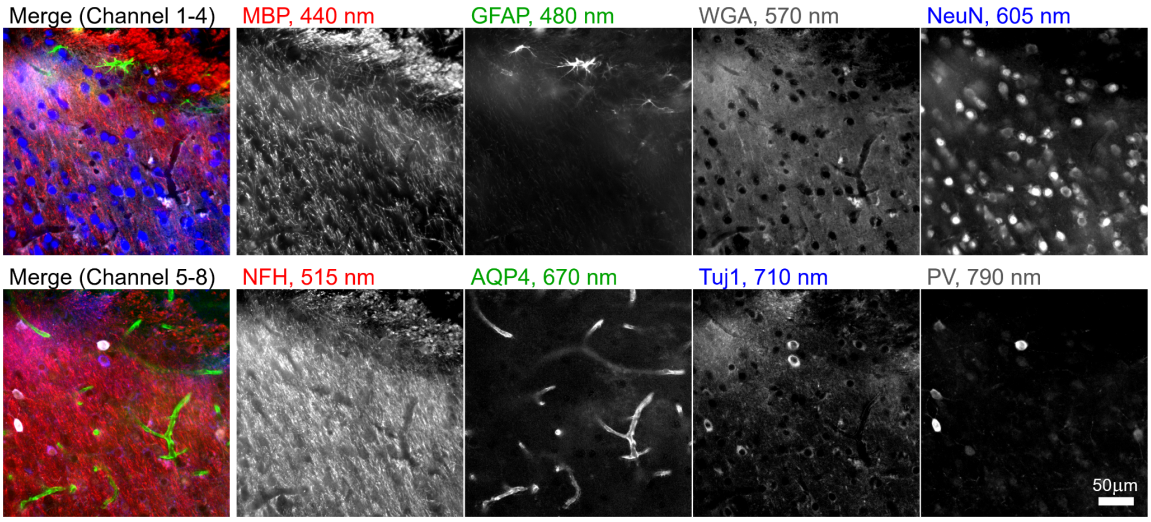

Figure 2.2. Emission multiplexing with the 405ex-Pdot series. *A 100 µm thick brain section was stained with eight different Pdots conjugated to a set of seven secondary antibodies and the lectin wheat germ agglutinin. The specimen was imaged at the amygdalar and piriform area by illuminating with 405 nm light on a widefield microscope. The signal measured through different bandpass filters was linearly unmixed. (MBP = myelin basic protein, GFAP = glial fibrillary acidic protein, WGA = wheat germ agglutinin, NeuN = neuronal nuclei, NFH = neurofilament H, AQP4 = aquaporin-4, Tuj1 = tubulin beta III, PV = parvalbumin.)*

To concurrently label and visualize eight key structures in mouse brain using emission multiplexing with Pdots excited at 405 nm, we first selected and validated seven primary antibodies and the lectin wheat germ agglutinin (WGA) with distinct staining patterns in mouse brain. The panel of seven primary antibodies was selected to also be antigenically distinct (i.e., mouse IgG1, mouse IgG2a, mouse IgG2b, mouse IgG3, rabbit, rat, and chicken) so that they could each be uniquely targeted by specific secondary antibodies (i.e.,

goat anti-mouse IgG1, goat anti-mouse IgG2a, goat anti-mouse IgG2b, goat anti-mouse IgG3, donkey anti-rabbit, donkey anti-rat, and donkey anti-chicken; see **Supplementary Table 2.7.1** for details). Next, eight Pdots from the 405 nm series with emission peaks ranging from 430 nm to 800 nm were conjugated to secondary antibodies or directly to WGA. **Figure 2.2** shows a 100 μm thick brain tissue section stained for eight targets using these probes and then imaged within a few seconds in a single round of automated imaging using matched filter sets. The images displayed in **Figure 2.2** were linearly unmixed from raw data to correctly reassign bleedthrough from each spectral band to the corresponding stain; see the Methods, **Supplementary Text** and **Supplementary Figure 2.7.3** for details on the linear unmixing procedure and for a comparison of the raw and unmixed images. The secondary antibody-Pdot conjugates bind to primary antibodies accurately with a low background signal. Anti-MBP labeled oligodendrocytes, anti-GFAP labeled astrocytes/glial cells, WGA labeled N-Acetylglucosamine, anti-NeuN labeled neuronal nuclei, anti-NFH labeled heavy neurofilaments, anti-AQP4 labeled aquaporin-4 water channel protein, and anti-Tuj1 labeled beta-tubulin III on neural stem cells.

In a related experiment for 8-channel emission multiplexing with the 405 nm Pdot series, we used a set of five secondary antibody-Pdot conjugates (anti-mouse IgG1, anti-mouse IgG2a, anti-mouse IgG2b, anti-rabbit, anti-rat), a direct antibody-Pdot conjugate, and two Pdot-lectin conjugates, to label and image a mouse kidney tissue section (**Supplementary Figure 2.7.4**). We also performed 7-channel emission multiplexing with the 355ex-Pdot series in mouse brain and mouse kidney using a mixture of Pdot-secondary antibody conjugates, Pdot-primary conjugates, and Pdot-lectin conjugates (**Supplementary Figure 2.7.5 and 2.7.6**). Together, this collection of experiments demonstrates the feasibility of using emission multiplexing with Pdots to achieve up to 8-channel imaging with a single excitation wavelength.

2.3.3. Excitation multiplexing: Visualizing three targets using a single emission filter in a single round

In addition to emission multiplexing, in which one excitation wavelength excites a set of Pdots that fluoresce across a range of emission wavelengths, Pdots can also be used for excitation multiplexing, in which Pdots that emit at the same wavelength are selectively excited using different illumination wavelengths. For example, in **Figure 2.3**, we demonstrate three-channel excitation-multiplexed imaging of mouse brain tissue using Pdots that emit at 670 nm and of mouse kidney tissue using Pdots that emit at 800 nm. In each case, the Pdots are selectively excited via illumination at 365 nm, 405 nm, and 488 nm. Unlike emission multiplexing, in which bleedthrough into neighboring emission channels is observed, here we encounter some cross-excitation of Pdots that produces channel crosstalk (e.g., 405 nm illumination undesirably cross-excites the 488ex-Pdots ~20%, see **Figure 2.1B**). We corrected this cross-excitation in a similar fashion as before using linear unmixing (see **Supplementary Figure 2.7.7** for a comparison of the

raw and unmixed data). This ability to perform excitation multiplexing is unavailable to Qdots because they do not have distinct absorption peaks.

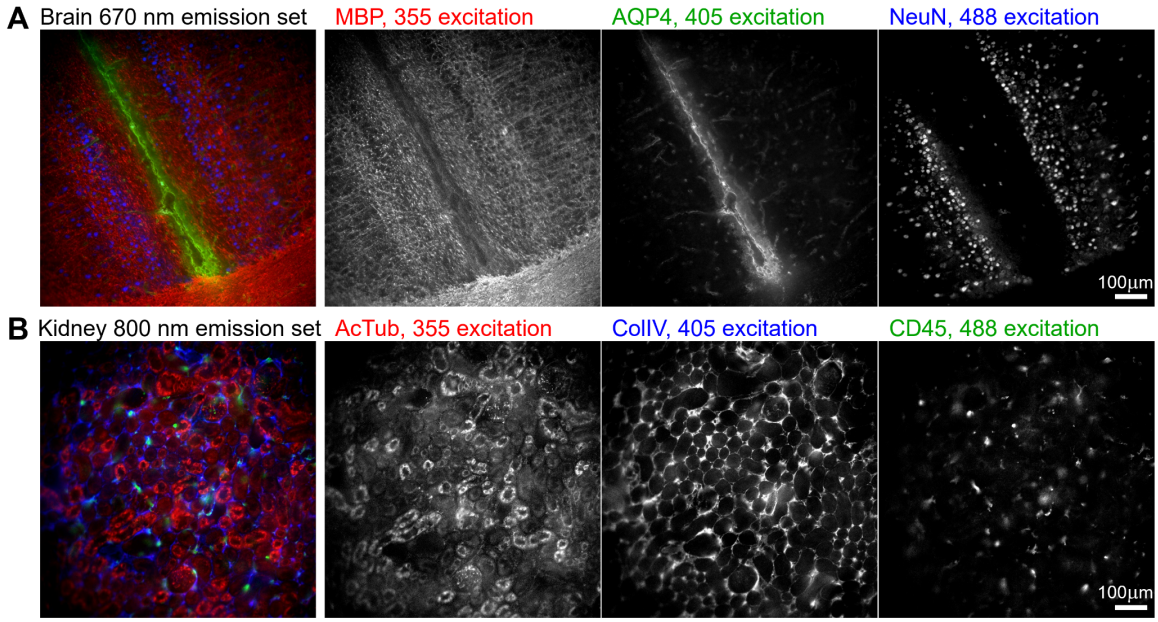

Figure 2.3. Excitation multiplexing. *Three-channel excitation-multiplexed imaging of 100 µm thick tissue sections of (A) mouse brain, imaged above the medial corpus callosum region, and (B) mouse kidney, imaged at the cortex region. Each set of three Pdots was illuminated at 365 nm, 405 nm, and 488 nm; a 667/30 nm emission filter was used for the brain, and a 800/60 nm emission filter for the kidney. (MBP = myelin basic protein, AQP4 = aquaporin-4, NeuN = neuronal nuclei, AcTub = acetylated tubulin, ColIV = collagen 4, CD45 = leukocyte common antigen.)*

2.3.4. Excitation and emission multiplexing: up to 21-plex imaging in a single round

Having separately demonstrated the possibilities of using Pdots for excitation- and emission-multiplexed imaging, we sought to combine them using our three series of Pdots to stain and visualize up to 21 targets in a single round. Using indirect immunofluorescence to stain a large number of targets in a single round is impractical due to limitations in the number of independent primary/secondary antibody combinations. Therefore, when creating larger palettes of probes, we chose to conjugate the Pdots directly to primary antibodies or lectins (see **Supplementary Table 2.7.3**). We validated independent antibodies or lectins as labeling their respective targets of interest, conjugated each antibody or lectin to a Pdot, revalidated the binding of antibody-Pdot conjugates to the original targets, and performed careful crosstalk calibration measurements for each Pdot. Using this procedure, we were able to perform 14-plex imaging of a mouse brain section and 21-plex imaging of a mouse kidney section, with the data acquisition for each being performed in under a minute (**Figure 2.4–2.5**). As before, details of filters, antibodies, and Pdot

conjugations are listed in **Supplementary Table 2.7.1–2.7.3**, and the linear unmixing procedure is described in the methods section.

We also investigated the compatibility of our workflow with formalin-fixed paraffin-embedded (FFPE) tissues in addition to the fresh fixed tissues shown above. This labeling was performed without any modifications to our brain and kidney panels of pre-conjugated Pdots and without any optimization of concentrations, crosstalk, or antigen retrieval. We chose 10 Pdot conjugated antibodies or lectins against targets that show broad expression in many organs and we successfully stained and visualized targets in 7-9 channels each in the brain, kidney, thymus, prostate, and larynx (**Supplementary Figure 2.7.8-2.7.12**). As before, these images were obtained using just 3 excitation wavelengths. In 1-3 channels per organ, we did not see a positive signal as the antibody targets were either not expressed (e.g., NeuN is only present in the brain) or in low abundance in those organs.

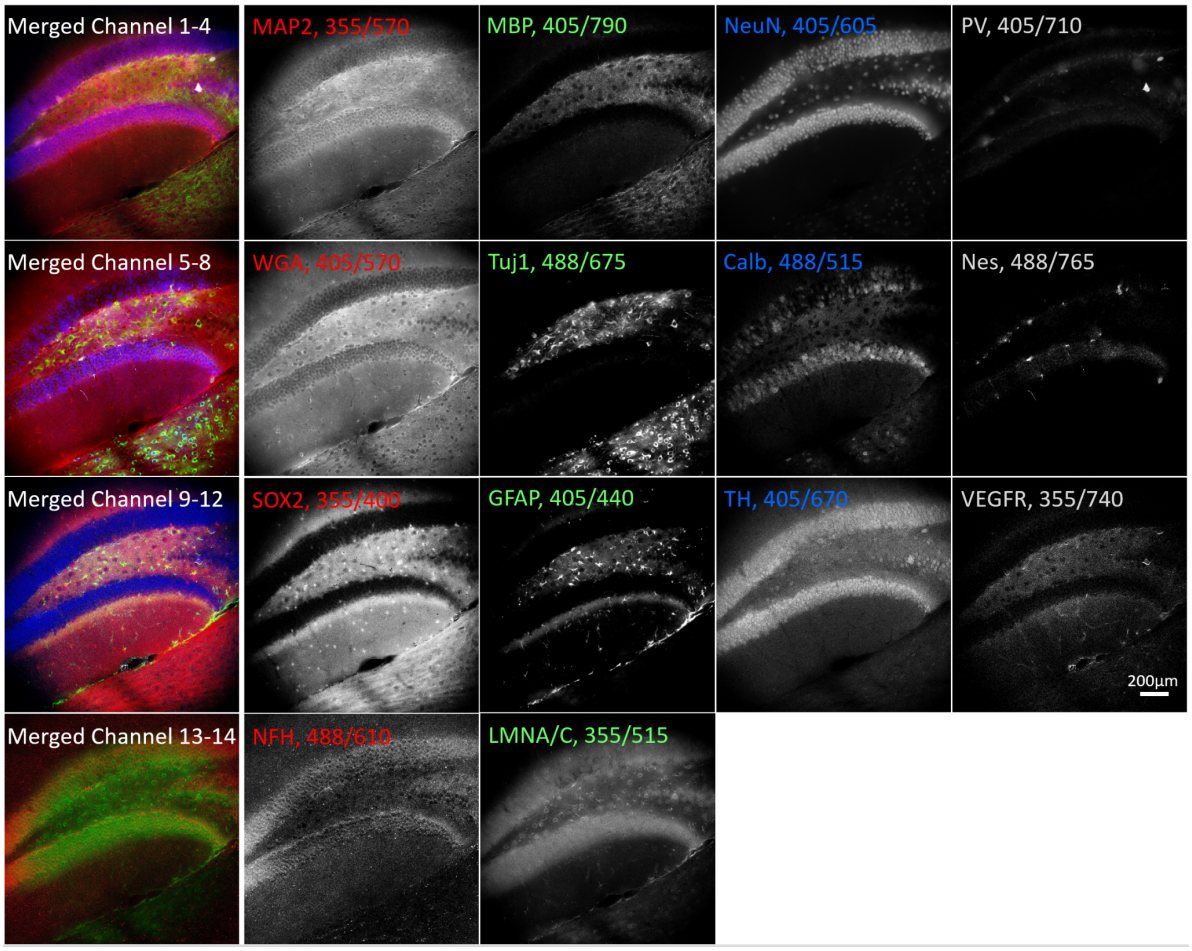

Figure 2.4. Excitation and emission multiplexing in brain tissue. *A 50 μm thick mouse brain section showing the dentate gyrus of the hippocampus stained with 14 Pdots conjugated to primary antibodies and lectins. The tissue was imaged using a combination of three excitation wavelengths and eleven emission filters. The left column shows four partial 4-channel composite images; the four columns to the right show corresponding grayscale images. Labels indicate the protein target or lectin (WGA) together with Pdot excitation/emission wavelengths. (MAP2 = microtubule associated protein 2, MBP = myelin basic protein, NeuN = neuronal nuclei, PV = parvalbumin, WGA = wheat germ agglutinin, Tuj1 = tubulin beta III, Calb = calbindin, Nes = neuroepithelial stem cell protein, SOX2 = sex determining region Y-box 2, GFAP = glial fibrillary acidic protein, TH = tyrosine hydroxylase, VEGFR = vascular endothelial growth factor receptor 3, NFH = neurofilament H, LMNA/C = lamin A/C.)*

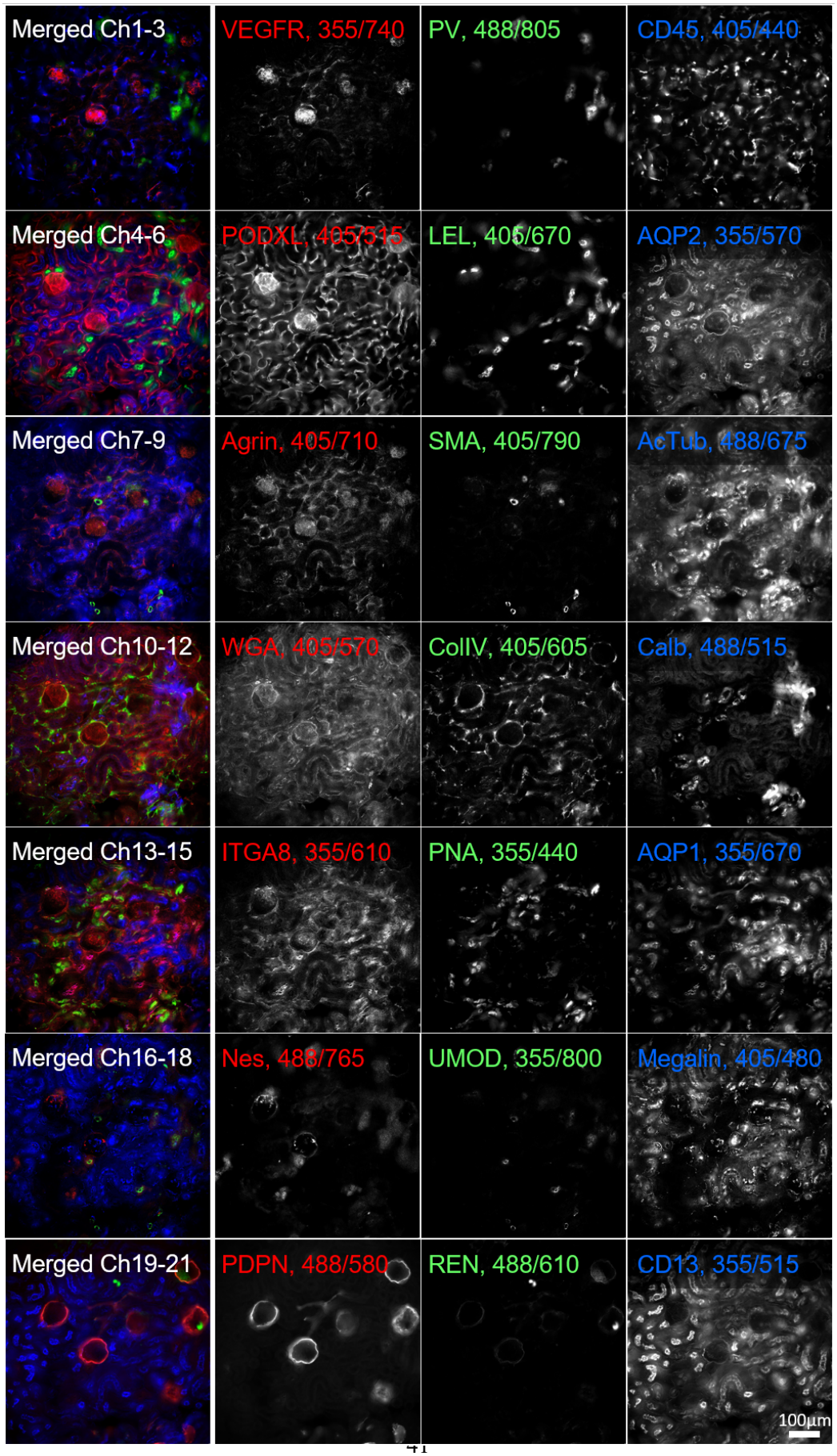
Merged Ch1-3
VEGFR, 355/740
PV, 488/805
CD45, 405/440
Merged Ch4-6
PODXL, 405/515
LEL, 405/670
AQP2, 355/570
Merged Ch7-9
Agrin, 405/710
SMA, 405/790
AcTub, 488/675
Merged Ch10-12
WGA, 405/570
ColIV, 405/605
Calb, 488/515
Merged Ch13-15
ITGA8, 355/610
PNA, 355/440
AQP1, 355/670
Merged Ch16-18
Nes, 488/765
UMOD, 355/800
Megalin, 405/480
Merged Ch19-21
PDPN, 488/580
REN, 488/610
CD13, 355/515
100µm

Figure 2.5. Excitation and emission multiplexing in kidney tissue. *A 50 µm thick mouse kidney section stained with 21 Pdots conjugated to primary antibodies and lectins. The tissue was imaged at the cortex region using a combination of three excitation wavelengths and eleven emission filters. The left column shows seven 3-channel composite images of the same tissue region; the three columns to the right show corresponding grayscale images. Labels indicate the protein targets or lectins (LEL, WGA, PNA) together with Pdot excitation/emission wavelengths. (VEGFR = vascular endothelial growth factor receptor 3, PV = parvalbumin, CD45 = leukocyte common antigen, PODXL = podocalyxin, LEL = lycopersicon esculentum tomato lectin, AQP2 = aquaporin 2, SMA = alpha-smooth muscle actin, AcTub = acetylated tubulin, WGA = wheat germ agglutinin, ColIV = collagen 4, Calb = calbindin, ITGA8 = integrin alpha 8, PNA = peanut agglutinin, AQP1 = aquaporin 1, Nes = neuroepithelial stem cell protein, UMOD = uromodulin, Megalin = low density lipoprotein-related protein 2, PDPN = podoplanin, REN = renin, CD13 = Aminopeptidase N.)*

2.4. Discussion

Multiplexed imaging is increasingly important to probe the interactions of various cell types in disease and in the context of discovery efforts such as tissue atlases. Our technique provides broad applicability since Pdots can be bound to commercially available conventional antibodies, which offers flexibility in the choice of cellular markers, antibody-Pdot combinations, etc. Compared to iterative staining methods [2–7], our method is simpler and faster, and does not require probe inactivation reagents or suffer from tissue distortion. We make use of standard imaging hardware available in most bioimaging labs, unlike other multiplexing approaches that use more sophisticated hardware or may need dedicated instruments for automated fluidics or multi-day acquisitions [6–11,25]. We have demonstrated that in a single round of highly multiplexed imaging, we can concurrently investigate up to 21 targets in a single 50 µm thick tissue specimen using three series of Pdots with excitation at 365 nm, 405 nm, and 488 nm. Additional 560 nm and 647 nm series of Pdots would enable excitation multiplexing [26] to a larger extent than we demonstrated here, and the number of targets could be increased further to ~30 in a single round through a combination of excitation and emission multiplexing with 5 series of Pdots. Combining this approach with antibody stripping or Pdot inactivation (e.g. via quenching or bleaching) may make it possible to measure over 100 targets in only 4–5 rounds of imaging.

In contrast to the above benefits, the use of Pdots for highly multiplexed imaging does face some challenges. The process of conjugating antibodies to Pdots places some restrictions on the choice of antibodies and requires careful pre- and post-validation of antibody performance. For this study, we tested 54 Pdot-primary antibody (or Pdot-lectin) conjugates (**Supplementary Table 2.7.3**). Of these 54 conjugates, 31 consistently

produced strong staining of the correct molecular targets, 10 produced weak staining, and 13 showed no staining or unsuitably high background indicative of non-specific binding (see **Supplementary Figure 2.7.13** for the process of validation of Pdot-antibody conjugates). These results show an estimated ~60% success rate for Pdot conjugation. The failure rate of Pdot-primary antibody conjugates (~40% not binding their targets efficiently) is similar to that of DNA-conjugated primary antibodies and other approaches involving custom primary conjugates to conventional dyes [3]. Purchasing different primary antibodies against the same target and repeating the conjugation often led to identifying a successful conjugate.

As part of our image processing workflow, we used linear unmixing - a simple and popular technique in the field of multiplexed imaging which uses raw/mixed image data and a reference/calibration matrix to generate unmixed spectral images [24,27]. Despite the technique's simplicity, it requires a pre-measurement of all the Pdots individually in each imaging channel before the unmixing can be performed. However, this calibration can be performed once for all subsequent experiments where the same imaging settings are used. Techniques like hyper-spectral phasors (HySP) and blind source separation methods can unmix signals without prior measurements of reference spectra but generally perform worse when there are larger numbers of mixed channels [28–31]. For instance, PICASSO [31] uses a sophisticated unmixing algorithm that seeks to maximize the differences between multiple channels but has some potential limitations in cases where channels may be innately similar to one another. In another approach, Lin *et al.* used a customized microscope with a 7-laser system and a continuously tunable emission filter together with variable Stokes shift fluorescent probes to achieve up to 19-channel immunofluorescence [25].

We also noticed higher levels of background when illuminating the 355 nm series of Pdots; at these shorter excitation wavelengths, biological tissues exhibit strong autofluorescence that can mask the specific staining or impact the unmixing calculation, generating images with autofluorescence contamination in the short wavelength channels. The use of thinner tissue sections or incorporating corrections for autofluorescence may improve the multiplexing performance of these Pdots. While most Pdots are bright and photostable, we noticed that some Pdots with larger Stokes shifts exhibit blue-shifting of their spectrum in a power density dependent manner when exposed to bright focused light (e.g., when using a confocal microscope with a high-NA objective lens). This spectral shift can introduce errors during linear unmixing, as signals tend to be weaker for Pdots with larger Stokes shift (i.e., redder emission channels). This may limit the current applications of Pdot multiplexing to microscopies that use lower power densities, such as widefield and lightsheet microscopy. In the future, engineering Pdots that do not exhibit spectral shifts would make them more broadly applicable and better suited to microscopy modes that involve very high excitation power densities.

With the availability of additional sets of Pdots excitable at 561 nm and 640 nm, together with increasing emission multiplexing and better compensation methods, it will be possible to further increase the number of targets that can be studied in a single round of staining and imaging. While fewer emission bands can be accommodated for these redder excitation wavelengths, incorporating these additional Pdot series could allow for probing ~30 targets in a single round. We are also investigating approaches to engineer these Pdots to have narrower excitation and emission bands to reduce bleedthrough and cross-excitation, which will further increase the number of targets that can be probed in a single round of imaging.

2.5. Materials and Methods

2.5.1. Experimental Design

This study aims to develop an approach to highly-multiplexed fluorescence microscopy with a simple workflow and wide applicability in bioimaging laboratories with standard imaging hardware. The experimental design is based on the use of fluorescent semiconducting nanoparticles (Pdots) that have a large range of Stokes shifts and are spectrally distinct from each other, thus enabling combinations of excitation and emission multiplexing. Pdots are conjugated to commercially available antibodies of interest. By designing all experiments to be conducted in a single round of staining and imaging, our approach emphasizes simplicity, speed, and applicability to routine microscopy procedures.

2.5.2. Absorption and emission spectra

Semiconducting Pdots were diluted 1:100 in PBS-azide (phosphate buffered saline containing 3 mM sodium azide) and measured using a PerkinElmer LS55 fluorometer. Three excitation wavelengths—355 nm, 405 nm, and 488 nm—were used to generate emission by the corresponding Pdot series.

2.5.3. Mouse brain and kidney sample preparation

All procedures used in this study were approved by the University of Washington Institutional Animal Care and Use Committee under protocol number 4442-01. Three mice were used in this study: Mouse 1, a 6-month-old C57BL/6 Cre-ERT2 female; Mouse 2, a 2-month-old C57BL/6 wildtype female; and Mouse 3, a 5.5-month-old B6*P14 transgenic female. Tissues from these mice did not exhibit any fluorescent reporters. Immediately after CO_2 euthanasia, mice were cardiac-perfused with PBS-azide and 4% paraformaldehyde (PFA), each for 5 min. The kidneys, with renal capsule removed, were harvested and fixed in 10 mL of 4% PFA for 1 h. The brain was fixed overnight in PFA. After fixation, the brain was embedded in agarose gel and sliced into 50 μm and 100 μm thick sections on a vibratome along the coronal

plane. The kidneys were sliced without embedding into 50 µm and 100 µm sections along the coronal plane. All sections were stored in PBS-azide at 4 ºC until further use.

2.5.4. Screening and validation of antibodies

The full list of primary and secondary antibodies used in this study is provided in **Supplementary Table 2.7.2–2.7.3**. We validated the performance of primary antibodies by staining tissues with the primary antibody and then a pre-validated secondary antibody conjugated to conventional fluorescent dyes (such as ATTO 488, Alexa Fluor 568, or ATTO 647N). We confirmed that the antibodies bound the correct targets in desired tissues by comparing our images with the literature. Secondary antibodies were validated in a similar manner but in combination with a pre-validated primary antibody. After this first round of validation, the antibodies (primary or secondary) were conjugated to Pdots. In some cases, the conjugation could change the antibody's structure, antigenicity, or binding efficiency. We therefore re-validated each antibody after conjugation to Pdots to confirm target binding via imaging. The process of conjugating antibodies to Pdots places some restrictions on the choice of antibodies. Some components typically found in the antibody buffer solution, such as bovine serum albumin, gelatin, albumin, and Tris buffer, can interfere with the conjugation reaction and make the yield harder to quantify. We chose to use antibodies without these components, which sometimes limited us to using antibodies that were not used widely in other papers.

2.5.5. Conjugation of antibodies to Pdots

The preparation of Pdot-conjugates has been described in detail in prior publications[12-14, 17, 21]. Briefly, Pdots were conjugated to antibodies or lectin via a 1-ethyl-3-(-3-dimethylaminopropyl) carbodiimide hydrochloride (EDC) catalyzed reaction, in which 0.25 mL of Pdot solution was mixed with 3 uL of EDC and 60 uL of an antibody solution, and reacted for 3 h. The final solution was then loaded onto a gel filtration column to purify the Pdot-antibodies from free unreacted antibodies.

2.5.6. Immunostaining

Tissues were incubated in block/permeabilization solution (3% bovine serum albumin and 0.5% Triton-X 100) for at least 4 h at room temperature (~23 °C) on a shaker. All tissues were stained in a single round. For indirect immunofluorescence, tissues were stained overnight with primary antibody and overnight with Pdot-conjugated secondary antibody. For direct immunofluorescence, tissues were stained for 24 h. Tissues were washed with PBS-azide 3 times for 10 min each and were imaged in a single round with the proper filter combinations (**Supplementary Table 2.7.1**). Luminescence tends to be dimmer for Pdots with larger Stokes shifts and the quantum efficiency of standard sCMOS cameras also declines towards the near-

infrared region. To counter these issues, we paired the brightest immunostains with the dimmest Pdots and increased the concentration of the dimmest stains to achieve similar levels of signal intensity for each channel.

2.5.7. Immunostaining of FFPE Tissue Microarray:

FFPE tissue microarray slides containing multiple organ sections of 5 μm thickness were purchased from TissueArray.com (MON621 : from C57BL/6N mouse). The slides were baked at 60°C for 2 hours. Tissues were deparaffinized by incubation in 100% Histo-Clear (Electron Microscopy Sciences**)** for 30 minutes, followed by 50% Histo-Clear: 50% ethanol for 5 minutes. Tissues were rehydrated by incubating in serial dilutions of ethanol in MilliQ water: 100%, 90%, 80%, 70%, 60%, 50% ethanol for 5 minutes each, then finally in MilliQ water for 10 minutes. Antigen retrieval was performed with a sodium citrate buffer (10mM Sodium Citrate, 0.05% Tween 20, pH 6.0), which was heated in the microwave for 35 seconds at high power. Slides were then inserted in the hot buffer, microwaved at low power for 2-3 minutes, cooled at room temperature (~23 °C) for 50 minutes, and washed with PBS for 10 minutes before storing in PBS. The slides were then placed in a 50 mL conical tube with block/permeabilization solution at room temperature for 2 hours on a shaker. A PAP pen was used to form a hydrophobic layer around the tissues. Tissues were stained with 10 Pdot-primary antibody conjugates in a single round of overnight staining in 250 microliters of block/perm solution. Staining was performed in a humidity chamber in the dark and tissues were washed with PBS a few times the next day before imaging.

2.5.8. Imaging

All Pdot imaging was performed on a Nikon widefield microscope equipped with a motorized objective z-drive for focusing (Ti2-E, Nikon Instruments Inc.), automated XY stage (MS2000, Applied Scientific Instrumentation), motorized filter cube turrets, an assembly of motorized filter wheels (FW102C, Thorlabs), and a scientific CMOS camera (Orca Flash 4.0v3, Hamamatsu). All parts were controlled using open-source Micromanager software (v2.0). Excitation was achieved by filtering the white light output of a SOLA U-nIR light engine (Lumencor) using three excitation filters. Emission filters were optimized to capture a band of 20–60 nm at the emission peaks of each Pdot.

For a few validation experiments, another Nikon widefield scope (Ti-S, Nikon Instruments Inc.) with 4-channel LED illumination (Thorlabs DC4104), quad-band dichroic, emission filters, and an Andor Zyla 5.5 scientific CMOS camera (Andor) was used. All dichroic, excitation, and emission filters are listed in **Supplementary Table 2.7.1** and were purchased from Semrock or Chroma.

2.5.9. Linear unmixing

Mixed signals due to spectral overlap in each channel were computationally unmixed using a custom analysis script in MATLAB (v2024a). The emission profiles of each conjugated Pdot in solution were measured across the available emission filter channels to record the proportion of crosstalk and signal bleedthrough to neighboring channels. During initial stages of the project when excitation and emission multiplexing were performed separately, we used a simpler calibration procedure for just the few necessary channels. As more Pdots were conjugated and the full palette of 22 distinct Pdots was available, we performed a full calibration for each pure Pdot in solution (i.e., using each combination of illumination wavelength and emission channel for each Pdot) to produce a 22 × 22 calibration matrix. The inverse of the complex conjugate of this calibration matrix was multiplied to the raw mixed datasets to generate unmixed datasets using non-negative least squares fitting on a pixel-by-pixel basis.

2.5.10. Statistical Analysis

Image data was processed using established software tools (e.g., ImageJ and MATLAB 2024a). Quantitative measurements, such as signal intensities, were extracted from regions of interest. Example raw data, including images and measurement values, are available in the supplementary material and also archived in Zenodo.

2.6. Acknowledgments

We gratefully acknowledge assistance from Dr. Chenyi Mao in the initial stages of this project. This work was supported by funding from the University of Washington (J.C.V. and D.T.C.), National Institutes of Health grant R01MH115767 (D.T.C and J.C.V.), NIDDK Diabetic Complications Consortium grants DK076169 and DK115255 (J.C.V.), and Washington Research Foundation Postdoctoral Fellowship (C.P.).

All relevant data needed to evaluate the conclusions in the paper are present in the paper and/or the Supplementary Materials. Two example datasets and the MATLAB source code used for linear unmixing of mixed signals have been deposited on Github (https://github.com/chetan-poudel/Pdot-linearunmixing) and archived in Zenodo (https://doi.org/10.5281/zenodo.11100240)

2.7. Supporting Information

Supplementary Text on linear unmixing:

Mixed signals in spectral multiplexing experiments arise when two or more signals are detected within a single channel as a result of spectral crosstalk. In linear algebra terms, this can be written as equation (S2.1) where the mixed signals are a matrix multiplication between the crosstalk / calibration matrix and the "unmixed" or true signal.

$$Mixed = CM \times Unmixed \qquad \text{(S2.1)}$$

Using linear unmixing, the "unmixed" images can be calculated using equation (S2.2) when the "mixed" images and the "calibration matrix" are known. It is a simple matrix multiplication between the inverse calibration matrix and the mixed images.

$$Unmixed = CM^{-1} \times Mixed \qquad \text{(S2.2)}$$

As an example, let us take the context of emission multiplexing as shown in **Figure 2.2** or **Supplementary Figure 2.7.3**. According to equation (S2.2), an 8-channel unmixed image [8×1 dimensions] can be generated by the matrix multiplication of the inverse calibration matrix [CM^{-1}, 8×8 dimensions] with the 8-channel mixed image [8×1 dimensions].

For the average signal in the images in **Supplementary Figure 2.7.3**, equation (S2.1) looks like the following in visual and in tabular form:

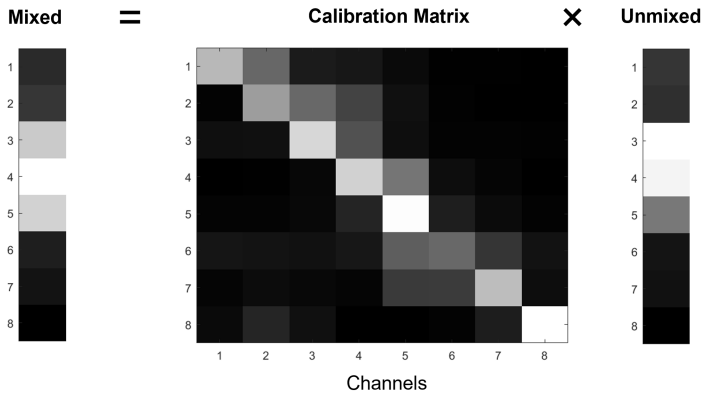

Mixed	=	Normalized Calibration Matrix (row sum = 1)								×	Unmixed
4128.692		0.523	0.292	0.079	0.068	0.030	0.005	0.003	0.000		5067.87
5115.112		0.010	0.447	0.296	0.191	0.047	0.006	0.002	0.000		4506.26
17253.86		0.043	0.046	0.610	0.232	0.041	0.011	0.009	0.008		23836.98
21666.55		0.000	0.003	0.020	0.592	0.331	0.038	0.015	0.001		22789.82
17940.11		0.014	0.014	0.024	0.103	0.717	0.086	0.032	0.011		11272.82
3134.799		0.061	0.055	0.049	0.067	0.267	0.297	0.153	0.051		2015.379
2303.913		0.015	0.037	0.023	0.017	0.166	0.168	0.536	0.037		1737.986
673.6892		0.030	0.106	0.045	0.000	0.000	0.011	0.082	0.724		121.7523

According to the calibration matrix, 52.3% of the total signal of the first Pdot lands in its own channel, 29.2% of the signal lands in the next channel, and so on. Note that the unmixed signal intensities have changed in subtle ways in comparison to the mixed signals. These changes are much more obvious when unmixing one or two pure stains in solution. We tested our method on solutions of pure stains and simple combinations of pure stains and we were able to unmix the signals with >99% accuracy: less than 1% of the signal was misassigned. Our actual unmixing software routine, which is provided on GitHub and Zenodo together with sample data (see main text, Data and materials availability), uses a small variation on the above procedure that ensures the returned unmixed signals lack negative components which would be unphysical.

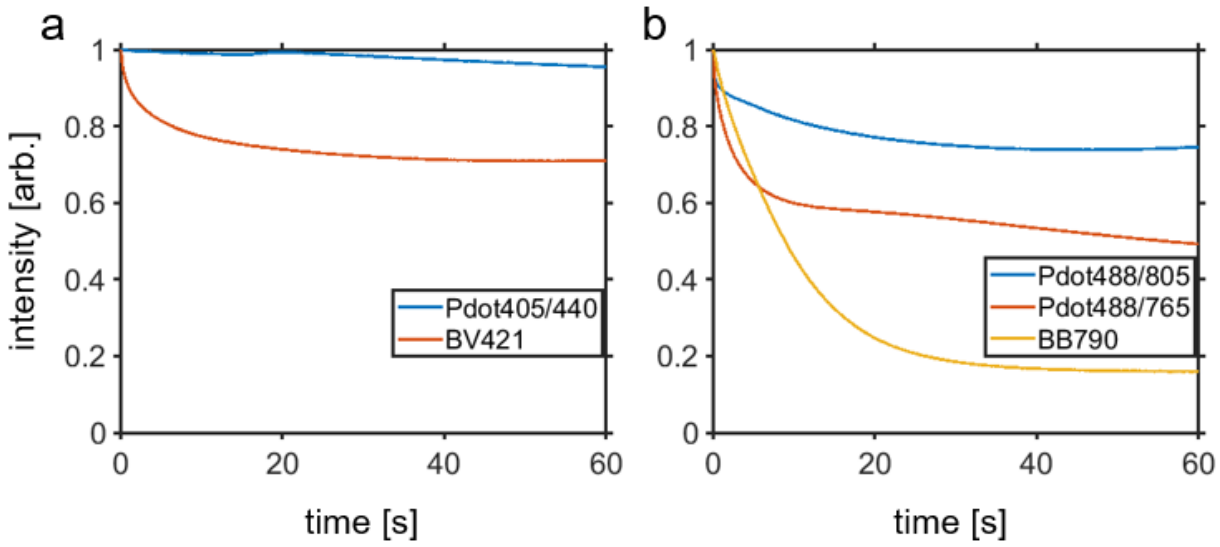

Supplementary Figure 2.7.1. Comparing the photostability of Pdots against other dyes commonly used in flow cytometry. *(a) Comparison of the photostability of Pdot405/440 and Brilliant Violet 421, both excited at 405 nm (N=1). (b) Comparison of the photostability of the long Stokes-shift probes Pdot488/765, Pdot488/805, and BB790, all excited at 488 nm (N=1). All probes were illuminated at intensities comparable to that used for imaging.*

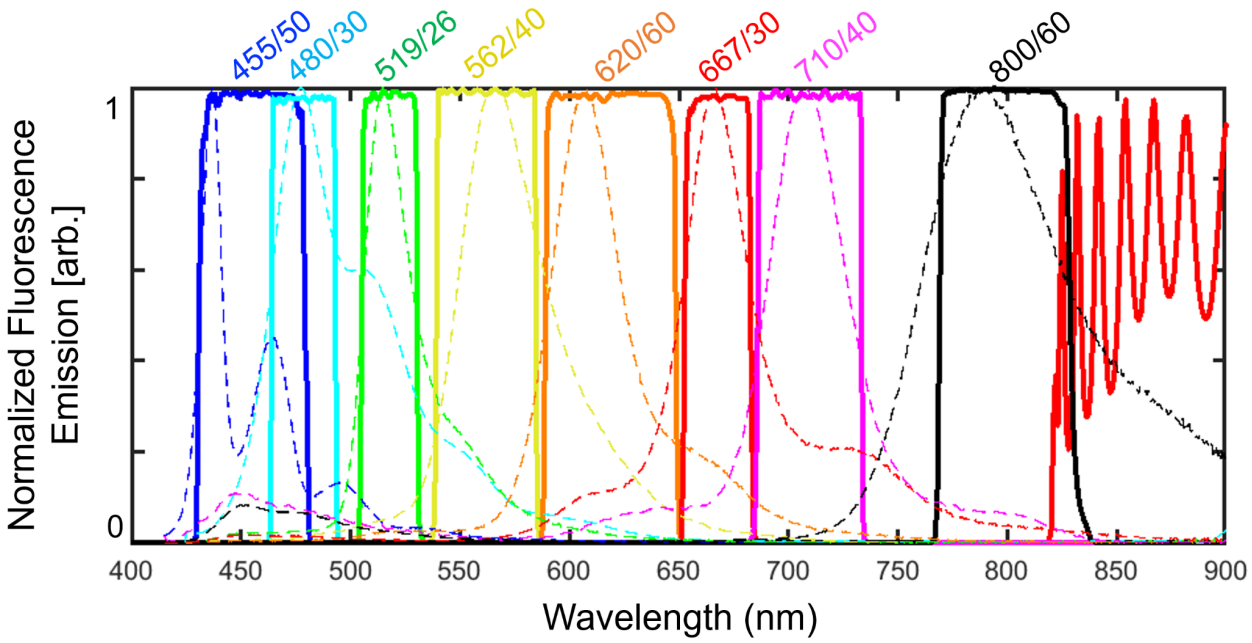

Supplementary Figure 2.7.2. Emission spectra and associated filters overlay. *Emission spectra of eight 405-excited Pdots (dashed lines) along with the associated dichroic filter reflectance (red oscillating line above 825 nm) and emission filter transmission (solid colored lines).*

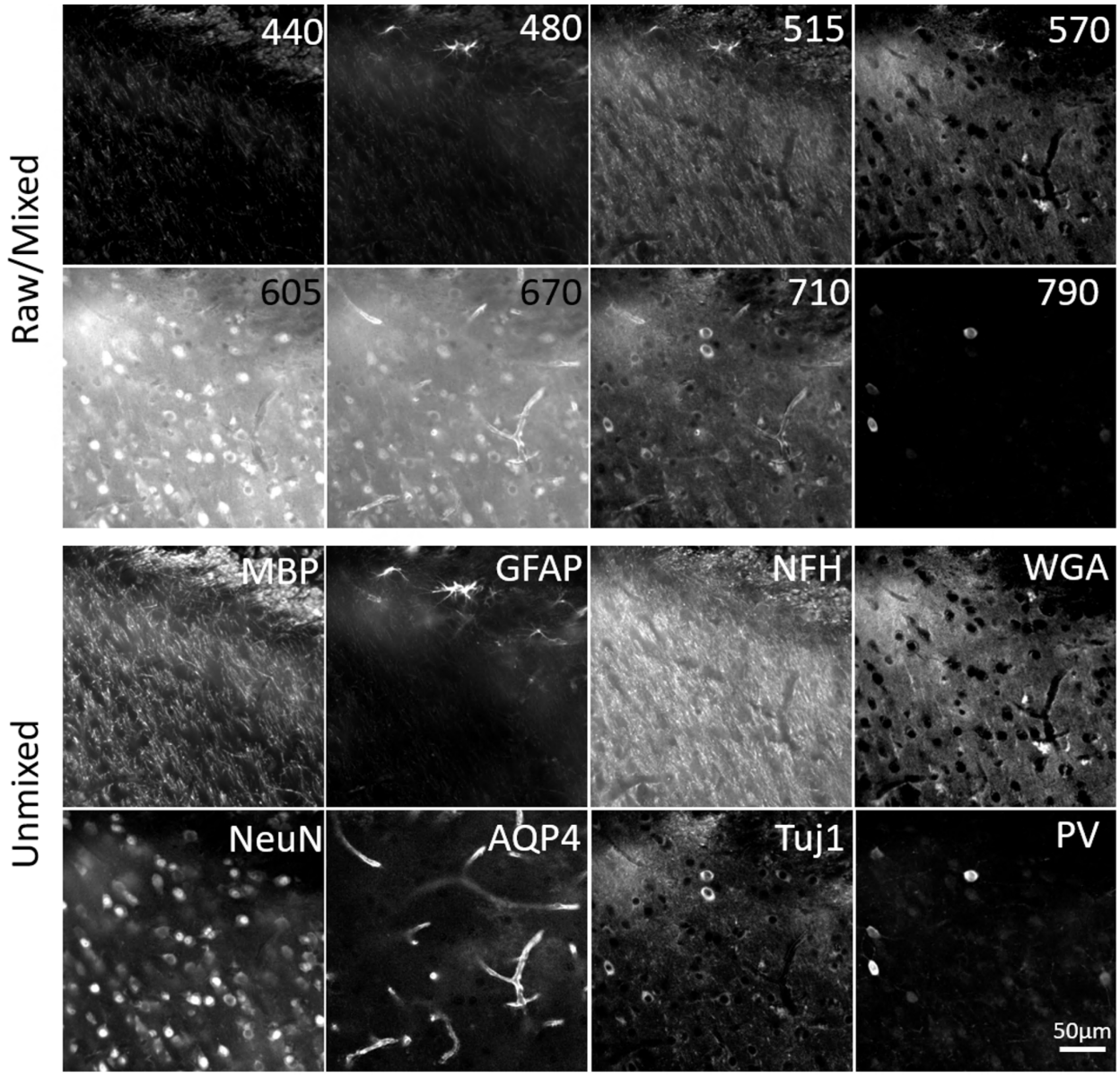

Supplementary Figure 2.7.3. Raw and processed image comparison for the data set shown in Figure 2.2. *Comparison of raw (mixed) images acquired at different emission wavelengths and the processed (unmixed) images that correspond to the primary antibody targets in mouse brain tissue, imaged at the amygdalar and piriform area.*

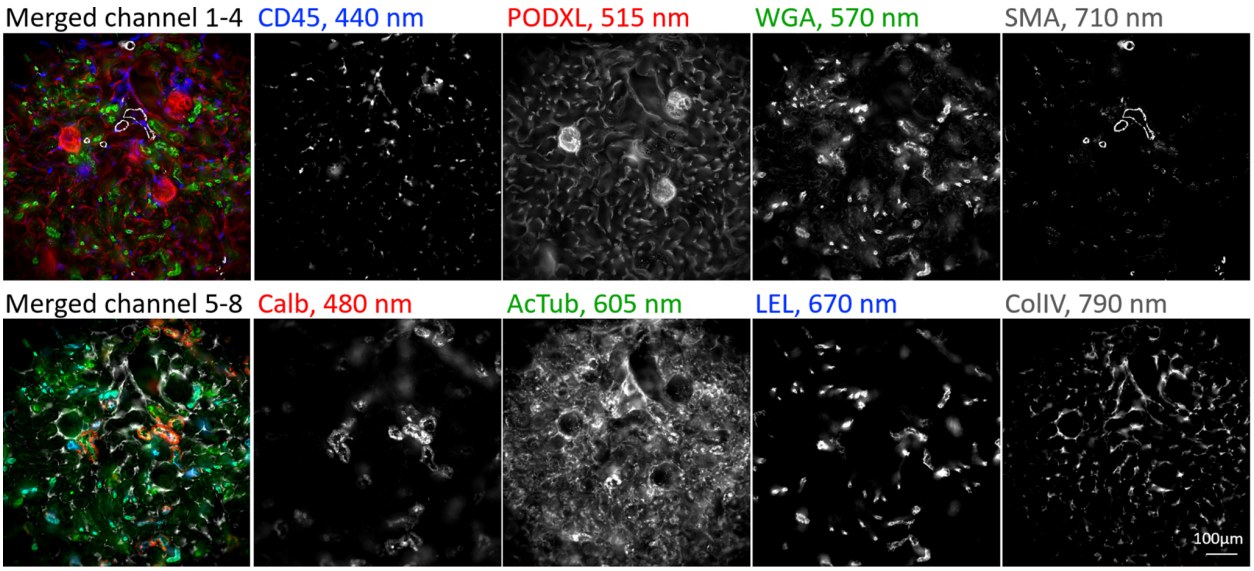

Supplementary Figure 2.7.4. Eight-channel emission multiplexing in the mouse kidney. *Unmixed images from indirect immunostaining of a 50 µm kidney slice using eight 405 nm-excited Pdot conjugates and imaged at the cortex region of the kidney.*

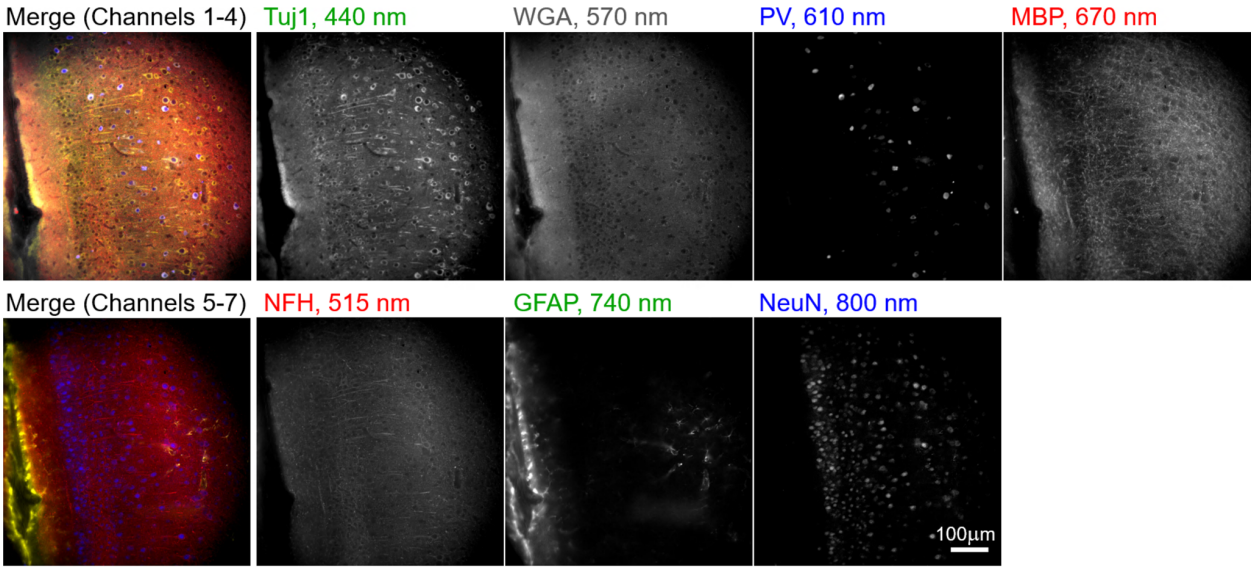

Supplementary Figure 2.7.5. Seven-channel emission multiplexing in the mouse brain. *Unmixed images from indirect immunofluorescence staining of a 100 μm thick mouse brain slice using seven 355 nm-excited Pdot conjugates and imaged at the anterior cingulate area of the brain.*

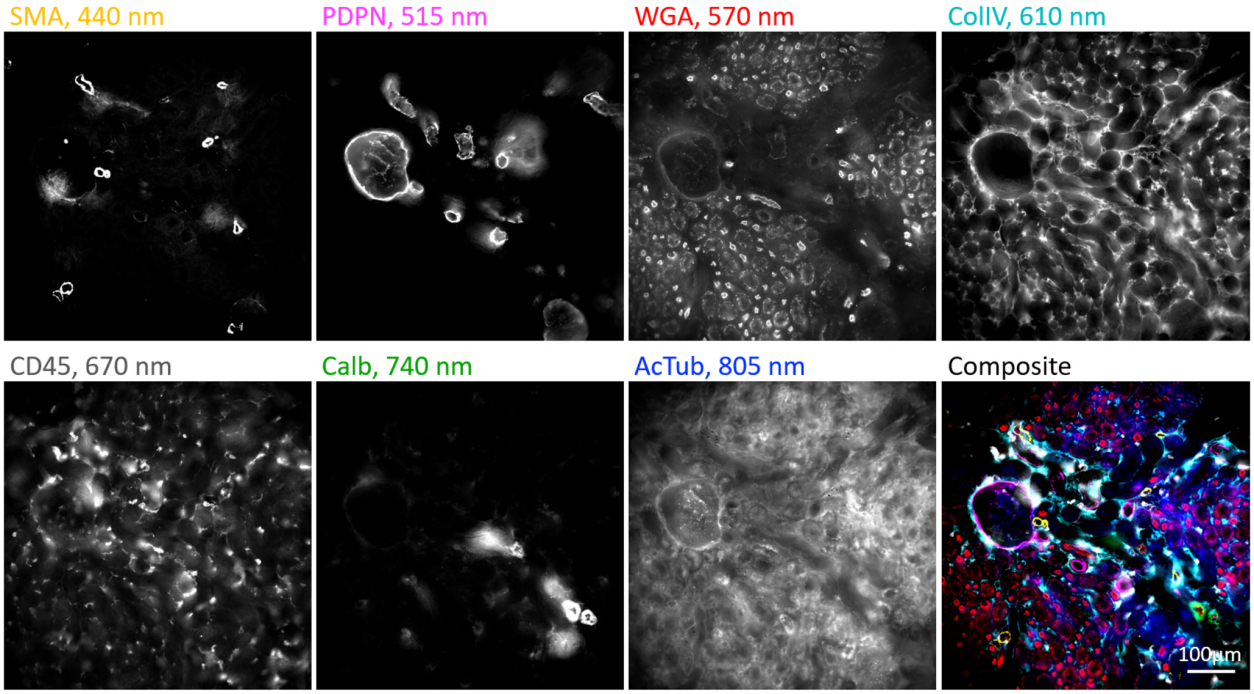

Supplementary Figure 2.7.6. Seven-channel emission multiplexing in the mouse kidney. *Unmixed images from indirect immunostaining of a 50 µm kidney slice using seven 355 nm-excited Pdot conjugates and imaged at the cortex region of the kidney.*

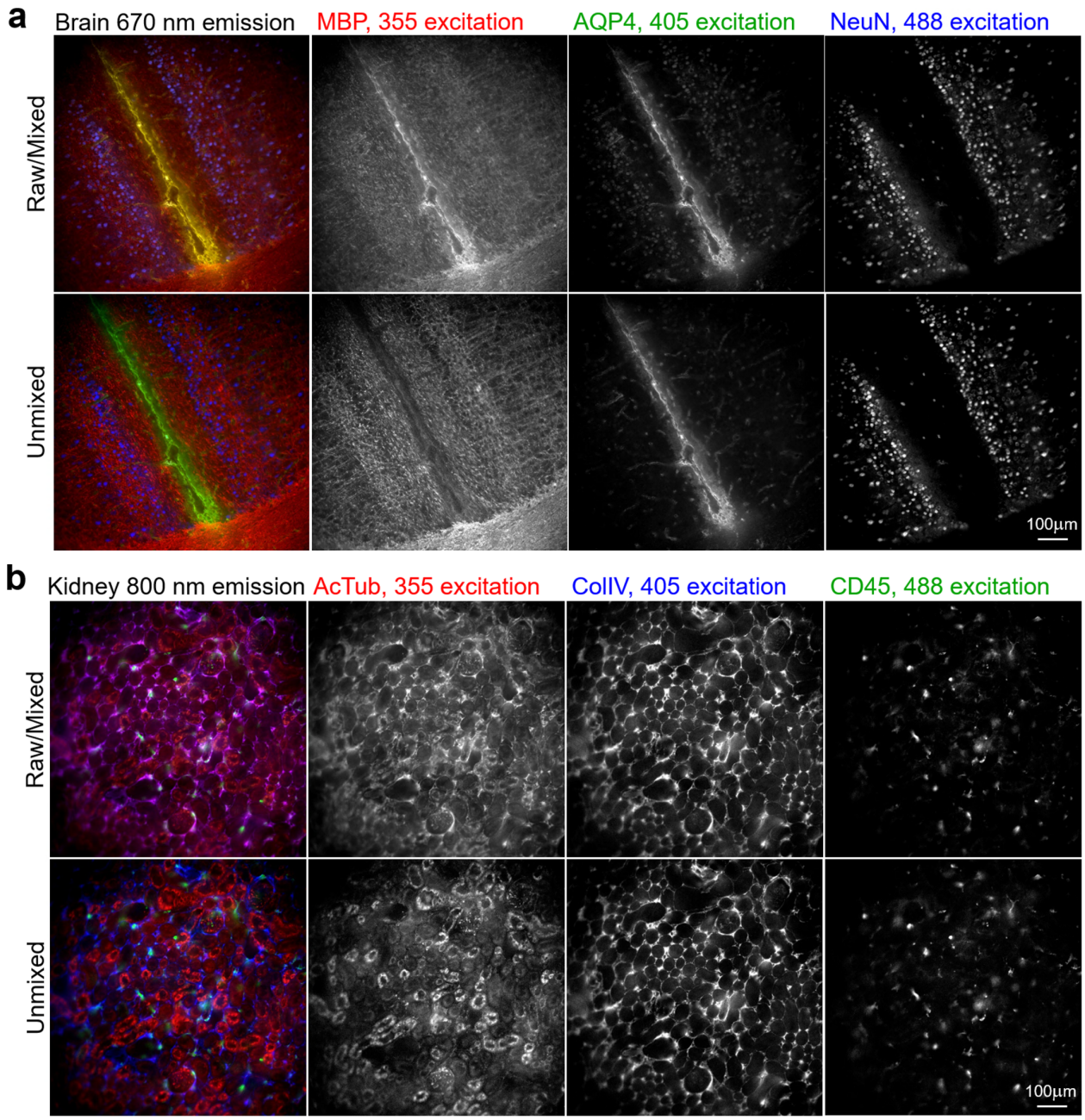

Supplementary Figure 2.7.7. Three-channel excitation multiplexing in the mouse brain and mouse kidney. *A comparison of mixed (rows 1,3) and linearly unmixed (row 2,4) images for the data set shown in* ***Figure 2.3****. (a): A 100 µm thick mouse brain slice was stained using three Pdots with different excitation maxima. The brain section was imaged above the medial corpus callosum region and emission was collected with the same emission filter for all three channels. (b): A 100 µm thick mouse kidney slice was stained using three Pdots with different excitation maxima. The kidney section was imaged at the cortex region and emission was collected with the same emission filter for all three channels.*

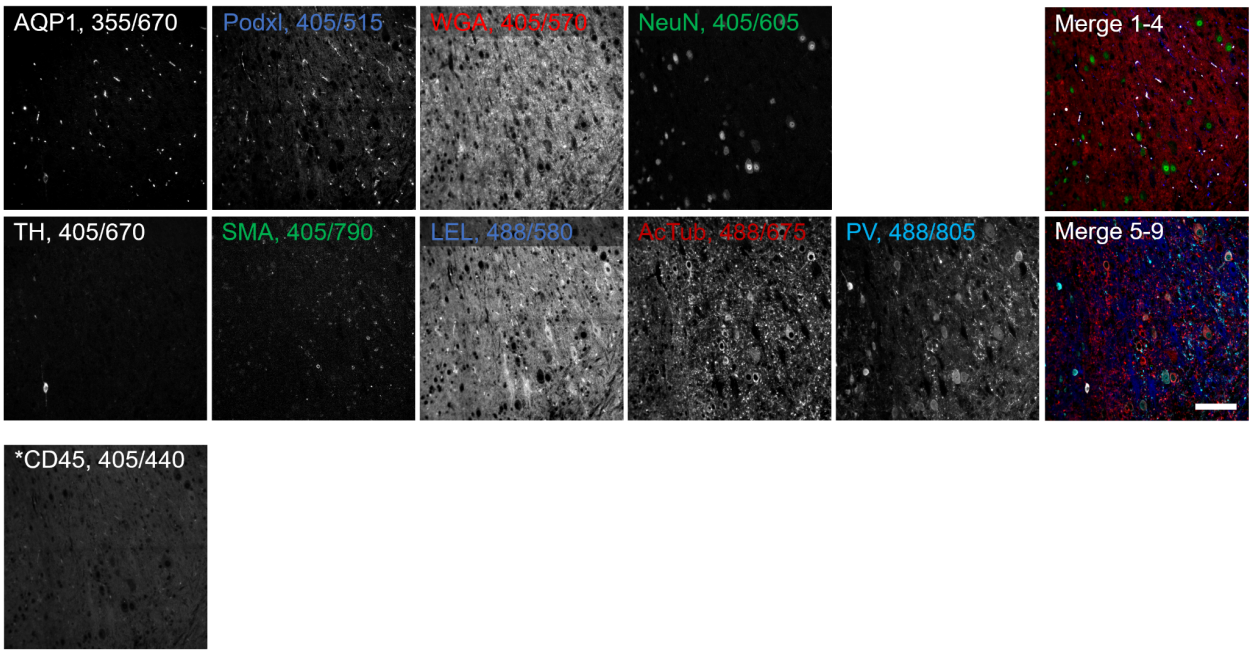

Supplementary Figure 2.7.8. 10-channel Pdot staining of mouse cerebellum FFPE tissue. *The images in the five columns to the left show grayscale images for individual molecular targets in the mouse cerebellum. The rightmost column shows 4-channel composite images of the same tissue region. CD45, shown with an asterisk (*) in the bottom row, is not expressed in this region of the brain. The scale bar is 100 µm. Labels indicate the protein targets or lectins together with Pdot excitation/emission wavelengths. (AQP1 = aquaporin 1, PODXL = podocalyxin, WGA = wheat germ agglutinin lectin, NeuN = neuronal nuclei, TH = tyrosine hydroxylase, SMA = alpha-smooth muscle actin, LEL = lycopersicon esculentum tomato lectin, AcTub = acetylated tubulin, PV = parvalbumin, CD45 = leukocyte common antigen).*

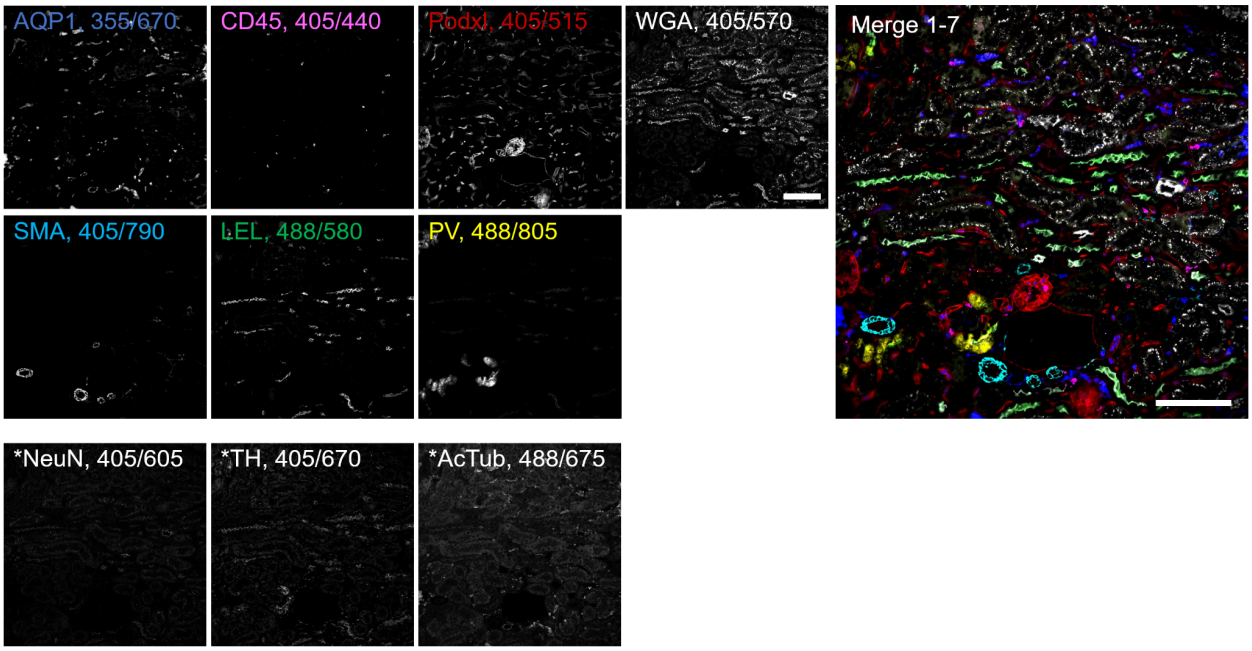

Supplementary Figure 2.7.9. 10-channel Pdot staining of mouse kidney FFPE tissue. *The images in the four columns to the left show grayscale images for individual molecular targets in the mouse kidney. The rightmost column shows a 7-channel composite image of the same tissue region. NeuN, TH, and AcTub, shown with a asterisk (*) in the bottom row, were either not expressed in the kidney or showed very low levels of staining in this specimen. All scale bars are 100 μm. Labels indicate the protein targets or lectins together with Pdot excitation/emission wavelengths. (AQP1 = aquaporin 1, PODXL = podocalyxin, WGA = wheat germ agglutinin lectin, NeuN = neuronal nuclei, TH = tyrosine hydroxylase, SMA = alpha-smooth muscle actin, LEL = lycopersicon esculentum tomato lectin, AcTub = acetylated tubulin, PV = parvalbumin, CD45 = leukocyte common antigen).*

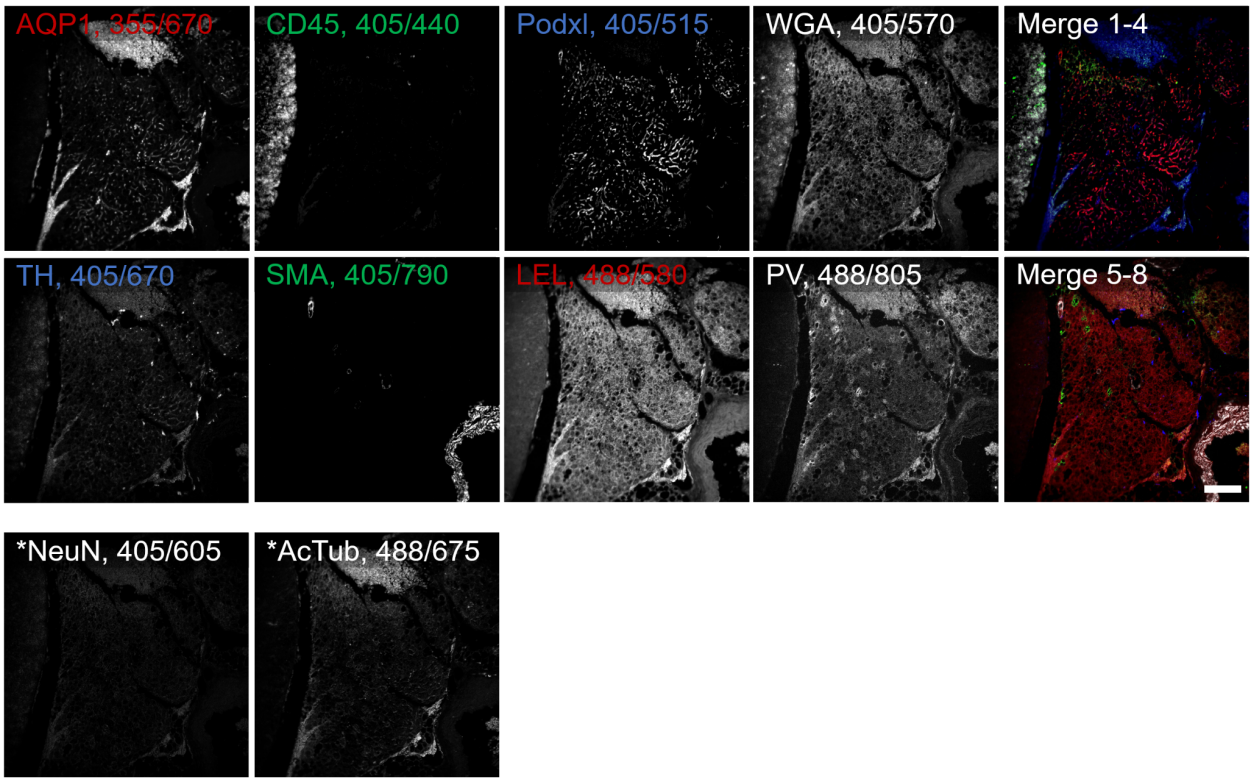

Supplementary Figure 2.7.10. 10-channel Pdot staining of mouse thymus FFPE tissue. *The images in the four columns to the left show grayscale images for individual molecular targets in the mouse thymus. The rightmost column shows 4-channel composite images of the same tissue region. NeuN and AcTub, shown with asterisks (*) in the bottom row, were either not expressed in the thymus or showed very low levels of staining in this specimen. The scale bar is 100 μm. Labels indicate the protein targets or lectins together with Pdot excitation/emission wavelengths. (AQP1 = aquaporin 1, PODXL = podocalyxin, WGA = wheat germ agglutinin lectin, NeuN = neuronal nuclei, TH = tyrosine hydroxylase, SMA = alpha-smooth muscle actin, LEL = lycopersicon esculentum tomato lectin, AcTub = acetylated tubulin, PV = parvalbumin, CD45 = leukocyte common antigen).*

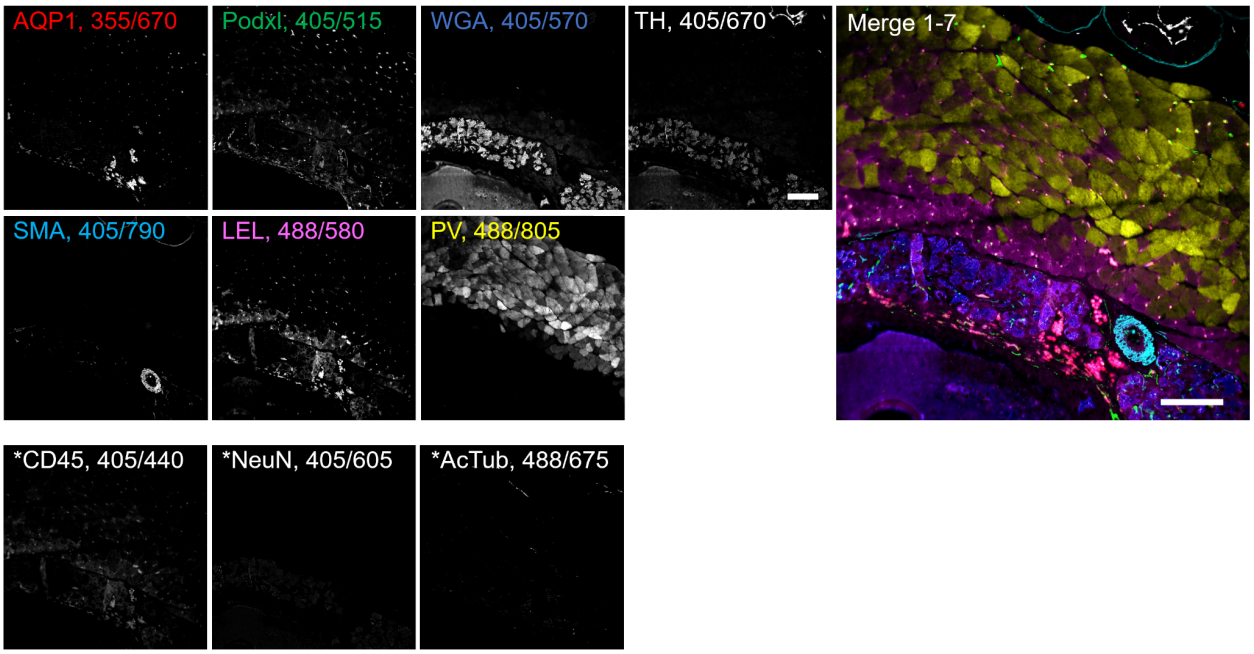

Supplementary Figure 2.7.11. 10-channel Pdot staining of mouse prostate FFPE tissue. *The images in the four columns to the left show grayscale images for individual molecular targets in the mouse prostate. The rightmost column shows a 7-channel composite image of the same tissue region. CD45, NeuN, and AcTub, shown with asterisks (*) in the bottom row, were either not expressed in the prostate or showed very low levels of staining in this specimen. All scale bars are 100 μm. Labels indicate the protein targets or lectins together with Pdot excitation/emission wavelengths. (AQP1 = aquaporin 1, PODXL = podocalyxin, WGA = wheat germ agglutinin lectin, NeuN = neuronal nuclei, TH = tyrosine hydroxylase, SMA = alpha-smooth muscle actin, LEL = lycopersicon esculentum tomato lectin, AcTub = acetylated tubulin, PV = parvalbumin, CD45 = leukocyte common antigen).*

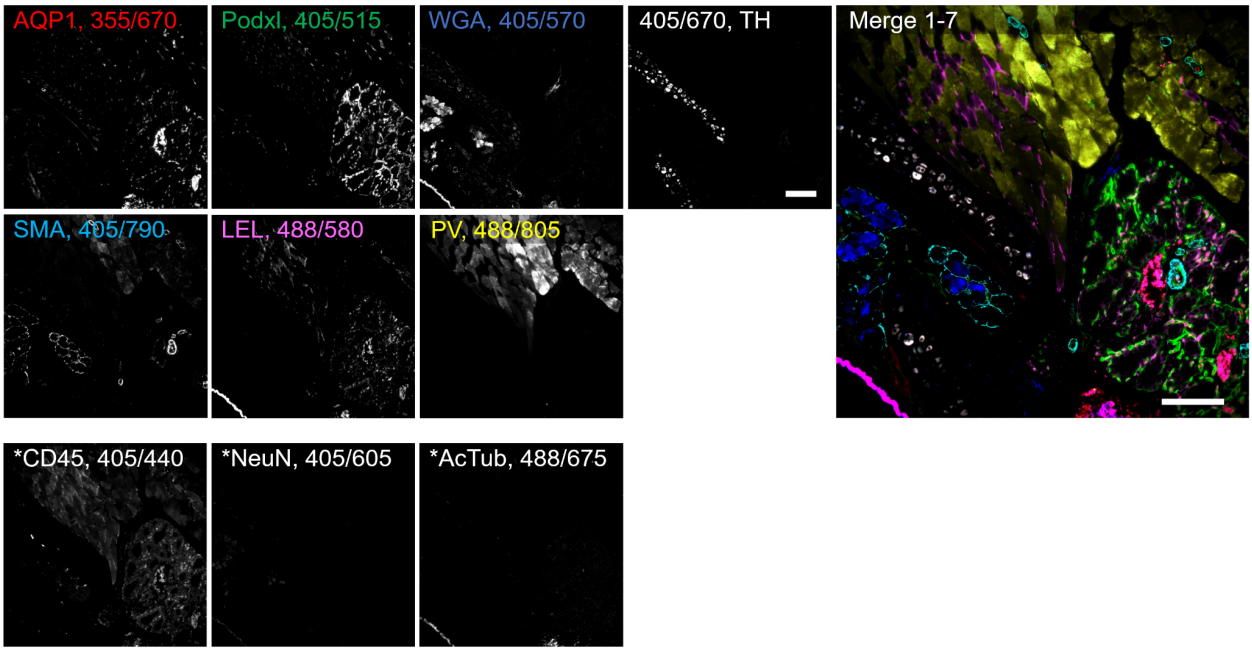

Supplementary Figure 2.7.12. 10-channel Pdot staining of mouse larynx FFPE tissue. *The images in the four columns to the left show grayscale images for individual molecular targets in the mouse larynx. The rightmost column shows a 7-channel composite image of the same tissue region. CD45, NeuN, and AcTub, shown with asterisks (*) in the bottom row, were either not expressed in the larynx or showed very low levels of staining in this specimen. All scale bars are 100 μm. Labels indicate the protein targets or lectins together with Pdot excitation/emission wavelengths. (AQP1 = aquaporin 1, PODXL = podocalyxin, WGA = wheat germ agglutinin lectin, NeuN = neuronal nuclei, TH = tyrosine hydroxylase, SMA = alpha-smooth muscle actin, LEL = lycopersicon esculentum tomato lectin, AcTub = acetylated tubulin, PV = parvalbumin, CD45 = leukocyte common antigen).*

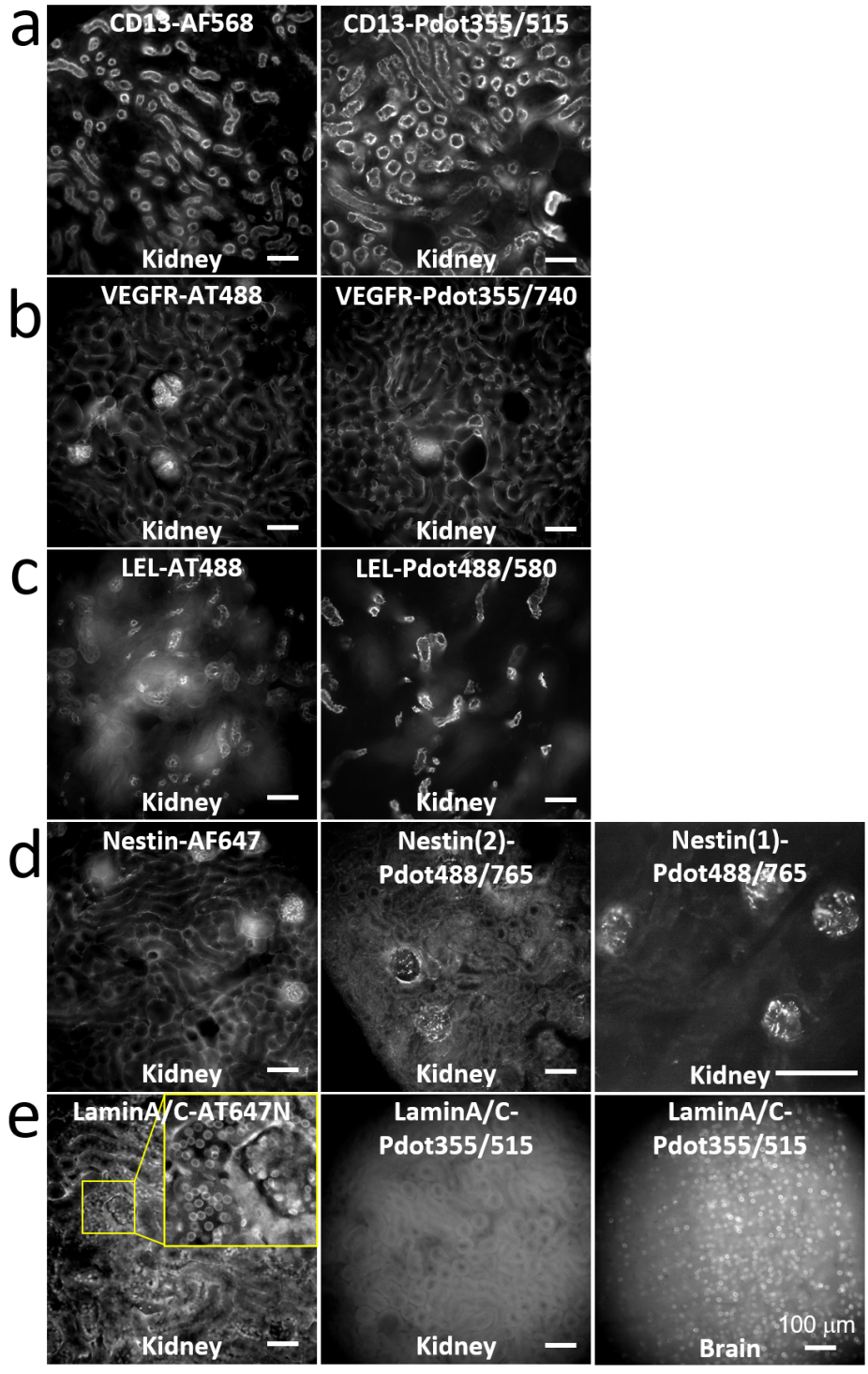
a
CD13-AF568
Kidney
CD13-Pdot355/515
Kidney
b
VEGFR-AT488
Kidney
VEGFR-Pdot355/740
Kidney
c
LEL-AT488
Kidney
LEL-Pdot488/580
Kidney
d
Nestin-AF647
Kidney
Nestin(2)-
Pdot488/765
Kidney
Nestin(1)-
Pdot488/765
Kidney
e
LaminA/C-AT647N
Kidney
LaminA/C-
Pdot355/515
Kidney
LaminA/C-
Pdot355/515
100 μm
Brain

Supplementary Figure 2.7.13. Methodology for validation of Pdot-antibody conjugates. *Kidney and brain tissue sections were stained for a single molecular target using direct or indirect immunostaining. The left column shows the results of staining using antibodies conjugated with conventional small molecule dyes. The right column shows the results of staining using antibodies conjugated with Pdots. Rows (a-c) showed the correct staining pattern using antibody-Pdot conjugates or lectin-Pdot conjugates. In row (d), Nestin(2) antibody, when conjugated to Pdot488/765, showed partial loss of antigenicity or weak staining. When the Pdot conjugation was repeated with another Nestin antibody (Nestin(1)), it showed the correct staining pattern. In row (e), the LaminA/C antibody conjugated to Pdot355/515 showed little to no stain in the kidney but showed good nuclear stain in brain tissue. This difference in staining between kidney and brain may result from either a greater abundance of the protein in brain vs kidney tissue (relative to the background signal for each) or from different efficiencies of binding of the antibody to the relevant lamin a/c splice isoforms in brain and kidney.*

(a) *Rat anti-CD13 + Donkey anti-Rat AF568 (left); Rat anti-CD13, Pdot355/515 (right)*
(b) *Rat anti-VEGFR + Donkey anti-Rat AT488 (left); Rat anti-VEGFR, Pdot355/740 (right)*
(c) *LEL-AT488 (left); LEL-Pdot488/580 (right)*
(d) *Mouse IgG1 Nestin + Goat anti-mouse AF647 (left); mouse IgG1 Nestin(2), Pdot488/765 ; mouse IgG2a Nestin(1), Pdot488/765.*
(e) *Rabbit Lamin A/C + Donkey anti-Rabbit AT647N; Rabbit Lamin A/C, Pdot355/515.*

Supplementary Table 2.7.1. Summary of sample labeling and imaging setup. All experiments (except for **Supplementary Figure 2.7.13**) used a Ti2-E Nikon microscope, exposure time of 100 ms for fresh-cut tissues, 1000 ms for FFPE tissues, 20x objective lens, SOLA light engine, ORCA Flash 4.0 camera, immunostaining procedure, and 20–24 hour incubation time; secondary antibodies are all from Jackson ImmunoResearch. More details are provided in the Methods section.

Figure **Tissue** **Thickness**	**Primary Antibody**	**Secondary Antibody**	**Filter Combinations**		
			Dichroic:	*Excitation filter:*	*Emission filters:*
2.2, S2.7.3	MBP	Pdot405/440 Donkey anti-Rat	DI02-R405-25X36	zet405/20x	ET455/50m
Brain (Mouse 1)	GFAP	Pdot405/480 Donkey anti-Mouse IgG1	Same for all	Same for all	ET480/30m
100 µm section	NFH	Pdot405/515 Goat anti-Chicken			ET519/26m
	WGA	Pdot405/570 WGA			FF01-562/40
	NeuN	Pdot405/605 Goat anti-Mouse IgG2b			ET620/60m
	AQP4	Pdot405/670 Goat anti-Mouse IgG3			ET667/30m
	Tuj1	Pdot405/710 Goat anti-Mouse IgG2a			FF01-710/40
	PV	Pdot405/790 Donkey anti-Rabbit			ET800/60
			Dichroics:	*Excitation filters:*	*Emission filter:*
2.3A, S2.7.7	MBP	Pdot355/670 Donkey anti-Rat	FF376-DI01-25X36	zet365/20x	ET667/30m
Brain (Mouse 1)	AQP4	Pdot405/670 Goat anti-Mouse IgG3	DI02-R405-25X36	zet405/20x	ET667/30m
100 µm section	NeuN	Pdot488/675 Goat anti-Mouse IgG2b	DI02-R488-25X36	zet488/10x	ET667/30m
			Dichroics:	*Excitation filters:*	*Emission filter:*
2.3B, S2.7.7	AcTub	Pdot355/800 Goat anti-Mouse IgG2b	FF376-DI01-25X36	zet365/20x	ET800/60
Kidney (Mouse 1)	ColIV	Pdot405/790 Donkey anti-Rabbit	DI02-R405-25X36	zet405/20x	ET800/60
100 µm section	CD45	Pdot488/805 Donkey anti-Rat	DI02-R488-25X36	zet488/10x	ET800/60
			Dichroics:	*Excitation filters:*	*Emission filters:*
2.4	Pdot355/400 SOX2 (1)	All primary conjugates, no secondaries	FF376-DI01-25X36	zet365/20x	ET405/30m
Brain (Mouse 3)	Pdot355/515 LMNA/C (1)	necessary	FF376-DI01-25X36	zet365/20x	ET519/26m
50 µm section	Pdot355/570 MAP2		FF376-DI01-25X36	zet365/20x	FF01-562/40
	Pdot355/740 VEGFR3 (1)		FF376-DI01-25X36	zet365/20x	ET740/40x
	Pdot405/440 GFAB		DI02-R405-25X36	zet405/20x	ET455/50m
	Pdot405/570 WGA		DI02-R405-25X36	zet405/20x	FF01-562/40
	Pdot405/605 NeuN		DI02-R405-25X36	zet405/20x	ET620/60m
	Pdot405/670 TH		DI02-R405-25X36	zet405/20x	FF01-562/40
	Pdot405/710 PV		DI02-R405-25X36	zet405/20x	FF01-710/40
	Pdot405/790 MBP		DI02-R405-25X36	zet405/20x	ET800/60
	Pdot488/515 Calb (1)		DI02-R488-25X36	zet488/10x	ET519/26m
	Pdot488/610 NFH		DI02-R488-25X36	zet488/10x	ET620/60m
	Pdot488/675 Tuj1		DI02-R488-25X36	zet488/10x	ET667/30m
	Pdot488/765 Nes		DI02-R488-25X36	zet488/10x	ET760/40
			Dichroics:	*Excitation filters:*	*Emission filters:*
2.5	Pdot355/440 PNA	All primary conjugates, no secondaries	FF376-DI01-25X36	zet365/20x	ET455/50m
Kidney (Mouse 2)	Pdot355/515 CD13	necessary	FF376-DI01-25X36	zet365/20x	ET519/26m
50 µm section	Pdot355/570 AQP2		FF376-DI01-25X36	zet365/20x	FF01-562/40
	Pdot355/610 ITGA8		FF376-DI01-25X36	zet365/20x	ET620/60m
	Pdot355/670 AQP1		FF376-DI01-25X36	zet365/20x	ET667/30m
	Pdot355/740 VEGFR3 (1)		FF376-DI01-25X36	zet365/20x	ET740/40x
	Pdot355/800 UMOD		FF376-DI01-25X36	zet365/20x	ET800/60
	Pdot405/440 CD45		DI02-R405-25X36	zet405/20x	ET455/50m
	Pdot405/480 Megalin		DI02-R405-25X36	zet405/20x	ET480/30m
	Pdot405/515 PODXL		DI02-R405-25X36	zet405/20x	ET519/26m
	Pdot405/570 WGA		DI02-R405-25X36	zet405/20x	FF01-562/40
	Pdot405/605 ColIV		DI02-R405-25X36	zet405/20x	ET620/60m
	Pdot405/670 LEL		DI02-R405-25X36	zet405/20x	ET667/30m
	Pdot405/710 Agrin		DI02-R405-25X36	zet405/20x	FF01-710/40
	Pdot405/790 α-SMA		DI02-R405-25X36	zet405/20x	ET800/60
	Pdot488/515 Calb (1)		DI02-R488-25X36	zet488/10x	ET519/26m
	Pdot488/580 PDPL		DI02-R488-25X36	zet488/10x	FF01-562/40
	Pdot488/610 REN		DI02-R488-25X36	zet488/10x	ET620/60m
	Pdot488/675 AcTub		DI02-R488-25X36	zet488/10x	ET667/30m
	Pdot488/765 Nes		DI02-R488-25X36	zet488/10x	ET760/40
	Pdot488/805 PV		DI02-R488-25X36	zet488/10x	ET800/60

			Dichroic: DI02-R405-	*Excitation filter:*	*Emission filters:*
S2.7.4	CD45	Pdot405/440 Donkey anti-Rat	25X36	zet405/20x	ET455/50m
Kidney (Mouse 2)	Calb	Pdot405/480 Donkey anti-Mouse IgG1	Same for all	Same for all	ET480/30m
50 µm section	PODXL	Pdot405/515 PODXL			ET519/26m
	WGA	Pdot405/570 WGA			FF01-562/40
	AcTub	Pdot405/605 Goat anti-Mouse IgG2b			ET620/60m
	LEL	Pdot405/670 LEL			ET667/30m
	α-SMA	Pdot405/710 Goat anti-Mouse IgG2a			FF01-710/40
	ColIV	Pdot405/790 Donkey anti-Rabbit			ET800/60
			Dichroics:	*Excitation filters:*	*Emission filters:*
S2.7.5	Tuj1	Pdot355/440 Goat anti-mouse IgG2a	FF376-DI01-25X36	zet365/20x	ET455/50m
Brain (Mouse 1)	NFH	Pdot355/515 Donkey anti-Chicken	Same for all	Same for all	ET519/26m
100 µm section	WGA	Pdot355/570 WGA			FF01-562/40
	PV	Pdot355/610 Donkey anti-Rabbit			ET620/60m
	MBP	Pdot355/670 Donkey anti-Rat			ET667/30m
	GFAB	Pdot355/740 Goat anti-Mouse IgG1			ET740/40x
	NeuN	Pdot355/800 Goat anti-Mouse IgG2b			ET800/60
			Dichroics:	*Excitation filters:*	*Emission filters:*
S2.7.6	α-SMA	Pdot355/440 Goat anti-mouse IgG2a	FF376-DI01-25X36	zet365/20x	ET455/50m
Kidney (Mouse 2)	PDPN	Pdot355/515 Donkey anti-Hamster	Same for all	Same for all	ET519/26m
50 µm section	WGA	Pdot355/570 WGA			FF01-562/40
	ColIV	Pdot355/610 Donkey anti-Rabbit			ET620/60m
	CD45	Pdot355/670 Donkey anti-Rat			ET667/30m
	Calb	Pdot355/740 Goat anti-Mouse IgG1			ET740/40x
	AcTub	Pdot355/800 Goat anti-Mouse IgG2b			ET800/60
			Dichroics:	*Excitation filters:*	*Emission filters:*
S2.7.8–S2.7.12	Pdot355/670 AQP1	All primary conjugates, no secondaries	FF376-DI01-25X36	zet365/20x	ET667/30m
Mouse Tissue	Pdot405/440 CD45	necessary	DI02-R405-25X36	zet405/20x	ET455/50m
Microarray	Pdot405/515 PODXL		DI02-R405-25X36	zet405/20x	ET519/26m
5 µm section	Pdot405/570 WGA		DI02-R405-25X36	zet405/20x	FF01-562/40
	Pdot405/605 NeuN		DI02-R405-25X36	zet405/20x	ET620/60m
	Pdot405/670 TH		DI02-R405-25X36	zet405/20x	ET667/30m
	Pdot405/790 α-SMA		DI02-R405-25X36	zet405/20x	ET800/60
	Pdot488/580 LEL		DI02-R488-25X36	zet488/10x	FF01-562/40
	Pdot488/675 AcTub		DI02-R488-25X36	zet488/10x	ET667/30m
	Pdot488/805 PV		DI02-R488-25X36	zet488/10x	ET800/60
			Dichroics:	*Excitation filters:*	*Emission filters:*
S2.7.13	CD13	AF568 Donkey anti-Rat	zt405/488/561/640rpc v2-UF2	- (LED control)	ET595/44m
Kidney and Brain					
(Mouse 3)	Pdot355/515 CD13	-	FF376-DI01-25X36	zet365/20x	ET519/26m
50 µm section	VEGFR	AT488 Donkey anti-Rat	DI02-R488-25X36	zet488/10x	ET519/26m
	Pdot355/740 VEGFR	-	FF376-DI01-25X36	zet365/20x	ET740/40x
	AT488 LEL	-	DI02-R488-25X36	zet488/10x	ET519/26m
	Pdot488/580 LEL	-	DI02-R488-25X36	zet488/10x	FF01-562/40
	Nestin	AF647 Goat anti-mouse	zt405/488/561/640rpc v2-UF2	- (LED control)	ET700/75m
	Pdot488/765 Nestin(2)	-	DI02-R488-25X36	zet488/10x	ET760/40
	Pdot488/765 Nestin(1)	-	DI02-R488-25X36	zet488/10x	ET760/40
	Lamin A/C	AT647N Donkey anti-Rabbit	zt405/488/561/640rpc v2-UF2	- (LED control)	ET700/75m
	Pdot355/515 Lamin A/C	-	FF376-DI01-25X36	zet365/20x	ET519/26m

Supplementary Table 2.7.2. Pdot-secondary antibody conjugates.

	Primary Antibody or Lectin	Protein Target or Lectin	Host	Vendor	Catalog #	Clonality	Pdot Conjugated Secondary Antibody or Lectin	Catalog #
Brain - 355ex	Tuj1/TUBB3	Tubulin β 3	Mouse IgG2a	BioLegend	801201	monoclonal	Pdot355/440 Goat anti-mouse IgG2a	115-005-206
	NFH	Neurofilament Heavy Chain	Chicken	Aves Labs	NFH		Pdot355/515 Donkey anti-Chicken	703-005-155
	WGA	Wheat Germ Agglutinin		Vector Labs	L-1020		Pdot355/570 WGA	-
	PV	Parvalbumin	Rabbit	Abcam	ab11427	polyclonal	Pdot355/610 Donkey anti-Rabbit	711-005-152
	MBP	Myelin Basic Protein	Rat	Abcam	ab7349	monoclonal	Pdot355/670 Donkey anti-Rat	712-005-153
	GFAP	Glial Fibrillary Acidic Protein	Mouse IgG1	Cell Signaling	3670S	monoclonal	Pdot355/740 Goat anti-mouse IgG1	115-005-205
	NeuN	Neuronal Nuclei	Mouse IgG2b	Encor	MCA-1B7	monoclonal	Pdot355/800 Goat anti-mouse IgG2b	115-005-207
Kidney - 355ex	α-SMA	alpha-Smooth Muscle Actin	Mouse IgG2a	BioLegend	904601	monoclonal (1A4)	Pdot355/440 Goat anti-mouse IgG2a	115-005-206
	PDPN	Podoplanin	Syrian Hamster IgG	DSHB	8.1.1-s	monoclonal	Pdot355/515 Donkey anti-Hamster	Unavailable
	WGA	Wheat Germ Agglutinin		Vector Labs	L-1020		Pdot355/570 WGA	-
	AQP1	Aquaporin 1	Rabbit	Abcam	ab15080	polyclonal	Pdot355/610 Donkey anti-Rabbit	711-005-152
	CD45	Leukocyte Common Antigen	Rat	BioLegend	103101	monoclonal (30-F11)	Pdot355/670 Donkey anti-Rat	712-005-153
	Calb	Calbindin	Mouse IgG1	Abcam	ab82812	monoclonal	Pdot355/740 Goat anti-mouse IgG1	115-005-205
	AcTub	Acetylated Tubulin	Mouse IgG2b	Sigma	T7451-25UL	monoclonal (6-11B-1)	Pdot355/800 Goat anti-mouse IgG2b	115-005-207
Brain - 405ex	MBP	Myelin Basic Protein	Rat	Abcam	ab7349	monoclonal	Pdot405/440 Donkey anti-Rat	712-005-153
	GFAP	Glial fibrillary acidic protein	Mouse IgG1	Cell Signaling	3670S	monoclonal	Pdot405/480 Donkey anti-mouse IgG1	115-005-205
	NFH	Neurofilament Heavy-chain	Chicken	Aves Labs	NFH	polyclonal	Pdot405/515 Goat anti-chicken	103-005-155
	WGA	Wheat Germ Agglutinin		Vector Labs	L-1020		Pdot405/570 WGA	-
	NeuN	Neuronal Nuclei	Mouse IgG2b	Encor	MCA-1B7	monoclonal	Pdot405/605 Goat anti-mouse IgG2b	115-005-207
	AQP4	Aquaporin 4	Mouse IgG3	Santa Cruz Biotechnology	sc-32739	monoclonal	Pdot405/670 Goat anti-mouse IgG3	115-005-209
	Tuj1/TUBB3	Tubulin β 3	Mouse IgG2a	BioLegend	801201	monoclonal	Pdot405/710 Goat anti-mouse IgG2a	115-005-206
	PV	Parvalbumin	Rabbit	Abcam	ab11427	polyclonal	Pdot405/790 Donkey anti-rabbit	711-005-152
Kidney - 405ex	CD45	Leukocyte Common Antigen	Rat IgG2b	BioLegend	103101	monoclonal (30-F11)	Pdot405/440 Donkey anti-Rat	712-005-153
	Calb	Calbindin	Mouse IgG1	Abcam	ab82812	monoclonal	Pdot405/480 Donkey anti-mouse IgG1	115-005-205
	PODXL	Podocalyxin	Goat	R&D Systems	AF1556		Pdot405/515 Goat anti-PODXL	-
	WGA	Wheat Germ Agglutinin		Vector Labs	L-1020		Pdot405/570 WGA	-
	AcTub	Acetylated Tubulin	Mouse IgG2b	Sigma	T7451-25UL	monoclonal (6-11B-1)	Pdot405/605 Goat anti-mouse IgG2b	115-005-207
	LEL	Lycopersicon Esculentum Tomato Lectin		Vector Labs	L-1170-2		Pdot405/670 LEL	-
	α-SMA	alpha-Smooth Muscle Actin	Mouse IgG2a	BioLegend	904601	monoclonal (1A4)	Pdot405/710 Goat anti-mouse IgG2a	115-005-206
	ColIV	Collagen IV	Rabbit	Abcam	ab6586	polyclonal	Pdot405/790 Donkey anti-rabbit	711-005-152
Brain - 488ex	Tuj1/TUBB3	Tubulin β 3	Mouse IgG2a	BioLegend	801201	monoclonal	Pdot488/610-Goat anti-mouse IgG2a	115-005-206
	NeuN	Neuronal Nuclei	Mouse IgG2b	Encor	MCA-1B7	monoclonal	Pdot488/675-Goat anti-mouse IgG2b	115-005-207
	MBP	Myelin Basic Protein	Rat	Abcam	ab7349	monoclonal	Pdot488/805-Donkey anti-Rat	712-005-153
Kidney - 488ex	α-SMA	alpha-Smooth Muscle Actin	Mouse IgG2a	BioLegend	904601	monoclonal (1A4)	Pdot488/610-Goat anti-mouse IgG2a	115-005-206
	AcTub	Acetylated Tubulin	Mouse IgG2b	Sigma	T7451-25UL	monoclonal (6-11B-1)	Pdot488/675-Goat anti-mouse IgG2b	115-005-207
	CD45	Leukocyte Common Antigen	Rat	BioLegend	103101	monoclonal (30-F11)	Pdot488/805-Donkey anti-Rat	712-005-153

Supplementary Table 2.3. Pdot-primary antibody conjugates.

Pdot	Antibody or Lectin	Protein Target or Lectin	Performance	Host	Vendor	Catalog #
355-400	CD31/PECAM-1	Cluster of Designation 31, Platelet Endothelial Cell Adhesion Molecule-1	++	Goat	R&D Systems	AF3628
355-400*	SOX2 (1)	Sex Determining Region Y-Box 2	+++	Goat	Novus Biologicals	AF2018
355-400	SOX2 (2)	Sex Determining Region Y-Box 2	++	Mouse IgG1	Thermo Fisher	66411-1-IG
355-440	Tuj1/TUBB3	Tubulin β 3	+	Mouse IgG2a	BioLegend	801201
355-440†	PNA	Peanut Agglutinin	+++	-	Vector	L-1070-25
355-440	SYNPO	Synaptopodin	+	Rabbit	Thermo Fisher	TA890150
355-515†	CD13/APN	Cluster of Designation 13, Aminopeptidase N	+++	Rat IgG2a	Thermo Fisher	MA1-33449
355-515*	LAMIN A/C (1)	Lamin A/C	+++	Rabbit	Proteintech	10298-1-AP
355-515	Podocin (1)	Podocin	+	Rabbit	Millipore Sigma	P0372-200UL
355-570†	AQP2	Aquaporin 2	+++	Rabbit	Novus Biological	NB110-74682
355-570*	MAP2	Microtubule Associated Protein 2	+++	Chicken IgGY	Novus Biologicals	NB300-213
355-610	AQP4 (1)	Aquaporin-4	+	Rabbit	Millipore Sigma	HPA014784-100UL
355-610	AQP4 (2)	Aquaporin-4	+	Rabbit	LSBio	LS-C150456
355-610	Nephrin	Nephrin	+	Goat	R&D Systems	AF3159
355-610	CD45	Cluster of Designation 45, Leukocyte Common Antigen	+++	Rat IgG2b	BioLegend	103102
355-610†	ITGA8	Integrin alpha 8	+++	Goat	Novus Biologicals	AF4076
355-610	Podocin (2)	Podocin	+	Rabbit	Thermo Fisher	PA5-37284
355-670†	AQP1	Aquaporin 1	+++	Rabbit	Proteintech	20333-1-AP
355-670	PNA	Peanut Agglutinin	++	-	Vector	L-1070-5
355-740*†	VEGFR3	Vascular Endothelial Growth Factor Receptor 3	+++	Rat	Novus Biologicals	NB110-61018, 2022
355-740	VIM	Vimentin	++	IgG2a	R&D Systems	MAB21052-100
355-805	GAD67	Glutamate Decarboxylase 1	+	Rabbit	LSBio	LS-C827246-100
355-805	CD90/Thy1	Cluster of Designation 90, Thymus Cell Antigen-1	+	Rat IgG1	Novus Biologicals	NB100-65543
355-805†	UMOD/THP	Uromodulin, Tamm-Horsfall Protein	+++	Rat IgG2a	R&D Systems	MAB5175
405-440†	CD45	Cluster of Designation 45, Leukocyte Common Antigen	+++	Rat IgG2b	BioLegend	103102
405-440*	GFAP	Glial Fibrillary Acidic Protein	+++	Chicken IgY	Thermo Fisher	PA1-10004
405-480	CD31/PECAM-1	Cluster of Designation 45, Platelet Endothelial Cell Adhesion Molecule-1	++	Goat	R&D Systems	AF3628
405-480†	Megalin/LRP2	Low Density Lipoprotein-related Protein 2	+++	Rabbit	Invitrogen	PA5-92032
405-515	NFL	Neurofilament Light Chain	+	Chicken	Aves Labs	NFL
405-515†	PODXL	Podocalyxin	+++	Goat	R&D Systems	AF1556
405-570*†	WGA	Wheat Germ Agglutinin	+++	-	Vector	L-1020-25
405-610†	ColIV	Collagen IV	+++	Rabbit	Abcam	ab6586
405-605*	NeuN	Neuronal Nuclei	+++	Mouse IgG2b	BioLegend	834501
405-670†	LEL	Lycopersicon Esculentum Tomato Lectin	+++	-	Vector	L-1170-2
405-670*	TH	Tyrosine Hydroxylase	++	Mouse IgG2a	BioLegend	818001
405-710†	Agrin	Agrin	+++	Goat	R&D Systems	AF550
405-710*	PV	Parvalbumin	+++	Rabbit	Novus Biologicals	NB120-11427
405-790†	α-SMA	alpha-Smooth Muscle Actin	+++	Mouse IgG2a	Millipore Sigma	A5228-200UL
405-790*	MBP	Myelin Basic Protein	+++	Mouse IgG2b	Invitrogen	MA1-10837
488-520*†	Calb (1)	Calbindin	+++	Rabbit	LSBio	LS-B16562-100

488-520	Calb (2)	Calbindin	++	Mouse IgG1	Abcam	ab82812
488-520	Calb (3)	Calbindin	+	Chicken	Novus Biologicals	NBP2-50028
488-580†	PDPN	Podoplanin	++	Goat	R&D Systems	AF3244
488-580	LEL	Lycopersicon Esculentum Tomato Lectin	+++	-	Vector	L-1170-2
488-610*	NFH	Neurofilament Heavy Chain	+++	Chicken IgY	Aves Labs	NFH
488-610†	REN	Renin	+++	Goat	R&D Systems	AF4277
488-675†	AcTub	Acetylated Tubulin	+++	Mouse IgG2b	Millipore Sigma	T7451-200UL
488-675*	Tuj1/TUBB3	Tubulin β 3	+++	Mouse IgG2b	BioLegend	MMS-435P
488-765*†	Nes/Nestin (1)	Neuroepithelial stem cell protein	+++	Mouse IgG2a	R&D Systems	MAB2736
488-765	Nestin (2)	Neuroepithelial stem cell protein	++	Mouse IgG1	Novus Biologicals	NB300-266
488-765	SYNPO (1)	Synaptopodin	+	Rabbit	Millipore Sigma	S9442-200UL
488-810	CK8	Cytokeratin 8	+	Rabbit	LSBio	LS-B7928-50
488-810	LMNB1 (1)	Lamin B1	++	Mouse IgG1	Proteintech	66095-1-Ig
488-810†	PV	Parvalbumin	+++	Rabbit	Novus Biologicals	NB120-11427

* labeled are used in brain 14-panel stain
† labeled are used in kidney 21-panel stain
+++ Positive and correct signals in multiple samples
++ Positive and correct signals in some tested samples
+ Images dominated by autofluorescence or exhibiting incorrect non-specific signals in most samples

Supplementary Table 2.7.4. Optical filters.

	Chroma	Semrock
Dichroics (longpass)		DI02-R405-25X36
		DI02-R488-25X36
		FF376-DI01-25X36
		zt405/488/561/640rpcv2-UF2
Excitation filters	zet365/20x	
	zet405/20x	
	zet488/10x	
Emission filters	ET405/30m	FF01-562/40
	ET455/50m	FF01-710/40
	ET480/30m	
	ET519/26m	
	ET595/44m	
	ET620/60m	
	ET667/30m	
	ET700/75m	
	ET740/40x	
	ET760/40	
	ET800/60	

2.8. References

(1) Hickey, J. W.; Neumann, E. K.; Radtke, A. J.; Camarillo, J. M.; Beuschel, R. T.; Albanese, A.; McDonough, E.; Hatler, J.; Wiblin, A. E.; Fisher, J.; Croteau, J.; Small, E. C.; Sood, A.; Caprioli, R. M.; Angelo, R. M.; Nolan, G. P.; Chung, K.; Hewitt, S. M.; Germain, R. N.; Spraggins, J. M.; Lundberg, E.; Snyder, M. P.; Kelleher, N. L.; Saka, S. K. Spatial Mapping of Protein Composition and Tissue Organization: A Primer for Multiplexed Antibody-Based Imaging. *Nat. Methods* **2021**. https://doi.org/10.1038/s41592-021-01316-y.

(2) Gerdes, M. J.; Sevinsky, C. J.; Sood, A.; Adak, S.; Bello, M. O.; Bordwell, A.; Can, A.; Corwin, A.; Dinn, S.; Filkins, R. J.; others. Highly Multiplexed Single-Cell Analysis of Formalin-Fixed, Paraffin-Embedded Cancer Tissue. *Proc. Natl. Acad. Sci.* **2013**, *110* (29), 11982–11987.

(3) Lin, J.-R.; Izar, B.; Wang, S.; Yapp, C.; Mei, S.; Shah, P. M.; Santagata, S.; Sorger, P. K. Highly Multiplexed Immunofluorescence Imaging of Human Tissues and Tumors Using T-CyCIF and Conventional Optical Microscopes. *eLife* **2018**, *7*, e31657. https://doi.org/10.7554/eLife.31657.

(4) Radtke, A. J.; Kandov, E.; Lowekamp, B.; Speranza, E.; Chu, C. J.; Gola, A.; Thakur, N.; Shih, R.; Yao, L.; Yaniv, Z. R.; Beuschel, R. T.; Kabat, J.; Croteau, J.; Davis, J.; Hernandez, J. M.; Germain, R. N. IBEX: A Versatile Multiplex Optical Imaging Approach for Deep Phenotyping and Spatial Analysis of Cells in Complex Tissues. *Proc. Natl. Acad. Sci.* **2020**, *117* (52), 33455–33465. https://doi.org/10.1073/pnas.2018488117.

(5) Murray, E.; Cho, J. H.; Goodwin, D.; Ku, T.; Swaney, J.; Kim, S.-Y.; Choi, H.; Park, Y.-G.; Park, J.-Y.; Hubbert, A.; McCue, M.; Vassallo, S.; Bakh, N.; Frosch, M. P.; Wedeen, V. J.; Seung, H. S.; Chung, K. Simple, Scalable Proteomic Imaging for High-Dimensional Profiling of Intact Systems. *Cell* **2015**, *163* (6), 1500–1514. https://doi.org/10.1016/j.cell.2015.11.025.

(6) Goltsev, Y.; Samusik, N.; Kennedy-Darling, J.; Bhate, S.; Hale, M.; Vazquez, G.; Black, S.; Nolan, G. P. Deep Profiling of Mouse Splenic Architecture with CODEX Multiplexed Imaging. *Cell* **2018**, *174* (4), 968-981.e15. https://doi.org/10.1016/j.cell.2018.07.010.

(7) Saka, S. K.; Wang, Y.; Kishi, J. Y.; Zhu, A.; Zeng, Y.; Xie, W.; Kirli, K.; Yapp, C.; Cicconet, M.; Beliveau, B. J.; Lapan, S. W.; Yin, S.; Lin, M.; Boyden, E. S.; Kaeser, P. S.; Pihan, G.; Church, G. M.; Yin, P. Immuno-SABER Enables Highly Multiplexed and Amplified Protein Imaging in Tissues. *Nat. Biotechnol.* **2019**, 1–11. https://doi.org/10.1038/s41587-019-0207-y.

(8) Chen, K. H.; Boettiger, A. N.; Moffitt, J. R.; Wang, S.; Zhuang, X. Spatially Resolved, Highly Multiplexed RNA Profiling in Single Cells. *Science* **2015**, *348* (6233), aaa6090–aaa6090. https://doi.org/10.1126/science.aaa6090.

(9) Shah, S.; Lubeck, E.; Zhou, W.; Cai, L. In Situ Transcription Profiling of Single Cells Reveals Spatial Organization of Cells in the Mouse Hippocampus. *Neuron* **2016**, *92* (2), 342–357. https://doi.org/10.1016/j.neuron.2016.10.001.

(10) Giesen, C.; Wang, H. A. O.; Schapiro, D.; Zivanovic, N.; Jacobs, A.; Hattendorf, B.; Schüffler, P. J.; Grolimund, D.; Buhmann, J. M.; Brandt, S.; Varga, Z.; Wild, P. J.; Günther, D.; Bodenmiller, B. Highly Multiplexed Imaging of Tumor Tissues with Subcellular Resolution by Mass Cytometry. *Nat. Methods* **2014**, *11* (4), 417–422. https://doi.org/10.1038/nmeth.2869.

(11) Angelo, M.; Bendall, S. C.; Finck, R.; Hale, M. B.; Hitzman, C.; Borowsky, A. D.; Levenson, R. M.; Lowe, J. B.; Liu, S. D.; Zhao, S.; Natkunam, Y.; Nolan, G. P. Multiplexed Ion Beam Imaging of Human Breast Tumors. *Nat. Med.* **2014**, *20* (4), 436–442. https://doi.org/10.1038/nm.3488.

(12) Wu, C.; Chiu, D. T. Highly Fluorescent Semiconducting Polymer Dots for Biology and Medicine. *Angew. Chem. Int. Ed.* **2013**, *52* (11), 3086–3109. https://doi.org/10.1002/anie.201205133.

(13) Yu, J.; Rong, Y.; Kuo, C.-T.; Zhou, X.-H.; Chiu, D. T. Recent Advances in the Development of Highly Luminescent Semiconducting Polymer Dots and Nanoparticles for Biological Imaging and Medicine. *Anal. Chem.* **2017**, *89* (1), 42–56. https://doi.org/10.1021/acs.analchem.6b04672.

(14) Wu, C.; Schneider, T.; Zeigler, M.; Yu, J.; Schiro, P. G.; Burnham, D. R.; McNeill, J. D.; Chiu, D. T. Bioconjugation of Ultrabright Semiconducting Polymer Dots for Specific Cellular Targeting. *J. Am. Chem. Soc.* **2010**, *132* (43), 15410–15417. https://doi.org/10.1021/ja107196s.

(15) Ye, F.; Wu, C.; Jin, Y.; Wang, M.; Chan, Y.-H.; Yu, J.; Sun, W.; Hayden, S.; Chiu, D. T. A Compact and Highly Fluorescent Orange-Emitting Polymer Dot for Specific Subcellular Imaging. *Chem. Commun.* **2012**, *48* (12), 1778. https://doi.org/10.1039/c2cc16486h.
(16) Chan, Y.-H.; Ye, F.; Gallina, M. E.; Zhang, X.; Jin, Y.; Wu, I.-C.; Chiu, D. T. Hybrid Semiconducting Polymer Dot–Quantum Dot with Narrow-Band Emission, Near-Infrared Fluorescence, and High Brightness. *J. Am. Chem. Soc.* **2012**, *134* (17), 7309–7312. https://doi.org/10.1021/ja3022973.
(17) Rong, Y.; Wu, C.; Yu, J.; Zhang, X.; Ye, F.; Zeigler, M.; Gallina, M. E.; Wu, I.-C.; Zhang, Y.; Chan, Y.-H.; Sun, W.; Uvdal, K.; Chiu, D. T. Multicolor Fluorescent Semiconducting Polymer Dots with Narrow Emissions and High Brightness. *ACS Nano* **2013**, *7* (1), 376–384. https://doi.org/10.1021/nn304376z.
(18) Zhang, X.; Yu, J.; Rong, Y.; Ye, F.; Chiu, D. T.; Uvdal, K. High-Intensity near-IR Fluorescence in Semiconducting Polymer Dots Achieved by Cascade FRET Strategy. *Chem. Sci.* **2013**, *4* (5), 2143. https://doi.org/10.1039/c3sc50222h.
(19) Ye, F.; Sun, W.; Zhang, Y.; Wu, C.; Zhang, X.; Yu, J.; Rong, Y.; Zhang, M.; Chiu, D. T. Single-Chain Semiconducting Polymer Dots. *Langmuir* **2015**, *31* (1), 499–505. https://doi.org/10.1021/la5038684.
(20) Wu, I.-C.; Yu, J.; Ye, F.; Rong, Y.; Gallina, M. E.; Fujimoto, B. S.; Zhang, Y.; Chan, Y.-H.; Sun, W.; Zhou, X.-H.; Wu, C.; Chiu, D. T. Squaraine-Based Polymer Dots with Narrow, Bright Near-Infrared Fluorescence for Biological Applications. *J. Am. Chem. Soc.* **2015**, *137* (1), 173–178. https://doi.org/10.1021/ja5123045.
(21) Chen, D.; Wu, I.-C.; Liu, Z.; Tang, Y.; Chen, H.; Yu, J.; Wu, C.; Chiu, D. T. Semiconducting Polymer Dots with Bright Narrow-Band Emission at 800 Nm for Biological Applications. *Chem. Sci.* **2017**, *8* (5), 3390–3398. https://doi.org/10.1039/C7SC00441A.
(22) Kuo, C.-T.; Wu, I.-C.; Chen, L.; Yu, J.; Wu, L.; Chiu, D. T. Improving the Photostability of Semiconducting Polymer Dots Using Buffers. *Anal. Chem.* **2018**, *90* (20), 11785–11790. https://doi.org/10.1021/acs.analchem.8b03104.
(23) Zhang, J.; Yu, J.; Jiang, Y.; Chiu, D. T. Ultrabright Pdots with a Large Absorbance Cross Section and High Quantum Yield. *ACS Appl. Mater. Interfaces* **2022**, *14* (11), 13631–13637. https://doi.org/10.1021/acsami.1c25215.
(24) Zimmermann, T.; Marrison, J.; Hogg, K.; O'Toole, P. Clearing Up the Signal: Spectral Imaging and Linear Unmixing in Fluorescence Microscopy. In *Confocal Microscopy*; Paddock, S. W., Ed.; Methods in Molecular Biology; Springer New York: New York, NY, 2014; Vol. 1075, pp 129–148. https://doi.org/10.1007/978-1-60761-847-8_5.
(25) Lin, J.-R.; Chen, Y.-A.; Campton, D.; Cooper, J.; Coy, S.; Yapp, C.; Tefft, J. B.; McCarty, E.; Ligon, K. L.; Rodig, S. J.; Reese, S.; George, T.; Santagata, S.; Sorger, P. K. High-Plex Immunofluorescence Imaging and Traditional Histology of the Same Tissue Section for Discovering Image-Based Biomarkers. *Nat. Cancer* **2023**, *4* (7), 1036–1052. https://doi.org/10.1038/s43018-023-00576-1.
(26) Chen, K.; Yan, R.; Xiang, L.; Xu, K. Excitation Spectral Microscopy for Highly Multiplexed Fluorescence Imaging and Quantitative Biosensing. *Light Sci. Appl.* **2021**, *10* (1), 97. https://doi.org/10.1038/s41377-021-00536-3.
(27) Alterman, M.; Schechner, Y. Y.; Weiss, A. Multiplexed Fluorescence Unmixing. In *2010 IEEE International Conference on Computational Photography (ICCP)*; IEEE: Cambridge, MA, USA, 2010; pp 1–8. https://doi.org/10.1109/ICCPHOT.2010.5585093.
(28) Fereidouni, F.; Bader, A. N.; Gerritsen, H. C. Spectral Phasor Analysis Allows Rapid and Reliable Unmixing of Fluorescence Microscopy Spectral Images. *Opt. Express* **2012**, *20* (12), 12729. https://doi.org/10.1364/OE.20.012729.
(29) Cutrale, F.; Trivedi, V.; Trinh, L. A.; Chiu, C.-L.; Choi, J. M.; Artiga, M. S.; Fraser, S. E. Hyperspectral Phasor Analysis Enables Multiplexed 5D in Vivo Imaging. *Nat. Methods* **2017**, *14* (2), 149–152. https://doi.org/10.1038/nmeth.4134.
(30) Neher, R. A.; Mitkovski, M.; Kirchhoff, F.; Neher, E.; Theis, F. J.; Zeug, A. Blind Source

Separation Techniques for the Decomposition of Multiply Labeled Fluorescence Images. *Biophys. J.* **2009**, *96* (9), 3791–3800. https://doi.org/10.1016/j.bpj.2008.10.068.
(31) Seo, J.; Sim, Y.; Kim, J.; Kim, H.; Cho, I.; Nam, H.; Yoon, Y.-G.; Chang, J.-B. PICASSO Allows Ultra-Multiplexed Fluorescence Imaging of Spatially Overlapping Proteins without Reference Spectra Measurements. *Nat. Commun.* **2022**, *13* (1), 2475. https://doi.org/10.1038/s41467-022-30168-z.

Chapter 3

Highly Multiplexed Volumetric Imaging for Thick Tissues

3.1. Abstract

The field of biology has been revolutionized by new imaging technologies that can specifically visualize and phenotype cells within tissues. Highly multiplexed fluorescence microscopy has emerged as a powerful technique for simultaneously visualizing and quantifying multiple molecular targets within tissues, while light sheet microscopy combined with tissue clearing methods enables detailed volumetric imaging of thick intact samples. However, as biology occurs in 3D in real life, integrating these two technologies to achieve highly multiplexed volumetric imaging has remained challenging. Traditional multiplexed fluorescence microscopy can image up to five targets simultaneously. Yet, newer methods have broadened this capability to tens of channels or more through cyclic staining and imaging, with signal elimination between rounds. These multi-round staining techniques currently work only with thin tissue sections, and the whole process takes hours to days. For thicker tissue, from 100 μm to the thickness of whole organs or organisms, the diffusion time for labeling probes scales as the square of the thickness to be penetrated, which could extend to weeks or months[1].

To address this challenge, we propose to combine semiconducting polymer dot (Pdot) probes and an open-top light sheet microscopy system optimized for spectral imaging. Pdots offer special photophysical properties, such as high brightness and various ranges of spectral tunability, enabling 20-30 channel multiplexed imaging in a single round of staining and imaging. Despite these advantages, Pdot probes are facing challenges in achieving uniform penetration into thick tissues deeply. To benchmark the performance of previously reported technologies on probe delivery, we evaluated standard/unoptimized and enhanced passive labeling protocols, including SWITCH[2] and CUBIC[3,4], which use a mild detergent and specialized additive buffers, respectively, to control antibody-antigen binding and to improve antibody diffusion while preserving tissue structure (introduced in **Chapter 1.3**). Our results indicated that current labeling methods provided only minimal improvements in Pdot-antibody penetration. These findings underscore ongoing challenges and highlight the need for further optimization, including synthesizing smaller single-chain Pdots and employing electrophoresis-enhanced labeling methods. This study establishes a foundation for developing scalable, highly multiplexed volumetric imaging approaches for complex tissue analysis.

3.2. Introduction

Volumetric imaging of intact tissues provides crucial insights into biomolecular spatial organization, disease progression, and multicellular dynamics at an organ-scale resolution. However, the challenge of delivering fluorescent probes deep into dense biological specimens has remained a limiting factor, particularly for high-plex immunolabeling. While traditional immunofluorescence excels in thin sections, its application to thick tissues (>500 μm) faces major barriers due to slow probe diffusion, uneven labeling, probe depletion, and limited penetration through dense tissue structures. Several methods have been developed to enhance antibody penetration in thick tissues[5–11], but the most common and easily applicable approach is simply passive diffusion of antibody-fluorophore conjugates[2,4,12,13]. This method often takes several days to weeks depending on tissue thickness, complexity, and antigen location. Additionally, the effectiveness of immunolabeling significantly decreases in dense or large specimens, resulting in more concentrated probe labeling on specimen surfaces compared to the interior[4,14,15]. This often contributes to additional imaging challenges due to higher light absorption at sample surface, resulting in diminished fluorescence from the interior of the sample. To address these challenges, several advanced passive diffusion and active labeling strategies have been developed to improve immunolabeling.

Passive diffusion methods SWITCH[2], SHANEL[12], and CUBIC-HistoVision2 (commercially available, cubicstars.com) employ a low concentration of detergent, such as SDS (sodium dodecyl sulfate) or CHAPS (3-[(3-cholamidopropyl)dimethylammonio]-1-propanesulfonate), to temporarily inhibit antibody binding during the diffusion phase. This is followed by detergent removal, enabling uniform antibody staining across the depth of specimens. SPEARs[13], another passive diffusion method, utilizes pH buffers and chemically engineered antibodies that enhance stability at higher temperatures (~37–55 °C). Higher temperatures increase the antibody diffusion rate, enabling deeper labeling penetration. These enhanced passive diffusion methods are advantageous as they retain tissue architecture and do not require specialized equipment.

On the other hand, active labeling methods introduce force-driven techniques to rapidly and uniformly label thick tissue specimens. Electrophoretic methods such as CLARITY[5,6], eFLASH[7], EERS[8], and CuRVE[9] take advantage of antibody charge ratios to pull them through the thickness of the tissue. This achieves uniform and rapid labeling, typically less than a few hours for a ~1 mm thick tissue slice, but requires specialized equipment. ELAST[16] utilizes machinery that protracts and retracts the specimen, allowing for accelerated antibody delivery; however, this increases the risk of tissue deformation. c-PRESTO[11] applies low centrifugal force (600g) to significantly reduce immunolabeling time but not penetration. BOOST[10] utilizes microwave irradiation to accelerate antibody penetration 10-80 times faster than passive diffusion. These

active approaches usually require specialized equipment and utilize procedures that risk introducing tissue damage.

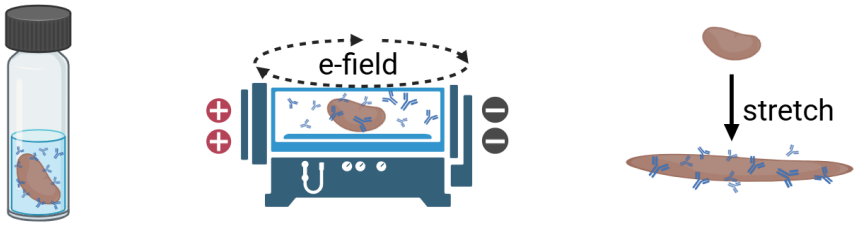

Figure 3.1. Thick tissue labeling strategies. *The basic concepts of several published thick tissue labeling techniques are illustrated: passive labeling, e-field-assisted labeling, and stretching-assisted "2D" labeling.*

Among all the thick tissue labeling methods, no existing imaging platform has demonstrated the ability to perform more than 12-channel immunolabeling and volumetric imaging of thick tissue specimens (greater than 500 µm) in a single round. Highly multiplexed imaging is largely restricted to 2D sections, where methods like CODEX[17], t-CyCIF[18], and IBEX[19] achieve 30–60+ channels using iterative staining cycles. These techniques are limited to thin sections, typically less than 50 µm or FFPE sections (3-10 µm thick), due to the long probe delivery times and potential distortion introduced by repeated rounds of staining and washing. Similarly, while commercial mass spectrometry-based imaging methods (e.g., MIBI[20], IMC[21]) offer high multiplexing capabilities, they are destructive and limited to 2D surfaces.

To bridge this gap, we seek to combine spectrally tunable polymer dot (Pdot) probes[22], CUBIC tissue clearing[23], and open-top light sheet fluorescence microscopy (OTLS)[24] to advance highly multiplexed volumetric imaging of thick tissues. Pdots offer the capability for single-round detection of over 20 targets due to their exceptional brightness, photostability, and broadly tunable Stokes shifts. Efforts to utilize them for highly multiplexed imaging of thick tissue (>500 µm) are ongoing.

In this chapter, we describe work aimed at optimizing the labeling uniformity and penetration depth of each Pdot-antibody conjugate in thick mouse kidney sections using both SWITCH and CUBIC-HistoVision2 staining protocols. Through ongoing improvements in thick tissue labeling, our goal is to establish a fast, highly multiplexed volumetric immunofluorescence light-sheet microscopy approach using polymer dots, enabling single-round, organ-scale spatial biology with 20+ channels.

3.3. Results

3.3.1. Thick Pdot Tissue Labeling Using Standard Passive Diffusion

Initial attempts to label ~1 mm-thick mouse kidney sections using standard unoptimized passive incubation of Pdot-antibody conjugates for 1-2 weeks resulted in uneven staining (**Figure 3.2**). Signals were strong at tissue surfaces but dropped rapidly with depth. Among all 22 Pdot-antibody conjugates, with 2 weeks incubation, eight show decent signal across the 1 mm kidney section, seven show uneven superficial labeling (~50-100 µm) that needs further optimization on the staining protocol, and seven did not work due to Pdot conjugation failure or the probe not being compatible with the clearing method (**Figure 3.3**). Interestingly, Pdot-antibody conjugates targeting structures in the interstitial space, such as vasculature, immune cells, nerves, and lymphatic vessels, tend to penetrate deeper than those targeting structures inside the tubules, like the apical surface of tubular cells. In addition, staining is generally better in the medullary region than in the cortex, likely because the medulla contains straight tubular bundles, while the cortex has a more compact and convoluted structure.

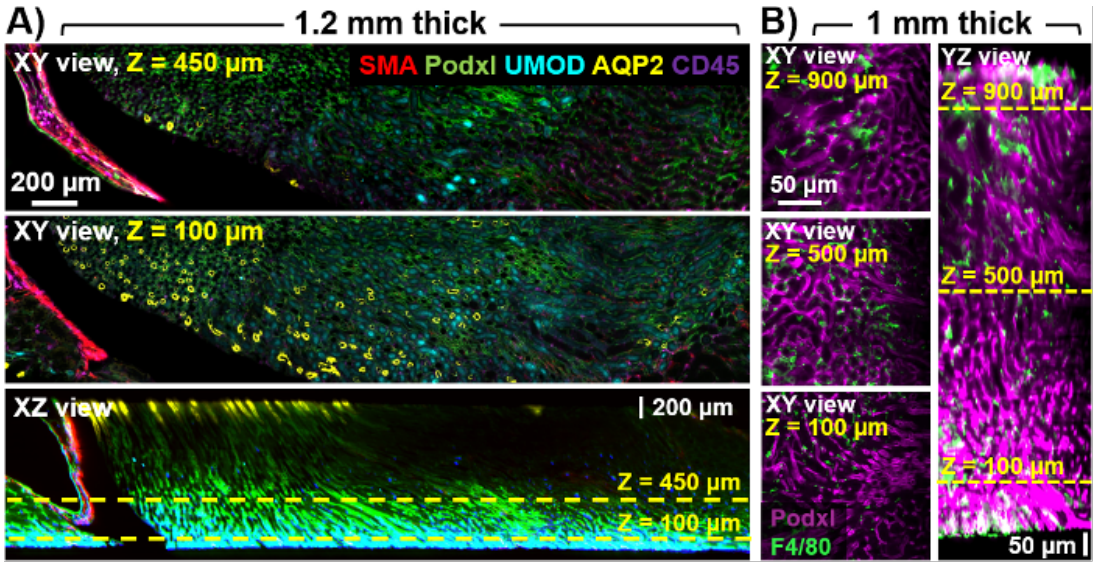

Figure 3.2. Multiplexed light sheet imaging of thick mouse tissues stained with Pdots. *A) 5-plex and B) 3-plex stained kidney slice in xy and xz orientation.*

405-440	405-480	405-515	405-570	405-605	405-670	405-710		405-790
Rat IgG2b **CD45** (immune cell) **Labels 1mm MK** (High Intensity)	Gt **CD31** (vasculature) **Inconsistent Labeling**	Gt **Podocalyxin** (podocyte, vasculature) **Labels 1mm MK** (High Intensity)	Rb **AQP1** (PCT, tDL) **Medulla=1mm Cortex=Surface**	Rb **CollagenIV**	Ms IgG2a **TH** (sympathetic nerve) **Labels 1mm MK** (Low Intensity)	Rb **PV** (DCT) **Surface Labeling**		Ms IgG2a **α-SMA** (big arteries) **Labels 1mm MK** (Low Intensity)
		488-520	**488-580**	**488-610**	**488-675**		**488-765**	**488-810**
		Rb **Calbindin** (DCT) **Surface labeling**	Rb **AQP2** (collecting duct) **Penetration Issue (~350 µm)**	Rb **NKCC2** (TAL/MD) **Surface labeling (<50 µm)**	Ms IgG2a **Tuj1** (sensory nerve) **Labels 1mm MK** (Low Intensity)		Rb **SGLT2** (PT S1/2) **Penetration Issue (~75 µm)**	Open Channel
			561-580	**SBY605**	**561-670**	**561-720**		**561-790**
			Rb **NCC** (DCT) **Surface labeling (<50 µm)**	Ms IgG2b **F4/80** (macrophages) **Labels 1mm MK** (Low Intensity)	Rat IgG2a **UMOD** (TAL/DCT) **Labels 1mm MK** (Moderate→Low Intensity)	Ms IgG1 **PDGFR-ß** (vasculature) **Pdot Conjugation Failure**		Rat IgG2a **CD13** (PT S1/2/3) **Incompatabile w/ CUBIC-L**
					SBR670	SBR715	SBR775	SBR815
					CD161 (NK & in rare T/Monocyte subsets) **Fibrosis Panel**	**CD19** (B-cell) **Fibrosis Panel**	CD3 (T-cell) **Fibrosis Panel**	CD11b (Granulocytes, monocyte, macrophage) **Fibrosis Panel**

Figure 3.3. Current Pdot-antibody conjugates panel. *All conjugates are grouped by their excitation wavelength in rows and excitation wavelength in columns. Green highlighting indicates good labeling throughout 1 mm-thick kidney slices, yellow indicates inadequate penetration, and red indicates unusable conjugates.*

3.3.2. Exploration of other thick tissue labeling methods for Pdot-antibody conjugates

For optimizing passive diffusion, there are several factors that could improve antibody diffusion, such as high detergent concentration for tissue delipidation, optimized salt concentration, antibody concentration, temperature, and pH. We explored several detergent variations, including SWITCH[2], which was developed for whole mouse brain hemispheres (~5 mm thick) and enabled uniform antibody labeling in approximately 9 days. The SWITCH protocol uses an initial 6-day incubation with antibody in 10 mM SDS that is designed to enable transport while hindering binding, followed by 2–3 days of reactivation in detergent-free binding buffer that is designed to enable binding. This two-step approach is intended to allow antibodies to diffuse more uniformly throughout the tissue without binding to their targets on the surface at the early incubation stage. For Pdot-antibody conjugates, I adapted a shortened protocol by incubating ~500 µm mouse kidney sections in labeling buffer containing 1–10 mM SDS to suppress binding for 2 days, followed by one day of reactivation in a large volume of PBST to enable binding. Unfortunately, I did not see a promising deeper penetration or more uniform labeling across the tissue depth in my tests. The staining patterns of multiple targets, including CD45 and aquaporin-1, remained superficial and uneven, similar to unoptimized passive diffusion.

I also evaluated the CUBIC-HistoVision2 (HV2) antibody incubation kit, an updated version of the original CUBIC-HV[4,23] kit developed for deep immunolabeling of whole organs, especially in brain tissue. This

method is built based on two core technologies: HV-LLPS (liquid-liquid phase separation), which utilizes a “wrapping reagent” to condense staining probes by minimizing buffer volume, and HV-additives, which is a library of optimized compounds that enhance probe diffusion by modulating probe-tissue interactions. However, adapting HV2 for the Pdot-antibody conjugates in ~500 μm mouse kidney tissue was less successful. Each antibody required specific optimization, and the staining outcomes were often comparable to, or occasionally worse than, those obtained with unoptimized incubation conditions. Both penetration depth and labeling uniformity remained similar to passive diffusion, showing no significant overall improvement. Given the complexity of additive screening for each of 20+ Pdot-antibody conjugates, which conflicts with the goal of a simplified, single-round staining workflow, this approach was not further pursued.

3.4. Discussion

Achieving efficient and uniform immunolabeling in thick tissues has remained a persistent challenge in the field of volumetric imaging, particularly in bridging the gap between higher-plex and volumetric imaging. Despite significant advancements in both tissue clearing and light sheet microscopy, the bottleneck of probe delivery continues to limit the full potential of 3D spatial biology. In this study, I evaluated existing passive and two enhanced diffusion methods from the literature to assess their compatibility with Pdot-antibody conjugates for thick tissue labeling.

Initial exploration using standard/unoptimized passive diffusion reaffirmed the inherent limitations of this approach. Even after extended incubation periods of up to two weeks, only 8 out of 22 Pdot-antibody conjugates that target intertubular achieved satisfactory labeling across ~1 mm-thick mouse kidney sections. The majority of intratubular probes either exhibited superficial staining or lost specificity due to issues related to Pdot conjugation or incompatibility with the clearing process.

While those preliminary tests on SWITCH and CUBIC-HV2 offered helpful insight into their limitations, neither method provided promising results for thick tissue labeling with Pdot-antibody conjugates. This could be due to several factors. The protocol may require further optimization for kidney tissue, since the kidney is more densely packed compared to the brain, which was used in the original publication[2,4,23]. A harsh tissue pretreatment to loosen the dense structure might be useful for testing. Second, the relatively large size of Pdot-antibody conjugates (~14 nm Pdot plus ~14 nm antibody, assuming Pdot to antibody conjugation ratio is 1:1) and possible charge-related properties may limit their diffusion ability, since the published methods were developed for conventional primary antibodies and smaller Fab secondary-dye

conjugates. Similarly, the CUBIC-HistoVision2 approach, despite offering multiple additive combinations, proved impractical for high-plex workflows.

These collective observations highlight a critical gap in thick tissue labeling methodologies, particularly for novel probe systems such as Pdots. Future efforts should focus on addressing the fundamental barriers to diffusion and gaining a deeper understanding of the antibody-antigen binding mechanism. One promising direction is the development of smaller, single-chain Pdot constructs, which could reduce steric hindrance and improve tissue penetration without compromising brightness or spectral tunability. Additionally, integrating active labeling strategies, such as electrophoretic delivery, tailored specifically for nanoparticle-based probes, could provide the necessary driving force to achieve rapid and uniform labeling across large tissue volumes. Further optimization of incubation parameters, including buffer composition, pH, temperature, pressure, and detergents, as well as microwave-assisted incubation, may also enhance diffusion kinetics while preserving probe and tissue integrity. Exploring hybrid approaches that combine mild active forces with optimized chemical environments could strike a balance between efficiency and tissue preservation.

If successful, these advancements would enable a transformative shift in spatial biology, allowing for true single-round, highly multiplexed volumetric imaging of intact organs. This capability would drastically reduce staining times from weeks to days or even hours, while providing comprehensive molecular maps at cellular resolution across entire tissues. Such progress would not only accelerate basic research in developmental biology, neuroscience, and immunology but also open new avenues in clinical pathology, where rapid, high-content 3D diagnostics could revolutionize disease characterization and personalized medicine.

In conclusion, while current thick tissue labeling techniques remain inadequate for Pdot-based multiplexed imaging, this study lays a critical foundation for future innovations in this field. Continued efforts in probe design, labeling methodology, and integration with advanced microscopy platforms are essential to overcoming these challenges and realizing the full potential of organ-scale, high-dimensional spatial analysis.

3.5. Materials and Methods

3.5.1. Tissue preparation

After CO_2 euthanasia immediately, mice were cardiac-perfused with PBS-azide and 4% paraformaldehyde (PFA), each for 5 min. The kidneys, with renal capsule removed, were harvested and fixed in 10 mL of 4%

PFA for 1 h. The brain was fixed overnight in PFA. After fixation, the kidneys were sliced into 500 µm and 1 mm sections along the horizontal/transverse plane using a vibratome. All sections were stored in PBS-azide at 4 ºC until further use.

3.5.2. Pdot-antibody conjugates

Pdots were conjugated to antibodies or lectin via a 1-ethyl-3-(-3-dimethylaminopropyl) carbodiimide hydrochloride (EDC) catalyzed reaction, in which 0.25 mL of Pdot solution was mixed with 3 uL of EDC and 60 uL of an antibody solution, and reacted for 3 h. The final solution was then loaded onto a gel filtration column to purify the Pdot-antibodies from free unreacted antibodies.

3.5.3. Tissue clearing, immunolabeling, and RI matching

Mouse kidney slices are incubated at 37°C overnight in 1:1 DI H_2O/CUBIC-L, followed by incubation for 2 days at 37 °C in 100% CUBIC-L. Tissues are incubated in block/permeabilization solution (3% bovine serum albumin and 0.5% Triton-X 100) overnight at 4 °C. Then incubated in block/perm along with Pdot or primary/secondary antibodies for 1 day to 2 weeks at 4 °C, depending on experiment type and tissue thickness. Tissues are then washed 3 times in PBS for 1 hour. Immunolabeled tissues are incubated at RT in 1:1 DI H_2O/CUBIC-R overnight, followed by a 2-day incubation in 100% CUBIC-R. CUBIC clearing reagents are made according to the published protocol by Matsumoto et al[23].

3.5.4. SWITCH staining

Tissues were incubated in SWITCH-OFF solution (10 mM SDS in PBS) overnight at 37 °C. Then transfer samples to fresh SWITCH-OFF solution and Pdot-antibody probes, just to cover the sample, for 2 days at 37 °C. Transfer samples to a large volume of SWITCH-ON solution (PBST, 0.2% Triton X-100 in PBS) to remove SDS, and samples were incubated overnight for antibody binding.

3.5.5. CUBIC-HistoVision2 Staining Protocol

Tissues were stained following manufacturer protocols. After primary and secondary Pdot labeling steps, tissues were washed and re-cleared before imaging. Cleared mouse kidney sections (300–500 µm thick) were incubated in CUBIC-HistoVision2 antibody incubation buffer containing 2–5 Pdot-antibody conjugates for 2–4 days at 37 °C, followed by a brief amplification step per manufacturer instructions. Samples were extensively washed in CUBIC-PBS solution, re-cleared with CUBIC-2 solution, and imaged using OTLS. No enzymatic digestion or mechanical agitation was applied. Labeling depth and uniformity were assessed via xz-slice projection and intensity profiling in ImageJ.

3.5.6. Imaging with custom open-top lightsheet microscopes

Three-dimensional (3D) volumetric imaging of CUBIC cleared mouse kidney slices, 0.5-1 mm^3, was performed using the non-orthogonal dual objective (NODO) system introduced in the published hybrid OTLS by Glaser et al[24]. Excitation light source was delivered by a single-mode fiber from a four-channel (405, 488, 561, and 638 nm) laser package (Versalase, Vortran Lasers) and scanned using two-axis galvanometers (6220H, Cambridge Technology) to create a digital light sheet with $0.10 \times n$ illumination NA, where n is the refractive index. Fluorescence emission was collected via an assembly of motorized filter wheels (FW102C, Thorlabs), a FOV-maximized optical path, and focused onto a 2048 × 2048 pixel sCMOS camera (ORCA-Flash4.0 V3, Hamamatsu) mounted on a translational stage to compensate for focus misalignment caused by different wavelengths.

The spatial resolution is ~1 μm lateral and 2.7 μm axial for a refractive index of 1.56. The exposure time per frame was set to 20 ms. The specimen was laterally scanned in the y-direction across a stationary lightsheet to generate an image strip (2048 × 256). The same tile was rescanned with different laser/filter combinations before moving to the next tile position. A 5% overlap between tiles was used. When tiling vertically, the laser power was increased with depth to account for laser attenuation as it penetrates deeper into the specimen. 3D imaging was achieved using a combination of stage scanning and lateral/vertical tiling with a motorized XY stage and Z actuators (S562-2235A and LS-50-FTP, Applied Scientific Instrumentation). The entire image acquisition was controlled using a custom-written Python program that is available from the authors upon request.

3.5.7. Image post-processing - compression, stitching, and fusion

Raw camera frames were streamed from camera to RAM where on-the-fly downsampling (×2) was performed. These processing steps slow down the net data rate from camera to disk but save significant storage space. The output XML file is suitable for immediate post-processing with the BigStitcher plugin on ImageJ. All imaging tiles were aligned, stitched, and fused into one contiguous 3D image.

3.7. References

(1) Zhao, S.; Todorov, M. I.; Cai, R.; -Maskari, R. A.; Steinke, H.; Kemter, E.; Mai, H.; Rong, Z.; Warmer, M.; Stanic, K.; Schoppe, O.; Paetzold, J. C.; Gesierich, B.; Wong, M. N.; Huber, T. B.; Duering, M.; Bruns, O. T.; Menze, B.; Lipfert, J.; Puelles, V. G.; Wolf, E.; Bechmann, I.; Ertürk, A. Cellular and Molecular Probing of Intact Human Organs. *Cell* **2020**, *180* (4), 796-812.e19. https://doi.org/10.1016/j.cell.2020.01.030.

(2) Murray, E.; Cho, J. H.; Goodwin, D.; Ku, T.; Swaney, J.; Kim, S.-Y.; Choi, H.; Park, Y.-G.; Park, J.-Y.; Hubbert, A.; McCue, M.; Vassallo, S.; Bakh, N.; Frosch, M. P.; Wedeen, V. J.; Seung, H. S.; Chung, K. Simple, Scalable Proteomic Imaging for High-Dimensional Profiling of Intact Systems. *Cell* **2015**, *163* (6), 1500–1514. https://doi.org/10.1016/j.cell.2015.11.025.

(3) Tainaka, K.; Kuno, A.; Kubota, S. I.; Murakami, T.; Ueda, H. R. Chemical Principles in Tissue Clearing and Staining Protocols for Whole-Body Cell Profiling. *Annu. Rev. Cell Dev. Biol.* **2016**, *32* (1), 713–741. https://doi.org/10.1146/annurev-cellbio-111315-125001.

(4) Susaki, E. A.; Shimizu, C.; Kuno, A.; Tainaka, K.; Li, X.; Nishi, K.; Morishima, K.; Ono, H.; Ode, K. L.; Saeki, Y.; Miyamichi, K.; Isa, K.; Yokoyama, C.; Kitaura, H.; Ikemura, M.; Ushiku, T.; Shimizu, Y.; Saito, T.; Saido, T. C.; Fukayama, M.; Onoe, H.; Touhara, K.; Isa, T.; Kakita, A.; Shibayama, M.; Ueda, H. R. Versatile Whole-Organ/Body Staining and Imaging Based on Electrolyte-Gel Properties of Biological Tissues. *Nat. Commun.* **2020**, *11* (1), 1982. https://doi.org/10.1038/s41467-020-15906-5.

(5) Tomer, R.; Ye, L.; Hsueh, B.; Deisseroth, K. Advanced CLARITY for Rapid and High-Resolution Imaging of Intact Tissues. *Nat. Protoc.* **2014**, *9* (7), 1682–1697. https://doi.org/10.1038/nprot.2014.123.

(6) Chung, K.; Deisseroth, K. CLARITY for Mapping the Nervous System. *Nat. Methods* **2013**, *10* (6), 508–513. https://doi.org/10.1038/nmeth.2481.

(7) Yun, D. H.; Park, Y.-G.; Cho, J. H.; Kamentsky, L.; Evans, N. B.; Albanese, A.; Xie, K.; Swaney, J.; Sohn, C. H.; Tian, Y.; Zhang, Q.; Drummond, G.; Guan, W.; DiNapoli, N.; Choi, H.; Jung, H.-Y.; Ruelas, L.; Feng, G.; Chung, K. Ultrafast Immunostaining of Organ-Scale Tissues for Scalable Proteomic Phenotyping. *bioRxiv pre-print* **2019**.

(8) Zhang, N.; Li, X.; Czajkowsky, D. M.; Zhang, H.; Alam, M. S.; Shao, Z. Efficient and Fast Immuno-Labeling of Clarified Tissues Using Low-Field Enhanced Diffusion. *IEEE Trans. Biomed. Eng.* **2021**, *68* (11), 3301–3307. https://doi.org/10.1109/TBME.2021.3070146.

(9) Yun, D. H.; Park, Y.-G.; Cho, J. H.; Kamentsky, L.; Evans, N. B.; DiNapoli, N.; Xie, K.; Choi, S. W.; Albanese, A.; Tian, Y.; Sohn, C. H.; Zhang, Q.; Kim, M. E.; Swaney, J.; Guan, W.; Park, J.; Drummond, G.; Choi, H.; Ruelas, L.; Feng, G.; Chung, K. Uniform Volumetric Single-Cell Processing for Organ-Scale Molecular Phenotyping. *Nat. Biotechnol.* **2025**, 1–12. https://doi.org/10.1038/s41587-024-02533-4.

(10) Guo, J.; Yang, H.; Lu, C.; Cui, D.; Zhao, M.; Li, C.; Chen, W.; Yang, Q.; Li, Z.; Chen, M.; Zhao, S.; Zhou, J.; He, J.; Jiang, H. BOOST: A Robust Ten-Fold Expansion Method on Hour-Scale. *Nat. Commun.* **2025**, *16* (1), 2107. https://doi.org/10.1038/s41467-025-57350-3.

(11) Lee, E.; Sun, W.; Lee, E.; Sun, W. ACT-PRESTO: Biological Tissue Clearing and Immunolabeling Methods for Volume Imaging. *J. Vis. Exp. JoVE* **2016**, No. 118, e54904. https://doi.org/10.3791/54904.

(12) Mai, H.; Rong, Z.; Zhao, S.; Cai, R.; Steinke, H.; Bechmann, I.; Ertürk, A. Scalable Tissue Labeling and Clearing of Intact Human Organs. *Nat. Protoc.* **2022**, *17* (10), 2188–2215. https://doi.org/10.1038/s41596-022-00712-8.

(13) Lai, H. M.; Tang, Y.; Lau, Z. Y. H.; Campbell, R. A. A.; Yau, J. C. N.; Chan, C. C. Y.; Chan, D. C. W.; Wong, T. Y.; Wong, H. K. T.; Yan, L. Y. C.; Wu, W. K. K.; Wong, S. H.; Kwok, K.-W.; Wing, Y.-K.; Lam, H. H. N.; Ng, H.-K.; Mrsic-Flogel, T. D.; Mok, V. C. T.; Chan, J. Y. K.; Ko, H. Antibody Stabilization for Thermally Accelerated Deep Immunostaining. *Nat. Methods* **2022**, *19* (9), 1137–1146.

https://doi.org/10.1038/s41592-022-01569-1.
(14) Chung, K.; Wallace, J.; Kim, S.-Y.; Kalyanasundaram, S.; Andalman, A. S.; Davidson, T. J.; Mirzabekov, J. J.; Zalocusky, K. A.; Mattis, J.; Denisin, A. K.; Pak, S.; Bernstein, H.; Ramakrishnan, C.; Grosenick, L.; Gradinaru, V.; Deisseroth, K. Structural and Molecular Interrogation of Intact Biological Systems. *Nature* **2013**, *497* (7449), 332–337. https://doi.org/10.1038/nature12107.
(15) Yang, B.; Treweek, J. B.; Kulkarni, R. P.; Deverman, B. E.; Chen, C.-K.; Lubeck, E.; Shah, S.; Cai, L.; Gradinaru, V. Single-Cell Phenotyping within Transparent Intact Tissue through Whole-Body Clearing. *Cell* **2014**, *158* (4), 945–958. https://doi.org/10.1016/j.cell.2014.07.017.
(16) Ku, T.; Guan, W.; Evans, N. B.; Sohn, C. H.; Albanese, A.; Kim, J.-G.; Frosch, M. P.; Chung, K. Elasticizing Tissues for Reversible Shape Transformation and Accelerated Molecular Labeling. *Nat. Methods* **2020**, *17* (6), 609–613. https://doi.org/10.1038/s41592-020-0823-y.
(17) Goltsev, Y.; Samusik, N.; Kennedy-Darling, J.; Bhate, S.; Hale, M.; Vazquez, G.; Black, S.; Nolan, G. P. Deep Profiling of Mouse Splenic Architecture with CODEX Multiplexed Imaging. *Cell* **2018**, *174* (4), 968-981.e15. https://doi.org/10.1016/j.cell.2018.07.010.
(18) Lin, J.-R.; Izar, B.; Wang, S.; Yapp, C.; Mei, S.; Shah, P. M.; Santagata, S.; Sorger, P. K. Highly Multiplexed Immunofluorescence Imaging of Human Tissues and Tumors Using T-CyCIF and Conventional Optical Microscopes. *eLife* **2018**, *7*, e31657. https://doi.org/10.7554/eLife.31657.
(19) Radtke, A. J.; Kandov, E.; Lowekamp, B.; Speranza, E.; Chu, C. J.; Gola, A.; Thakur, N.; Shih, R.; Yao, L.; Yaniv, Z. R.; Beuschel, R. T.; Kabat, J.; Croteau, J.; Davis, J.; Hernandez, J. M.; Germain, R. N. IBEX: A Versatile Multiplex Optical Imaging Approach for Deep Phenotyping and Spatial Analysis of Cells in Complex Tissues. *Proc. Natl. Acad. Sci.* **2020**, *117* (52), 33455–33465. https://doi.org/10.1073/pnas.2018488117.
(20) Angelo, M.; Bendall, S. C.; Finck, R.; Hale, M. B.; Hitzman, C.; Borowsky, A. D.; Levenson, R. M.; Lowe, J. B.; Liu, S. D.; Zhao, S.; Natkunam, Y.; Nolan, G. P. Multiplexed Ion Beam Imaging of Human Breast Tumors. *Nat. Med.* **2014**, *20* (4), 436–442. https://doi.org/10.1038/nm.3488.
(21) Giesen, C.; Wang, H. A. O.; Schapiro, D.; Zivanovic, N.; Jacobs, A.; Hattendorf, B.; Schüffler, P. J.; Grolimund, D.; Buhmann, J. M.; Brandt, S.; Varga, Z.; Wild, P. J.; Günther, D.; Bodenmiller, B. Highly Multiplexed Imaging of Tumor Tissues with Subcellular Resolution by Mass Cytometry. *Nat. Methods* **2014**, *11* (4), 417–422. https://doi.org/10.1038/nmeth.2869.
(22) Guo, Z.; Poudel, C.; Sarfatis, M. C.; Yu, J.; Wong, M.; Chiu, D. T.; Vaughan, J. C. Highly Multiplexed Fluorescence Microscopy with Spectrally Tunable Semiconducting Polymer Dots. *ScienceAdvances* **2024**.
(23) Matsumoto, K.; Mitani, T. T.; Horiguchi, S. A.; Kaneshiro, J.; Murakami, T. C.; Mano, T.; Fujishima, H.; Konno, A.; Watanabe, T. M.; Hirai, H.; Ueda, H. R. Advanced CUBIC Tissue Clearing for Whole-Organ Cell Profiling. *Nat. Protoc.* **2019**, *14* (12), 3506–3537. https://doi.org/10.1038/s41596-019-0240-9.
(24) Glaser, A. K.; Bishop, K. W.; Barner, L. A.; Susaki, E. A.; Kubota, S. I.; Gao, G.; Serafin, R. B.; Balaram, P.; Turschak, E.; Nicovich, P. R.; Lai, H.; Lucas, L. A. G.; Yi, Y.; Nichols, E. K.; Huang, H.; Reder, N. P.; Wilson, J. J.; Sivakumar, R.; Shamskhou, E.; Stoltzfus, C. R.; Wei, X.; Hempton, A. K.; Pende, M.; Murawala, P.; Dodt, H.-U.; Imaizumi, T.; Shendure, J.; Beliveau, B. J.; Gerner, M. Y.; Xin, L.; Zhao, H.; True, L. D.; Reid, R. C.; Chandrashekar, J.; Ueda, H. R.; Svoboda, K.; Liu, J. T. C. A Hybrid Open-Top Light-Sheet Microscope for Versatile Multi-Scale Imaging of Cleared Tissues. *Nat. Methods* **2022**, *19* (5), 613–619. https://doi.org/10.1038/s41592-022-01468-5.